A comprehensive numerical and experimental study of Fibre Reinforced Polymer Composites fatigue response

Fatigue Life Prediction through stress dependent stiffness degradation: FEA with integrated VUSDFLD user subroutine study of FRP with and without imperfections

MSc Thesis

E.S. Gommers

Delft University of Technology

TU Delft

A comprehensive numerical and experimental study of Fibre Reinforced Polymer Composites fatigue response

Fatigue Life Prediction through stress dependent stiffness degradation: FEA with integrated VUSDFLD user subroutine study of FRP with and without imperfections

by

E.S. Gommers

Thesis committee:	Dr. M. Pavlovic	Chair supervisor
	Dr. O. Karpenko	Daily supervisor
	Dr.ir. F. van der Meer	Supervisor
Project Duration:	October, 2023 - November, 2024	
Faculty:	Faculty of Civil Engineering and Geosciences, Delft	
Degree:	MSc. Civil Engineering	
Track:	Structural Engineering	
Student number:	5421233	

Cover: Static tested coupon with DIC system after failure by O. Karpenko

TU Delft

Preface

Dear reader,

Hereby I would like to present my final work of my Master of Structural Engineering at the Faculty of Civil Engineering and Geoscience at the Technical University of Delft. This Master's thesis represents the work I have done on my thesis project over the past year, which includes some of the most stressful but also valuable periods of my academic career, even up to the last day. Upon writing this last part of my thesis, I can say that I experience mixed feelings between having to say an end to the student life, but also feeling somewhat relieved that the thesis journey is over. But all this work could not have been completed without the help of many that supported me along the way.

I would like to begin by thanking my thesis committee, who continuously guided me, helping me stay on the right track. First of, I would like to express my gratitude towards my chair supervisor Marko Pavlovic, who kept challenging me to pursue the right questions throughout my thesis. I would like to thank Olena Karpenko, my daily supervisor, for keeping her patience with me even though I reached out to her daily. Your support and feedback through all the obstacles that I had to overcome means a lot to me. And lastly, I would like to thank Frans van der Meer for taking the time to assist me and provide feedback on all the questions and work I was struggling with.

Besides sitting behind a desk doing research, a large part of my thesis was also spent inside the south hall of Stevin lab II doing experimental research. I would like to thank the lab staff, particularly Fred Schilperoort, for assisting me with the test set-up and operating the machines. Extra thanks go to Abishek Baskar, who tirelessly helped me create the resin-end coupons for my fatigue tests.

Lastly, I would like to thank my friends and family for their unconditional support and care. You all provided me with company and distractions when the thesis life seemed to overwhelm me. I would like to give a special thanks to my amazing girlfriend, Michelle, for always being there through the highs and lows. You endured listening to my thesis rants and cheering me up when I needed it the most.

As my journey at TU Delft comes to an end, I look forward to what the next chapter as a "burger" will bring me. One thing I have learned, though, is that with enough ice tea, anything is possible!

E.S. Gommers
Delft, November 2024

Abstract

As the structural engineering sector explores innovative materials such as Fibre Reinforced Polymer Composites (FRP), understanding their behavior under static and fatigue is critical. This thesis focuses on developing a numerical method to model the fatigue behavior of FRP composites, reducing the need for extensive experimental testing, resulting in a reduction of costs. Static and dynamic load tests were performed on Glass Fibre Reinforced Polymer (GFRP) coupons extracted from a vacuum-infused sandwich panel deck.

Based on these experimental test results, a numerical model was developed in Abaqus, integrating a VUSDFLD user subroutine to simulate stiffness degradation using a Continuum Damage Mechanics model. The model, which accounts for stress dependent stiffness degradation, was applied to coupons containing imperfections such as dimples from the manufacturing process, and without imperfections.

The research demonstrates promising results for higher load fatigue life predictions, with estimates within 10% of experimental results for both coupons with and without imperfections. However, at lower load levels, the model underestimates fatigue life by 85% for normal coupons and 30% for imperfection ones. These deviations highlight the need for further research, particularly at lower stress levels.

Despite the deviations at lower stress levels, this study presents an advancement in numerically predicting the fatigue life of FRP composites based on stiffness degradation, offering a cost-effective alternative to extensive experimental testing. The numerical model successfully integrates material degradation and manufacturing imperfections, providing valuable insights for the design and evaluation of composite structures subjected to fatigue loads. These findings also highlight the important role that imperfections play in fatigue performance. Future research should focus on optimizing the model, particularly at lower load levels, to enhance accuracy and increase its applicability. In conclusion, this study opens the door to more reliable, efficient, and improved use of FRP in structural applications, particularly in areas where fatigue behavior plays an important role.

Keywords: GFRP, FPC, FRP, Continuum Damage Mechanics, Progressive damage model, Fatigue, Material degradation, Stiffness degradation, Imperfections, Sandwich panel bridge decks, Vacuum-infusion, stress dependent, user subroutine, VUSDFLD, FEA

Contents

List of Figures

List of Tables

Nomenclature

Abbreviations

Abbreviation	Definition
CDM	Continuum Damage Mechanics
CFRP	Carbon Fibre Reinforced Polymer
CLD	Constant Life Diagram
CLT	Classical Laminate Theory
CoV	Coefficient of Variation
CT	Compact Tension
DIC	Digital Image Correlation
FDM	Fatigue Damage Model
FE	Finite Element
FEA	Finite Element Analysis
FLS	Fatigue Limit State
FRP	Fibre Reinforced Polymer
GFRP	Glass Fibre Reinforced Polymer
PU	Polyurethane
SCL	Simplified Cyclic Loading
SLERA	Strength-life equal rank assumption
S-N	Stress-Life
StDv	Standard Deviation
UD	Unidirectional
ULS	Ultimate Limit State

Symbols

Symbol	Definition	Unit
A	Area	[m^2 or mm^2]
D	Damage	[-]
E	Young's modulus	[Pa]
E_0	Undamaged Young's modulus	[Pa]
F	Force	[N]
f	Frequency	[Hz]
k	Stiffness	[N/mm]
L	Length	[m or mm]
N	Amount of cycles	[-]
R	Stress ratio	[-]
R_0	Initial residual strength	[Pa]
T	Temperature	[°C]
t	Time	[s]
V_f	Fibre volume fraction	[-]
V_m	Matrix volume fraction	[-]
w	Displacement	[m]
ϵ	Strain	[mm/mm]
ρ	Density	[kg/m^3]
ρ_c	Density composite	[kg/m^3]

Symbol	Definition	Unit
ρ_f	Density fibres	[kg/m^3]
ρ_m	Density matrix	[kg/m^3]
σ_r	Stress range	[Pa]
σ_a	Stress amplitude	[Pa]
σ_m	Mean stress	[Pa]
θ	Angle	[°]

1

Introduction

Historically dominated by steel and concrete, the bridge engineering industry is undergoing a large transition, driven by the need for more durable and sustainable materials. One of these materials is Fibre Reinforced Polymer (FRP) composites. FRP composites offer beneficial properties such as lightweight, resistant to environmental conditions, a high strength-to-weight ratio and a lot of design flexibility for creating creative shapes. Due to all these excellent properties, FRP composites are increasingly used in the bridge engineering, mainly on smaller scale bridges. Even though these bridges are already in use, research on this matter still continues. New fabrication techniques and material innovations are investigated, with the goal of improving the possibilities for building durable FRP bridge decks.

One of these new innovations is the ability to accurately model fatigue of multidirectional laminates. During the service life of a bridge, the structure will be exposed to a lot of fluctuation stresses due to several external factors such as traffic. Over time, this will cause fatigue failure to occur. One of the methods to examine the behavior of FRP composites in terms of fatigue resistance is by performing experiments in a laboratory. This does come with certain downsides, such as that fatigue tests can be very time-consuming, depending on the load and frequency of the tests. Another factor is the costs that are involved in running experiments, both in terms of material as the set-up and experienced personal. A preferred alternative method is to make use of numerical models to re-create the experiments.

Until the early 2000s, numerical models to predict fatigue life of FRP composites were very limited due to computational power restrictions and lack of ability to investigate different types of failures. In recent years, multiple researchers have looked into creating more advanced numerical models to predict the fatigue life of FRP composites. Studies focus on different failure mechanisms, such as matrix cracking, failure of individual fibres, or full failure of the composite. The researchers often use S-N curves or Constant Life Diagram (CLD) for implementing the reference fatigue life of the composite. There are multiple numerical approaches for simulating the cyclic loads such as the Simplified Cyclic Loading (SCL), Min-Max Analysis, and Cycle jump analysis. They all focus on maximum efficiency of accurate results in combination with efficient computational time. For this study, the SCL approach is used.

To thoroughly investigate the possibilities of this numerical method, a set of research questions is used as the foundation of the research. The primary research question that will be addressed is:

- How can fatigue in multidirectional composite laminates be modeled at the coupon level using computational methods?

To make it more manageable, the primary question is subdivided in multiple sub-questions that together will form the basis for answering the primary research question. The sub-questions are:

- What is the degradation behavior of multidirectional composite laminates at varying load levels?
- What role do geometrical imperfections play on the fatigue life of multidirectional laminate on coupon level?
- How can the degradation behavior of a coupon be modelled in Abaqus?

One of the production methods often used for sandwich panel bridge decks is vacuum infusion. This offers great advantages such as a minimum amount of voids within the composite. FiberCore is using and further developing a new lay-up approach, called a Z-shape, which makes use of overlapping layers of plies. Due to this method, a limited amount of thickness increases and dimples are created within the composite. These imperfections cause inhomogeneous stresses inside the material during fatigue testing. The influence of these imperfections will be investigated, and recreated in a numerical model. For this study, an approach based on stiffness degradation curves gathered from experimental results will be applied. The numerical model will be using a Continuum Damage Mechanics (CDM) model, focusing on stresses to determine the amount of damage per cycle for each element.

To answer the research questions, several actions were undertaken, beginning with experimental work. The objective of performing experiments in the lab was to gain insights in the rate and behavior of the stiffness degradation of the FRP composite. Instead of investigating the fatigue behavior on a structural level, it was investigated on a smaller scale in the form of coupons, cut out from the bridge deck. Tensile fatigue tests were performed on different load levels, ranging from low to high loads. The main focus of the experiments was in the longitudinal direction of the coupon. Several coupons contain local geometrical imperfections, such as dimples. The influence that these imperfections had on the fatigue life was mainly examined on an experimental level.

With all results gathered from experiments in the lab, an extensive analysis was performed. In addition to learning about the fatigue behavior of the coupons, a suitable method to replicate this damage behavior in a numerical model was investigated. This was required for the second part of the thesis, creating a numerical model of a coupon made out of GFRP composite which accurately describes the failure behavior, based on a predetermined damage model. After completion of all the above steps, a final conclusion could be drawn to the primary research question.

1.1. Report structure

This MSc Thesis consists out of seven main chapters. In Chapter 1, the topic is introduced, in combination with the problem and research questions that will be answered during the report. Chapter 2 provides background information in FRP, fatigue and relevant literature. Chapter 3 will go into the methodology used, looking at documentations and information regarding the materials tested and testing equipment used. This is followed by Chapter 4 that provides the results from the static tests that have been performed. The next phase after static tests is the fatigue tests. All results from the fatigue test are provided and analyzed in Chapter 5. The last chapter providing new detailed information is Chapter 6, containing the entire methodology and results of the Finite Element Analysis (FEA). Everything is wrapped up in Chapter 7, providing a conclusion, limitations of the study and recommendations for further research. This will be followed by the references and appendices.

2

Literature study

2.1. Introduction to FRP

The general definition of a composite material is a combination of two or more materials with different physical, mechanical and/or chemical properties which act in concert, yet remain separate and distinct at some level because they do not fully merge or dissolve into one another[1]. This applies to all sorts of materials such as metals, polymers and natural materials such as wood. The most commonly used composite nowadays is concrete. This building material is used for many structural applications, but due to its low tensile stress capacity it requires reinforcement in such that it will not instantly fail under a tensile loading. When adding this second material, you are talking about a composite.

An often occurring misinterpretation about FRP composites is that FRP composites are not suited for structural applications which require high strength and stiffness. But in fact, most FRP composites offer either similar or even better properties than conventional building materials such as steel. Composites in general have a very low density, creating a very high strength / weight ratio. This is a major advantage in weight-critical structures over for example steel or concrete alternatives. Depending on the matrix material you use, it can also have excellent resistance against environmental conditions such as varying moisture conditions. A use case where this is convenient is areas with a lot of rainfall interspersed with a lot of sunshine. Another option for this scenario is to apply a coating to the surface to ensure maximum resistance against environmental aspects.

There are a lot of methods to fabricate FRP composites, there are both open and closed mold processes which have different kind of (dis)advantages. Some often used techniques are filament winding, hand lay-up, vacuum infusion and pultrusion. Due to the way that FRP composites are fabricated, they allow for much more unconventional shapes to be produced. This is beneficial when the architect creates a unique design which is not practical to execute in steel. The advantage of FRP composites, which is the main subject material of this thesis, is the excellent resistance against fatigue. Besides the advantages, FRP composites also have some cons / points of attention that need to be kept in mind. Where steel has both elastic and plastic deformations before failure and is considered ductile, FRP composites have a more brittle failure, they do not yield a lot and have a more sudden failure. This should be taken into account in the design stage. Another thing to keep in mind is that FRP composites have a relatively low coefficient of thermal expansion, this on itself can be a very useful property, but can have a negative impact in combination with other components. If a component attached to the FRP composite has a higher thermal expansion coefficient, this can cause additional thermal stresses that were not accounted for in the design stage[17].

In general, FRP composites consist out of two different materials, there are fibres in combination with a matrix resin.

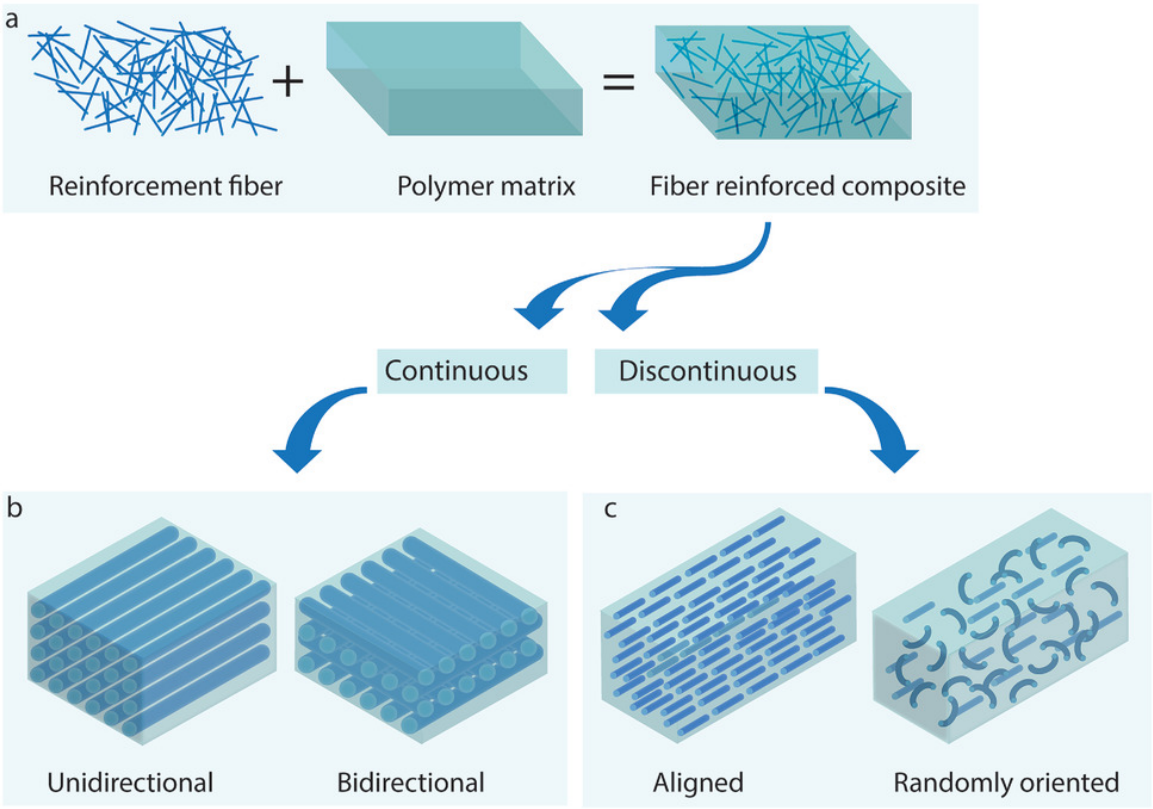

Figure 2.1: FRP build-up [16]

There is a wide range of materials for either of the two. For fibres the most commonly used materials are glass, carbon, and aramid (for most people known as Kevlar) fibres. Another option is organic fibres to create bio-composites, commonly used materials are cotton, flax, hemp, or wood. The primary function of the fibres is to provide the load-carrying function. As mentioned before there are different materials for the fibres, each with different properties such as tensile strength/modulus, elongation and density. In general, the synthetic fibres offer higher strength and stiffness but also require much more resources to produce. Therefore, bio-composites are the most environment friendly option. Depending on the use case, you should select the material that suits all needs.

As for the matrix, there are two types of polymer resin. There is a subdivision in thermoset and thermoplastic resin. Depending on the application, you choose one of the two. The main purpose of the matrix is to keep the fibres in place and make sure they are in the right orientation. But depending on the type of resin you choose, you can have additional benefits. For the thermoset resins you have polyester, vinyl, epoxy, bismaleimides, cyanate, polyamides en phenolics resin. Here, the type of resin also depends on the use case of the composite and the budget available. Polyester resin is extensively used in commercial applications since it is relatively inexpensive, while offering processing flexibility. The main characterization of thermosets is that once they are fully cured, the process is irreversible, they cannot be reprocessed even with heating up the material again. This can be either an advantage or disadvantage based on the usage. The five most used thermoplastic materials are Polyetheretherketone (PEEK), Polyetherketoneketone (PEKK), Polyetherimide (PEI), Polyphenylene Sulfide (PPS) and Polypropylene (PP). A characteristic of thermoplastics is that you can reshape it by reheating the material to the material processing temperature. This can be beneficial for recycling certain components for new projects at a later stage, but is also useful for joining the composite to other structures. This is not without a limitation, after a certain amount of times the polymer will degrade. On top of that, it

is also possible that due to reheating, the fibres get damaged from the heat. These point needs to be kept in mind.

Another important factor into the design of FRP composites is the lay-up of the composite. A composite always exists out of multiple layers of fibres. These fibres can be either continuous or discontinuous. The continuous fibres are only in one direction (unidirectional) but by using multiple layers in different directions you can have a certain pattern, for example bidirectional or multidirectional fibre patterns. Discontinuous fibres are chopped pieces of fibres aligned in all directions. A visualization of the different kinds of fibres can be found in Figure 2.1. Depending on the cost and strength required, you either choose for continuous or discontinuous fibres. In general, the fibres only provide a function in the direction of the fibre, they do not contribute to the (load-carrying) capacity in the perpendicular to the fibre direction. In this case the strength in the perpendicular (90°) comes from the matrix itself, but this is much weaker than the fibres, up to a factor of 40 depending on the materials you choose [15]. Due to this characteristic, the lay-up of the composite is very important. If all the fibres are arranged in unidirectional direction you will get an an-isotropic material, while in most applications you require an isotropic composite. This can be achieved by applying ply's with different fibre orientations. By balancing the ply's in all four directions you will create a quasi-isotropic lay-up, this can carry the loads equally in all directions. A comparison between a unidirectional lay-up versus a Quasi-Isotropic lay-up is given in Figure 2.2.

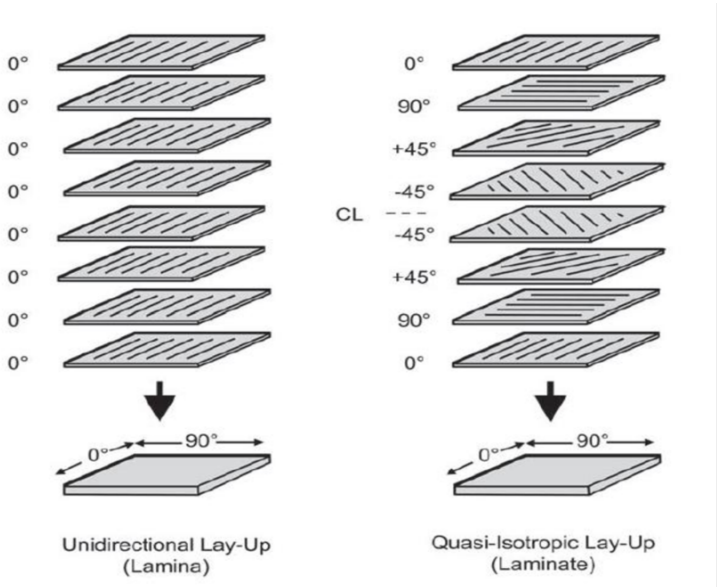

Figure 2.2: Unidirectional Lay-up vs Quasi-Isotropic Lay-up [5]

The fibres and matrix resin combined make the actual FRP composite. As mentioned earlier, they both serve a different function in the composite. Since they both have different mechanical properties, the actual FRP composite properties is a mix of both. This is dependent on multiple factors. One of the most important factors is the fibre volume fraction V_f. The fibre volume fraction defines the percentage of the composite that is made out of fibres. This influences mechanical properties such as strength and modulus of the composite, but also physical properties such as the density of the composite. An example of how the fibre volume fraction is used for the density of the composite is given in equation 2.1 where V_m is the matrix volume fraction and the ρ indicates the initial density of either the fibres or the matrix. It is important to note that working with the V_f is only accurate for a first estimation. In the actual designing stage, the properties should be determined based on mechanical properties testing.

$$\rho_c = \rho_f * V_f + \rho_m * V_m \tag{2.1}$$

2.2. Introduction to fatigue

As mentioned previously, one of the benefits of FRP composites compared to often used construction materials is the resistance to fatigue. A fatigue failure is a failure that occurs due to the application of a cyclic loading on the structure. This load will cause the fatigue crack to initiate. Three components are required for fatigue cracks to occur: [5]

- A maximum stress of a sufficiently high value
  - This peak stress should be high enough for a crack to occur.
- A large enough variation or fluctuation in the applied stress
  - This can be either in tension or compression and can change over time. but the stress range should be high enough.
- A sufficiently large number of cycles of the applied stress
  - This is largely dependent on the requirements above, depending on those criteria the amount of cycles can be either lower or higher before a crack initiation occurs. A very low tensile stress will never cause fatigue cracks even after millions of cycles, while a very high tensile stress can cause a fatigue crack with a relatively low amount of cycles.

There are several types of varying cyclic loads that can cause failure. Typical fatigue loading cycles are given in Figure 2.3.

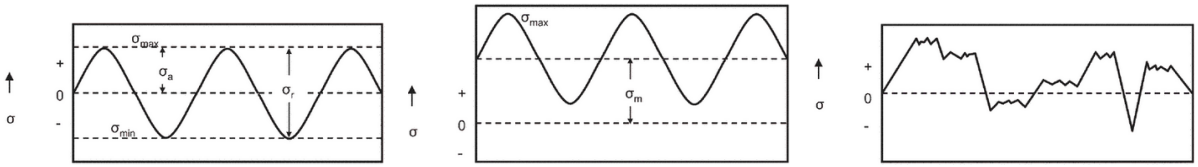

(a) Fully reversed loading **(b)** Tension-Tension with applied stress **(c)** Random loading

Figure 2.3: Typical cyclic loading patterns

The fully reversed loading shows uniform peaks in both compression and tension, but this does not necessary have to be the case. The stresses can also differ from each other. The cycle given in Figure 2.3b shows tension stresses only, but the same scenario is also possible in the compression domain. The last loading gives a random pattern during service, this scenario is valid for example on a bridge deck with different type of vehicles passing by. This can be either tension only, compression only, or both during one cycle. The cycle contains several parameters which are relevant to determine. You have the stress range, which is given by equation 2.2. This describes the total difference between the minimum en maximum stress.

$$\sigma_r = \sigma_{max} - \sigma_{min} \tag{2.2}$$

The stress amplitude describes the difference between the mean stress and the peak stress, either the maximum or the minimum, they are both equivalent. You determine it with the help of equation 2.3

$$\sigma_a = \frac{\sigma_{max} - \sigma_{min}}{2} \tag{2.3}$$

The mean stress indicates the average of the minimum and maximum stress in one cycle. The reference level is the neutral axis. This mean stress is not the same as the amplitude, as can be seen in figure 2.3. You determine it with equation 2.4.

$$\sigma_m = \frac{\sigma_{max} + \sigma_{min}}{2} \tag{2.4}$$

Besides the actual values of the stresses, sometimes a clear indication of the ratio between two stresses can also be very insightful. An often used ratio for this is the stress ratio (eq. 2.5)By using this ratio, you can compare and present the data in a clear manner. With the stress ratio (eq. 2.5) you can indicate what kind of cycle you are dealing with: R = 0, cyclic tension loading; R = -1, fully reversed cyclic loading

and R = ∞, cyclic compression loading. If the stress is never fully removed, you have $0 < R < 1$ or $-1 < R < 0$ which indicates a fluctuating stress with either a minimum tensile or compressive stress with lower magnitude than the maximum stress.

$$R = \frac{\sigma_{min}}{\sigma_{max}} \tag{2.5}$$

2.3. Literature review

Fatigue in composites is a well known issue since the introduction of FRP in the engineering industry, dating back several decades when it was first used in the aerospace industry. That is why initial studies for fatigue behavior in GFRP in the sixties and seventies were mostly focused on aircraft components [11]. As new composites, such as CFRP, were introduced, studies started on these materials as well. These studies were mainly experimental and focused on different types of cyclic loading patterns such as tensile, compressive, flexural, torsion and shear loading. The main focus for these studies was the durability and behavior of the composites.

Starting from the eighties, different sectors, such as the automotive and civil engineering sector, started investigating and exploring FRP composites for new applications. Especially the civil engineering sector had to deal a lot with fatigue failure in structures, such as bridges that made use of FRP for reinforcement purposes. Therefore, it was required for more intensive studies into environmental conditions such as moisture and temperature, which play an important role in outdoor applications [13]. The goal was still to investigate the fatigue behavior of the composites over a longer period of time, based on experimental results.

Nowadays, FRP composites are applied in numerous sectors and applications. It is used for the current renewable energy transition that is trending, has a lot of applications in the infrastructure, marine applications, and also the fields in which it is already applied for a long time, such as aerospace, automotive and civil engineering sectors. Besides the application in new components, also new possibilities are investigated in terms of materials compositions and production methods. This can be expressed in new fibre volume fractions, new materials, or new processes and methods before or during production.

Fatigue behavior of the material still plays an important role for all these cases, which is why the research into all sorts of failure mechanisms has increased. The biggest challenge of all these new techniques is the fact that a lot of information regarding the material is unknown again. A lot of these new unknowns can be uncovered by performing lots of experimental tests in labs. This however comes with a new downside. Performing experimental results is very time-consuming and expensive. It requires the production of materials, including all the material itself, personnel to operate the machines, and equipment specifically designed for performing the tests. That is why currently a new innovation is being widely researched, the possibility to create numerical life prediction models for fatigue failure mechanisms of FRP composites. The goal is to limit the amount of experimental tests that need to be performed.

There are countless different fatigue damage models available to determine the service life of a structure. According to Degrieck and Van Paepegem [9], you can divide these models in three categories, namely *fatigue life* models, *phenomenological* models and *progressive damage* models. In order to determine which model will be used for this research, it is important to know the differences between each model.

The fatigue life models are using the so called *S-N* curves or Goodman-type diagrams, based on these a fatigue failure criterion is proposed. The *S-N* curves depict the amount of cycles compared to the stress range, while the Goodman-type diagram generally depicts the mean stress compared to the alternating stress. What should be kept in mind is that these *S-N* curves do not take into account degradation mechanisms of the material, such as matrix cracks and fibre fractures. They only predict the number of cycles it takes for fatigue failure to occur under fixed loading conditions. In order to determine these *S-N* curves, a lot of experimental testing in the lab needs to be performed. This can be very time-consuming and also expensive, therefore it is not always the best option to choose. One of the studies looking into this approach for coupons and joints is performed by S. Sarkani [20].

Secondly, you have *phenomenological* models. This type of model describes the fatigue life of composites as well, but compared to the *fatigue life* model based on the *S-N* curves, this method also takes

into account the deterioration of the material. The main focus of the deterioration is on the residual stiffness and/or strength of the composite, there are different models for each of them. As for the first type of models, they focus on the degradation of elastic properties of the composite during fatigue loading. The variable used for this stiffness loss is the variable *D*. The total damage is then described as

$$D = 1 - \frac{E}{E_0} \tag{2.6}$$

where E_0 is the undamaged modulus and E is the observed modulus of elasticity. When the damage variable *D* approaches closer to 1, it indicates that there is increasing failure. Full failure is the case when *D* is 1. This variable *D* is used in many fatigue models from different researchers. It is also applied for different predictions, such as the damage growth rate $\frac{dD}{dN}$.

As for the residual strength models, there are two different types, the *sudden death* model and the *wearout* model. They each describe a different behavior. As the name suggests, a *sudden death* model focuses on the occurrence of a sudden fatigue failure. This can be achieved by applying a high stress level, by doing so initially the residual strength remains nearly constant, but as soon as the failure initiates, the amount of cycles decrease rapidly resulting in a *sudden death*. Besides this sudden failure, there is also the possibility of a more gradual fatigue failure. In order to get this kind of failure you apply a lower stress level so that over time the residual strength gradually degrades, this method is referred to as the *wearout* model. This failure model takes longer to test since it will have many more cycles before failure compared to the *sudden death* model. There are different applications for each method, in general the *sudden death* model is applied to high-strength unidirectional composites [22] whereas the *wearout* model is applied for a lot of composites.

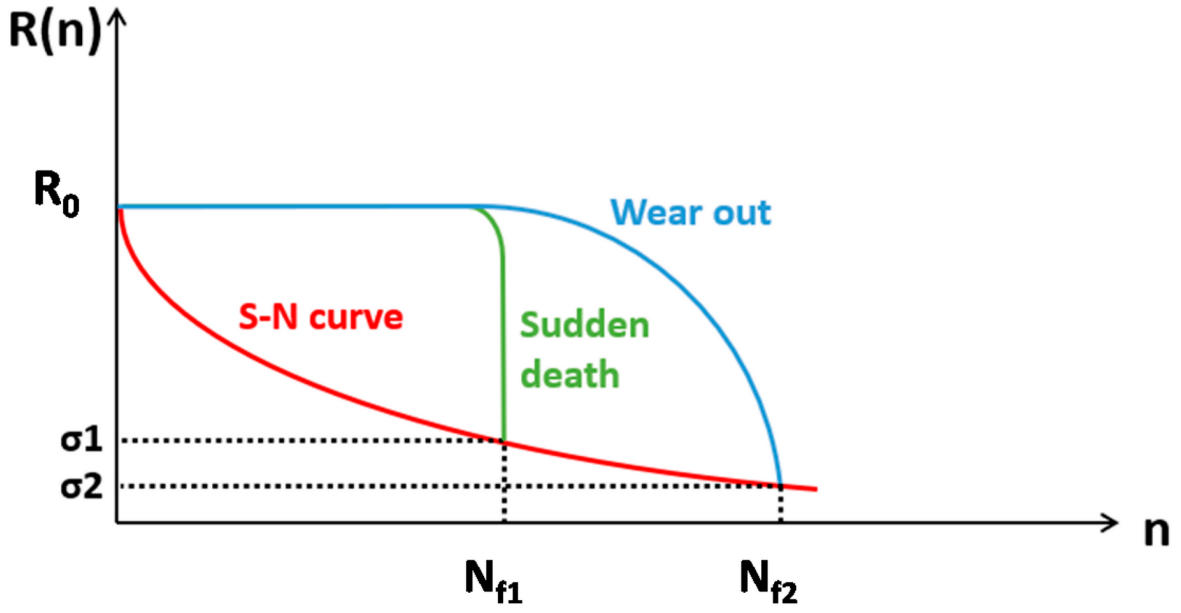

Figure 2.4: Schematic representation of the strength degradation under variable stress conditions [22]

A schematic representation of the difference between the *sudden death* and *wearout* model is given in Figure 2.4. You start with the initial residual strength R_0 which is constant for the initial period until it starts to drop off, this continues until it has reached the maximum applied stress σ. In Figure 2.4 you can see that the point of failure ($R(N_f)$) occurs at the intersection between the residual strength and the stress. Furthermore, you can see that a lower stress level $\sigma 2$ results in more cycles until failure and also a more gradual failure, which is in accordance with what you would expect. *Wearout* models generally state that stronger specimens are likely to have longer fatigue lives or higher residual strength at runout [22], this is often referred to as the *Strength-life equal rank assumption* (SLERA) by Chou and Croman [6].

The last category of fatigue models considered here is the *progressive damage* model. This kind of model is comparable to the above-mentioned models, but deviates in the fact that one or more properly chosen damage variables are introduced. These new variables describe the material deterioration of the composite component. There are two distinct damage model classes: models which predict the damage accumulation of specific damage types in terms of physically observable phenomenon (such as the size of the delaminated area or the number of transverse matrix cracks per unit length) and those which correlate the damage growth with the residual mechanical properties (based on stiffness/strength, comparable with the *phenomenological* models) of the laminate [9]. When using this method, it is possible to see the material properties, such as the stiffness, degrade gradually as the damage accumulation in the material increases. This damage increase can for example be defined based on local stress levels.

One of the studies that is looking into damage accumulation in CFRP composites, focusing on the numerical modeling part, is conducted by Brod et al. [4]. This study primarily focuses on bending test for coupons, looking into the deflections of the coupons. A finite element model is created, in which inhomogeneous stresses are present, resulting in damage accumulation as the fatigue tests progress. For validation, experimental tests are performed and compared against the numerical results as well. The focus of this study is only on matrix cracking and deformations of the material, it does not look into the next phase of fibre failure and eventual full failure of the specimen.

The same research group has looked into the numerical life prediction of UD fibre composites under block loading conditions while using a progressive fatigue damage model (FDM) [3]. Again, the material considered is CFRP, here orientated in UD direction. In this study, the block loading patterns are representing different stress amplitudes, mean stresses and load orientations. These different stresses are meant to imitate the different types of stresses that are present in a structure, which accelerate or decelerate the amount of damage that is being done during this process. They also focus on the effects due to combining tensile and compressive loads, resulting in a special damaging effect. This damage is expressed in terms of degraded stiffness and strength.

Both studies found focus on creating a numerical model which focus on progressive FDM's for CFRP. Both use experimental results for validation purposes, even though the second study uses results from a different research. There are some mentions regarding inhomogeneous stresses in the first study, but this is mainly due to the fixed clamping on both sides of the specimen, increasing the inhomogeneous stresses [8]. Furthermore, this study only focuses on the initial matrix cracking and leaves out predicting full failure.

The approach is to first obtain stresses and failure strains from FE analysis, and continue tweaking the model based on these numbers. For reference of the fatigue life properties, the failure is based on Stress Life curves and Constant Life Diagrams. This differs from the approach in this study, where the failure will be based on stiffness degradation curves originating from experimental results.

What is left out in both studies, is the application of this FDM on coupons containing geometrical imperfections that will result in increasing local stress concentrations. This is one of the applications that will provide a good validation to see if damage does increase by high local stress concentrations.

A recent study performed by Joosten et al. [14] is focusing on a computational approach to measure laminate fatigue damage initiation and propagation for different failure mechanisms and load combinations. It presents multiple methods for numerical approaches to represent the cyclic loads in a fatigue analysis, including the simplified cyclic loading (SCL) approach that will be used for this study. Other methods described are the Min-Max Analysis, which is based on co-simulation using twin models, and the cycle jump approach. There are a number of studies using the SCL approach, for example this study by Dávila [7]. The method chosen here is the cycle jump strategy, which is a more efficient method to perform a fatigue cycle analysis. It reduces the amount of full sinusoidal function cycles that need to be performed by calculating the damage done during one cycle, and extrapolate this over a certain interval of cycles. Once this interval is done, this same approach is repeated until failure is reached.

In fatigue tests of FRP composites, the fibre volume fraction, V_f, plays an important role in the fatigue life of the material. The influence for both static and fatigue tests is investigated by multiple researchers, trying to see if there is a limit at which it no longer is beneficial. In general, the higher the V_f is, the

better the static performance is, especially in terms of tensile strength. This is because at increased V_f, the fibres take up more of the load bearing function, reducing the stresses on the matrix [23]. The fibres itself have a much higher capacity compared to the matrix. As for the fatigue performance at multiple fibre volume fraction levels, researchers came to a different conclusion.

There are two stages with different implications for the fatigue life. In a certain range, the increase in V_f results in positive fatigue performance. However, there is a threshold at which the influence of increased V_f starts to work counterproductive on the fatigue life. The optimum value for the fibre volume fraction is 45 to 60% while exceeding this limit causes strength to reduce due to the lack of insufficient resin to transfer the load to the fibres effectively [12][2]. This is in direct relation with the increase of interface stresses found by Flore et al. [10]. The increase in V_f also resulted in different kinds of failure modes. For lower fractions, the failure modes were mainly matrix cracking and fibre-matrix debonding, while for higher fractions, the main failure mode was fibre pullout.

3

Testing methodology

Part of this research consists of performing tests in the lab on smaller coupons to look at local fatigue failure. The coupons for this research are gathered from GFRP bridge decks as shown in Figure 3.1. These decks are so-called sandwich panel decks, which consist out of two facings and a web with a foam core within the facings. These GFRP bridge decks are manufactured with vacuum-infused GFRP panels and polyurethane resin that has a core of polyurethane (PU) foam.

Figure 3.1: GFRP Bridge decks

3.1. Material properties

The decks are made out of Glass Fiber-polymer Composites also known as GFRP. Since we are dealing with composites, it means it is a combination of two or more materials, in this case E-glass fibers and polyurethane resin. A large contributing factor for the material strength of the composite is depending on the lay-up of all the plies, especially the fibre orientation for each layer. The lay-up of the facings and web are:

- Top facing - $[((0°/90°)_2/0°_3)_4/0°/90°/\pm 45°]$
- Web - $[\pm 45°_2/(0°/90°)_2/\pm 45°_2]$
- Bottom facing - $[((0°/90°)_2/0°_3)_4/0°/90°/\pm 45°]$

Both the top and bottom facing are identical to each other, they consist out of 32 layers in total. Most of the layers in the facings are unidirectional (UD), $\frac{21}{32} \cdot 100 = 65\%$ of the layers are in longitudinal direction. The rest of the fibres are perpendicular, except for one layer of $\pm 45°$. This layer is located at the outer layers of the facings which face the foam core, these PU foam blocks are wrapped with these E-glass fibres. Since the amount of fibres orientated in each direction is not equal the material properties are an-isotropic, they are given in Table 3.1. These properties are determined by the bridge deck manufacturer based on standard material tests. There is a difference in fiber volume fraction (V_f)

between the facings and the webs. The webs contain only 12 layers in total while having a similar thickness, resulting in a much lower V_f. Table 3.1 also contains the properties of the webs, but these are purely informational since the coupons are only extracted from the facings.

Table 3.1: Material properties of FRP plies

Property	Elastic FRP UD ply - Vf = 54% - in facings	Elastic FRP UD ply – Vf = 27% - in webs
Longitudinal modulus, E1 [GPa]	42	22
Transverse modulus, E2 [GPa]	14.5	8
Shear modulus, G12 [GPa]	4.2	3.5
Poisson's ratio, ν_{12} [-]	0.27	0.27
Density, ρ [kg/m3]	1962	1576
Longitudinal tensile strength, σ_{T1} [MPa]	855	327
Transverse tensile strength, σ_{T2} [MPa]	59	24
Longitudinal compressive strength, σ_{C1} [MPa]	395	410
Transverse compressive strength, σ_{C2} [MPa]	138	130
Shear strength, τ_{12} [MPa]	39	32
Interlaminar shear strength, τ_{13} [MPa]	51	33

3.1.1. Production method

The manufacturer of the bridge decks is the company FiberCore, a large manufacturer mainly specialized in producing bridge decks and lock gates. The deck in question is produced via vacuum-infusion, which is one of the most used techniques for creating decks on such scales. First, a mold of the deck is created in which layers of the dry glass fibres are arranged according to the lay-up specialized in the design. After the entire lay-up is completed, the entire mold will be sealed with a flexible vacuum bag. This allows to remove all the air from the mold by creating a vacuum. Once everything is set, liquid resin will be infused in the mold. Due to the vacuum environment, the resin can be evenly distributed across the entire deck. The last step is to cure the resin until it is fully hardened.

Using vacuum infusion for producing the deck comes with several advantages and disadvantages. One of the biggest advantages is that since this method relies on a vacuum environment, the amount of voids within the composite is minimized. Since production happens indoors, and in a vacuum, the environment is controlled, leaving less room for environmental factors affecting the durability of the deck.

There are also a few disadvantages when choosing for vacuum-infusion. The entire process is taking place in a mold, which has a flat surface at the bottom. At the topside, however, the vacuum bag will be present. When a full vacuum is reached, the top surface is not completely flat. This can result in local varying thickness differences, while ideally you want a uniform thickness over the entire deck. In general, the preference is to have a flat surface. That is why during production, the deck will be build upside down. This ensures that the top facing will be flat, while possible imperfections occur at the bottom. In addition to this, in order to spread the resin through the entire deck as effective as possible, tubes are inserted in the deck at several locations. Surrounding the entry points of these tubes, resin does not always stay very effectively, resulting in local imperfections as well.

For this deck, the thickness of the facings is 10 mm, but as mentioned previously, this can vary locally due to the way they are produced. Another factor influencing the thickness of the facings is the method of lay-up. For these panels a Z-shape lay-up was used for two $[0°/90°]$ layers, this Z-shape goes from the top facing towards the bottom facing via the webs. At those facings, it has an overlap of 2.5 blocks. This locally induces thickness bumps at locations where there is more overlap. The UD layers at the facings do not have this Z-shape layup, they stay on one side and have an overlap of 2 blocks each.

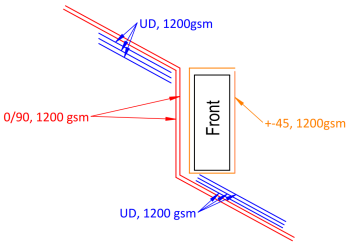

Figure 3.2: Z-shape lay-up

3.2. Geometry of the coupons

A total of 64 coupons have been cut out from two GFRP composite bridge decks. These coupons are designed based on specific guidelines in order to have representative test data. The main reason why the dimensions of the coupon are deviating from the standard coupon sizes is due to the thickness of the facings. The facings have an overall thickness of 10 millimeters, which is relatively thick for coupons. The risk of having these thick coupons is that it can cause non-uniform stresses throughout the coupon if there is no sufficient area to transfer the load over. The guideline document that was used in order to help determine the specific dimensions of the coupons is NEN-EN-ISO 527-4:2023 [18]. This code prescribes multiple types of specimen with different shapes and dimensions that can be used. For this research project, it was decided to continue with Type 4 specimens. The thickness range for which type 4 is applicable is between 2 and 10 millimeters, so the thickness of the bridge deck is just within this outer limit. Type 4 coupons are defined as indicated in Figure 3.3.

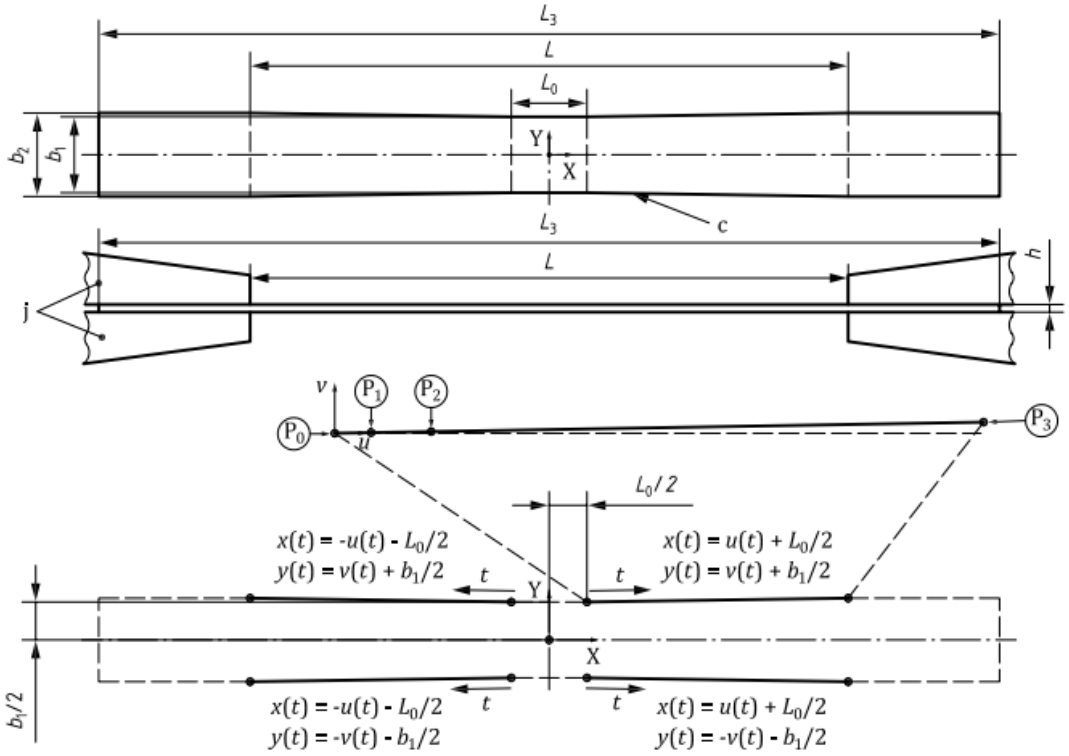

Figure 3.3: Type 4 specimen [18]

There are multiple parameters and requirements for this type as given in Table 3.2

Symbol	Name	Dimensions in millimeters
		Type 4
L_3	Total length	≥300
b_1	Width of parallel mid-section	25 ± 0.5
b_2	Width at ends	28 ± 0.5
H	Thickness	2 to 10
L_0	Gauge length (recommended for extensometers)	25 ± 1
L	Initial distance in between grips (nominal)	200
P_0	Bézier curve control point in (u, v) coordinates	(0; 0)
P_1	Bézier curve control point in (u, v) coordinates	(4.86; 0)
P_2	Bézier curve control point in (u, v) coordinates	(13.0; 0)
P_3	Bézier curve control point in (u, v) coordinates	(87.5; 1.5)
c	Edge is a Bézier curve	
j	Clamping jaws	

Table 3.2: Requirements Type 4 specimen [18]

Based on these requirements, the initial design for the coupons was made. Following this, the design was tested in Abaqus to see the general behavior of the coupon and to get an indication of the force at failure. When performing the test, it is convenient to have an idea of the location of failure in order to better analyze during the test, especially when the test is performed without a Digital Image Correlation (DIC) system. This is due to the fact that measuring devices such as an extensometer accurately measure at the location they are placed, but less when the failure occurs outside this region. Therefore, the design was made such to influence the location of failure as much as possible. In the middle of the coupon a gauge length L_0 of 35 millimeters was taken which had a decreased width of 25 millimeters compared to the 28 millimeters width of the rest of the coupon. In order to transform from one width to another, the standard uses the Bézier curves. This curve allows determining a polyline which smoothly transitions between the two widths. However, after running the model with and without the Bézier curve as a transition, it was noted that the impact of this curve was insignificant. This on top of that it would give an extra challenge with the cutting of the coupons resulted in the decision to use straight lines for the transition instead. The final coupon dimensions are given in Figure 3.4

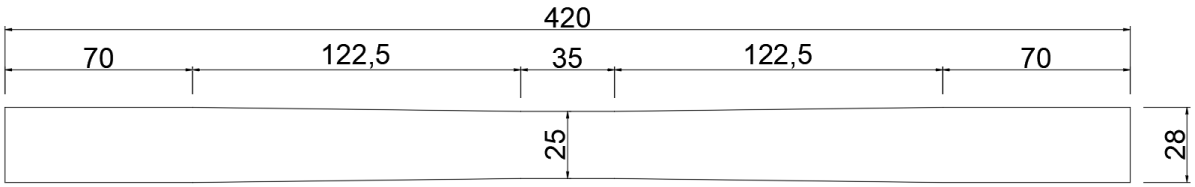

Figure 3.4: Final coupon dimensions

The total length of the coupon is 420 mm, this is longer than most coupons, but since the Dowty Rotel Rig clamp spacing can be adjusted as desired this was no problem for testing. Noticeable is that the end at both sides contain a straight part of 70 mm, this region is where the clamps will be located such that they have a large enough surface with a uniform width. This also decreases the chance of failure of the coupon in the clamping region. Starting from 70 mm is the transition from 28 to 25 mm, the total decrease per side is only 1.5 mm, which is minimal compared to the length of 122.5 mm in which this transition is done. As mentioned before, the middle of the coupon contains a gauge length of 35 mm, in which hopefully the failure will occur. Since the cross-sectional area is the lowest here, this will induce the highest stresses in the coupon, resulting in failure of the coupon.

3.3. Method of cutting

As mentioned in section 3.2 a total of 64 coupons are extracted from two separate bridge decks. All coupons are originating from the top and bottom facings, but before the large decks could be cut into smaller coupons, first the polyurethane (PU) foam core needed to be removed. This was still attached to the facings. The removing of the PU foam was done by hand (Figure 3.5).

Figure 3.5: Removal of PU foam

After all the foam was removed (as can be seen at the bottom of Figure 3.5) the facings could be cut into smaller samples. The method of extracting the coupons that was used is water jet cutting, which was outsourced to an external company. Water jet cutting provides an accurate method of cutting the coupons from the facings by using a concentrated water jet with high-pressure. One of the benefits of this method in combination with FRP is that there is no generation of high temperatures within the material, which can possibly affect the composite material properties. An additional benefit is the fact that it can also cut more complex shapes, such as the coupon with specific curves.

After determining the geometry of the coupons (as explained in section 3.2) it was necessary to determine the path of cutting, such that the company could cut all coupons from the panels in one continuous process. One important factor that needed to be taken into account was the direction of the fibres such that all the UD plies were facing the longitudinal direction of the coupon. Since the facings were already cut in segments of approximately 70 mm x 1200 mm, with the UD fibers in the longitudinal direction of the facing, this was already implemented. The resulting pattern is shown in Figure 3.6.

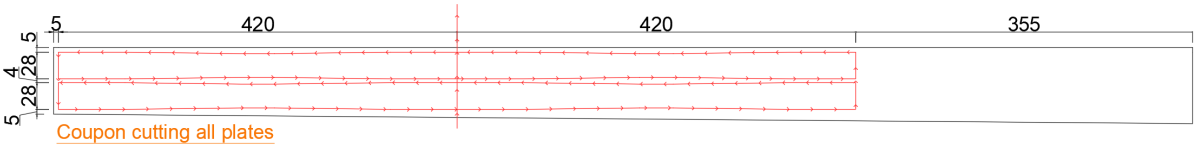

Figure 3.6: Coupons cutting pattern

A maximum of four coupons could be cut per plate, with a total of 16 plates, resulting in 64 coupons in total. The remaining segment of the plate was kept for the possibility to create CT-models for a possible follow-up study. There was one plate that was deviating from the rest, this contained a lot of imperfections near the middle. Therefore, this pattern was changed to the design given in Figure 3.7, this had to be done in two steps.

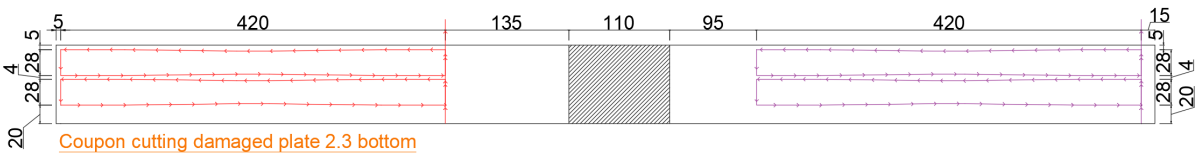

Figure 3.7: Coupon cutting damaged plate

3.4. Surface preparation

After the arrival of the coupons in the lab, the next step in the process was to prepare the surface. It still contained bits of PU foam at one side of the coupon which needed to be removed. This was done with sanding paper with different types of fine coatings. Besides PU foam there was also still resin residue present on the surface, this had to be removed with a sharp chisel to not damage the underlying plies of fibres and/or resin.

Figure 3.8: Surface preparation

Having a smooth surface is beneficial for multiple reasons. The largest benefit is that the clamping area is flat, ensuring that the clamping force is evenly distributed over the surface. If this is not the case, it can cause high local stresses, resulting in the failure in the clamp region. Another benefit is that the surface is well suited for applying a DIC pattern (explained more in depth in section 3.7) when the surface is smooth and flat.

3.5. Inventory

In order to make the analyzing of the data from all the specimens as convenient and insightful as possible, a system was introduced to name all the coupons individually. The system will be explained with an example. The coupon in question is PU 1.2_03T, which is shown in Figure 3.9.

Figure 3.9: Coupon PU 1.2_03T

The *PU* is a reference to the material of the deck and foam, this is the same for all the specimens in this case. The first number is a reference to the deck from which the coupon is originating from, in this case deck 1 out of 2 decks. From each deck a total of eight plates were extracted, four plates from the top facing and four plates from the bottom facing, the web part will not be tested. The second number indicates from which plate the coupon is originating, so in the example this is plate 2. The last

number indicates the coupon number from the plate, each plate was large enough to cut four coupons from (Figure 3.6). In this example, the coupon is the third coupon from the plate in question. The last letter indicates if the coupon is from either the top (T) or bottom (B) plate. In total there are 64 coupons extracted from the two bridge decks which are going to be used for both static and dynamic (fatigue) tests. With all coupons being distinguishable, the next necessary step was to document all coupons.

3.6. Documentation

The final step before the focus could be shifted to testing of the coupons is documenting all dimensions and where applicable the imperfections of each of the coupons. Therefore, a database was created in Excel in which all relevant information was bundled. An overview of the information provided is:

- Coupon name
- Type of test performed on the coupon
- Order in which the tests were performed
- Additional notes
- Width and thickness at 3 locations
- In case of imperfections
  - Type of imperfection
  - Location of imperfection
  - Width and thickness at location of imperfection
  - Width and thickness around the imperfection
- Type of failure

As listed above, the width and thickness are measured at multiple locations. The exact locations of the measurements are shown in Figure 3.10.

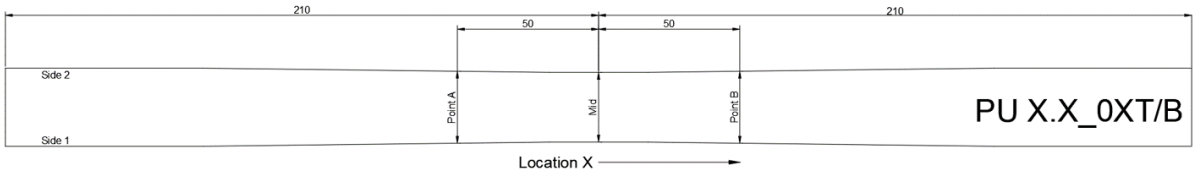

Figure 3.10: Locations of measuring coupon width + thickness

The locations measured are in the middle of the coupon and at ± 50 mm from the middle. Additionally, if imperfections were detected, three extra locations were measured, at the location of the imperfection and ± 15 mm from the imperfection. After a quick inspection, it became clear that the coupons have differences in thickness between the sides. Therefore, for the thickness, both sides were measured to establish an average thickness which later on will be used for calculations etc. These measurements were performed with a digital caliper with an accuracy of 0.01 mm. A full overview of the database is included in the Annex A.

On top of writing down all the information regarding the coupons, pictures of the coupons before testing were taken as well. This in order to later being able to retrace the imperfections when analyzing the data, not only relying on the measurements but also on photographic evidence. An overview of all the coupons after surface preparation, labeling and measuring is given in Figure 3.11.

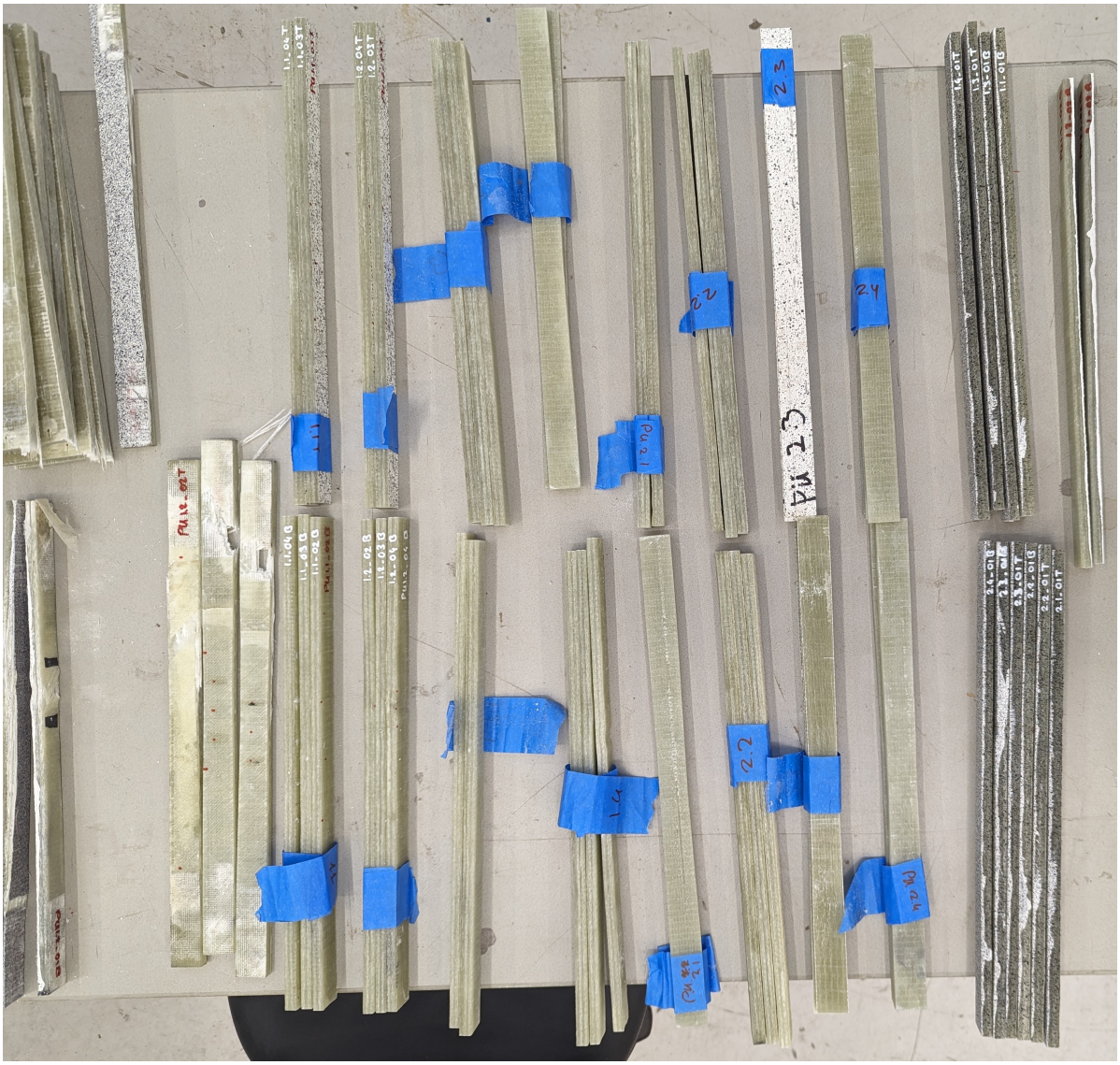

Figure 3.11: All coupons before testing

3.7. Test equipment

All coupon tests were performed on the Dowty Rotel Rig (shown in Figure 3.12), which is located in the south hall of the Stevinlab II at the TU Delft University. This machine is capable of performing compressive/tensile static and dynamic tests up to 250 tons. The choice was made to use this machine because the Dowty was the best machine available, which also features the correct clamps in terms of thickness requirements for the coupons. The clamps of the machine are flat wedge grips which are operating on hydraulic pressure, by firmly applying this pressure it is ensured that the coupons are held firmly in place. The machine is operated either directly from the machine terminal itself, or via the computer with the accompanying software. You can choose for either displacement controlled or force controlled guidance of the machine. Depending on the sort of test ran, this will differ. It will be mentioned which method is applied for which test. The software which controls the machine is also responsible for recording all the measurements. The machine measures several parameters such

Figure 3.12: Dowty Rotel Rig

as the force exerted on the coupon F [kN], strain in the coupon $\varepsilon[\%]$, stiffness k [N/m], displacement of the clamps since start of the test w [mm], amount of cycles N [-] (where applicable), time passed t [second] and frequency f [Hz] (where applicable). All this gathered data is crucial for post-processing the results of the coupon tests. As for the testing conditions, the temperature during testing will be at room temperature, which is present in the entire lab. The humidity is not regulated, but is assumed to be normal.

Besides measurements from the machine itself, external measuring devices are also used. One of the devices used is an extensometer from Instron shown in Figure 3.13. This device measures the strain accurately at the location of the device but also of the general coupon. By placing this at the location of the expected failure, accurate data of the strain is monitored/captured. The extensometer has a gauge length of 50 mm in which the strain is measured, if the failure occurs outside this area it may capture the strain less effective. Both for static and dynamic tests, the extensometer can be applied on the coupon. This also allowed for an accurate determination of the stiffness degradation over time. The extensometer is attached to the coupon with springs which keep it in place at the right location. The placement of the extensometer is determined beforehand such that it is located at the predicted location of failure. This is either in the middle when there are no imperfections present, or otherwise near imperfections such as dimples and/or kinks in the coupon. At both ends of the extensometer arms are small blades which have the purpose of keeping the extensometer in place as well. In order to prevent the blades from cutting in the outer ply causing fibres to break, a layer of electrical tape is applied, such that the blades need to cut the tape first.

Figure 3.13: Extensometer Instron with gauge length of 50 mm

A second measurement system used for the static tests is Digital Image Correlation (DIC). With this method, a spray-painted pattern is applied at one flat surface of the coupon to get a distinctive surface. As soon as the coupon is placed in the machine, a camera is placed perpendicular to the coupon, which takes high quality pictures of the coupon as the test progresses. For this project only a single camera system was used, therefore the DIC data analyzing is only possible in 2D. During testing, the camera

will capture an image every second, allowing insights in how the stresses and cracks progress during the test. This will be done with the help of the software GOM Correlate, which is designed for DIC analyzing. A large benefit of this system is that the entire coupon surface is visible, ensuring that the failure will be captured regardless of where it will occur. A picture of the DIC system setup is shown in Figure 3.14a, with the accompanying spray-painted coupons shown in Figure 3.14b.

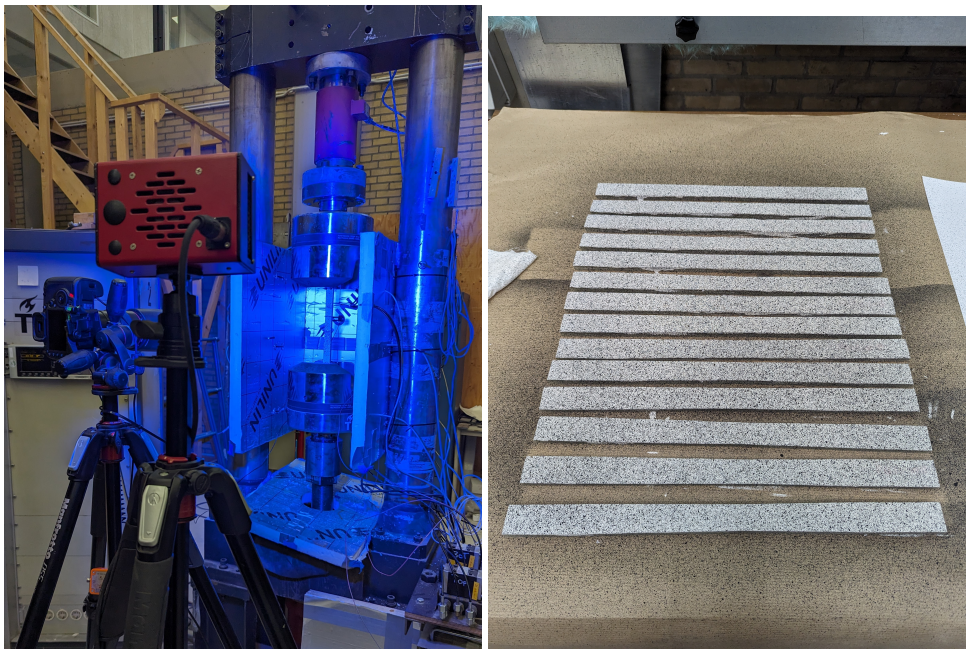

(a) (b)

Figure 3.14: DIC system, showing (a) the setup used and (b) the spray-painted coupons

4

Static tests

A large part of this research consists about gathering experimental data from tests in the lab. Both static and fatigue tests will be performed on GFRP composite coupons. First, static tests are performed, before the fatigue tests can start. All the gathered data from these tests will provide the foundation for the numerical model. First, the focus will be on static tests.

4.1. Static test results

With all coupons prepared and documented, the first step in the testing phase starts, the static tests. These tests consisted of tensile strength tests in the longitudinal direction of the fibres. The main objective of these tests was to determine the Ultimate Limit State (ULS) of the GFRP coupons. Based on the maximum tensile capacity, the different load levels for the follow-up dynamic tests will be determined. A test matrix was set up for these tests. The test matrix gives a clear indication in the amount of tests that will be performed and at which conditions the tests are run. For the static tests, this matrix is shown in Table 4.1.

Table 4.1: Test matrix for Static tests

Test type	Static (ULS)
Ratio	-
F_{max},kN	To be determined
Frequency, Hz	-
Temperature	Room (23 °C)
Speciments type	Non-aged and non-post cured
	Top facing/ Bottom facing (with imperfections)
Number of tests	3 + 3

As mentioned in section 3.7 the machine used for the static tests is the Dowty Rigid Rotel. The coupons are clamped at both ends by hydraulic clamping forces to make sure the coupon will not slip during testing. The machine is set to displacement control with a linear increase of one millimeter per minute (1 mm/min). There were two types of coupons that were tested statically, coupons with and without imperfections. The main objective was to determine the ULS of the coupons, but a different research question was coupled to this as well. It was interesting to see if the imperfections on the coupons had influence on the ULS during static tests or not, and if it had influence, how much this influence was. A total of seven coupons were tested for their tensile capacity. Three of these were without imperfections, and four contained imperfections, differing in the severeness of the imperfections. This deviates slightly from the original plan from the Test Matrix, an extra coupon with imperfections was tested, the reason for this will be addressed later.

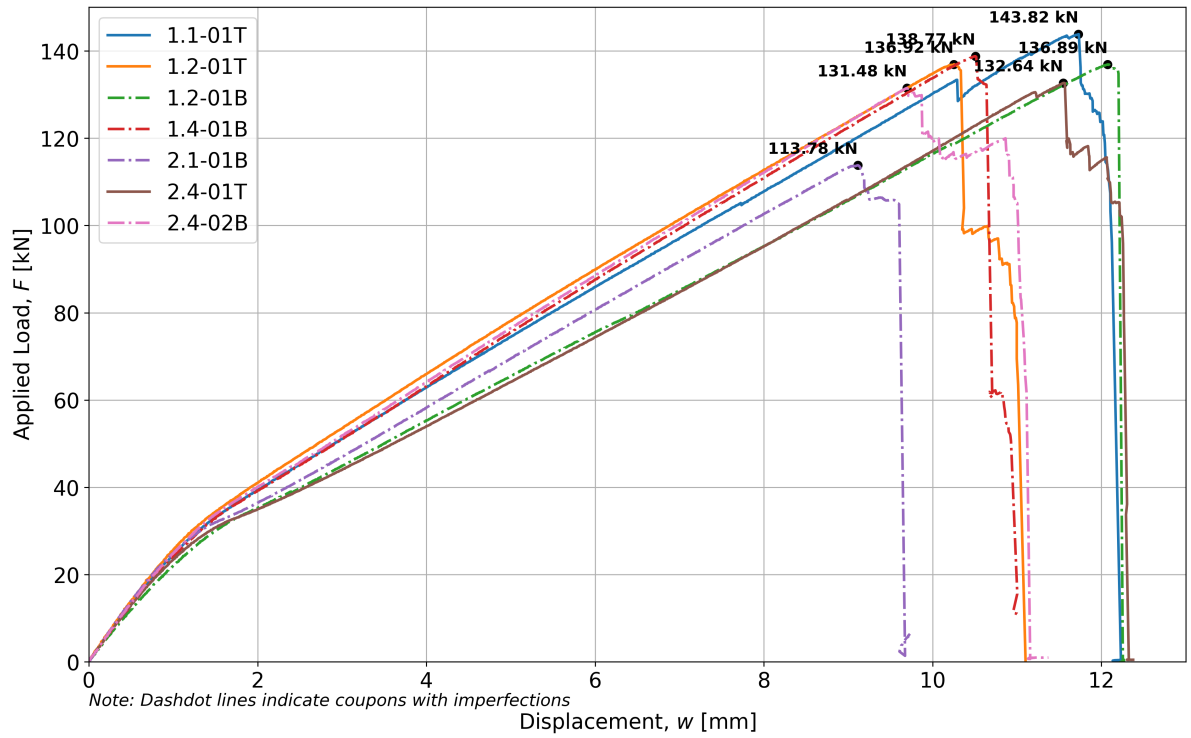

Figure 4.1: Load - Displacement curves from static testing

The graph in Figure 4.1 shows the results from the static tensile tests performed in the lab. It indicates the applied load during testing over the displacement that is constantly increasing with 1 mm/minute. All coupons show very similar behavior in terms of displacement versus applied load. There is one coupon that deviates from the rest. Coupon 2.1_01B fails before all others at 113.78 kN, respectively, while the failure limit of the other coupons is ranging between 130 kN and 140 kN. Coupon PU 2.1_01B is shown in Figure 4.2.

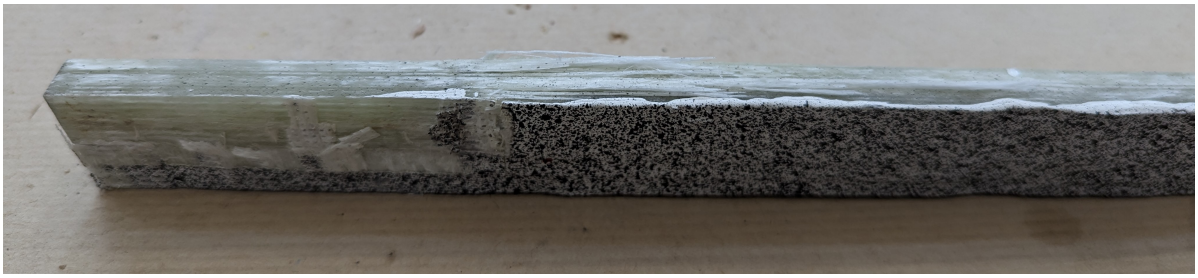

Figure 4.2: PU 2.1_01B after failure

After further inspection of the coupon, it becomes clear that the failure in this coupon first occurred in the clamping area of the coupon. Here, fibre breakage had started to occur in combination with the early stage of delamination. On top of that, the surface layer near the clamps started to break, therefore the test was stopped since this surface failure in the clamps resulted in slip. There also was not any failure visible in the region of the imperfection, so this factor did not have any influence on the ULS yet. Based on these findings, it was concluded that this test was not completed. Therefore, the decision was made to disregard the result from this test for the determination of the ULS. Tables 4.2 and 4.3 contain more detailed information regarding the static tests performed.

Table 4.2: Tensile coupon tests without imperfections, Static tests

Coupon	Failure Load, F_{max} [kN]	Failure Displacement, w_{max} [mm]	Failure Stress, σ_{max} [MPa]
1.1_01T	143.82	12.23	581.39
1.2_01T	136.92	11.10	604.02
2.4_01T	132.64	12.30	549.64
Average	137.79	11.88	578.35
StDv, σ	4.61	0.55	22.30
CoV, %	3.35	4.63	3.86

Table 4.2 contains the three tests performed on the coupons without imperfections. All test specimens are originating from the top flange of the original deck, these contain little to none imperfections due to the fabrication method as mentioned in section 3.1.1. The average load applied on the coupons till failure is a force of 137.79 kN. The standard deviation (StDv) is 4.61, which is low. This indicates that the three loads are close to the mean, making it fair to assume that this is the overall ULS of the coupons without imperfections. The failure stress σ_{max} for these coupons appears to have more variation, with a StDv of 22.3 MPa. This is mainly due to the different cross-sectional areas for each of the coupons. But when looking at this in terms of the coefficient of variation (CoV), it is only varying 0.5% more compared to the failure load's coefficient of variation. Due to this, the three tests performed are all considered successful and no more coupons were tested for this specific case.

Table 4.3: Tensile coupon tests with imperfections, Static tests

Coupon	Failure Load, F_{max} [kN]	Failure Displacement, w_{max} [mm]	Failure Stress, σ_{max} [MPa]
1.2_01B	136.89	12.25	685.27
1.4_01B	138.77	11.00	682.50
2.1_01B*	113.78	9.11	453.49
2.4_02B	131.48	11.16	587.07
Average	135.71	11.47	651.61
StDv, σ	3.09	0.56	45.65
CoV, %	2.28	4.88	7.01

* Stopped due to failure in clamps, not taken into account for data below

Table 4.3 contains all the results from the coupons with imperfections that were successful. At first glance the failure load of all the coupons is very similar in the region of 130 to 140 kN as well. When looking at the average Failure Load this is set at 135.71 kN, this is only 2 kN lower than the coupons without imperfections. Here, the standard deviation is 3.09, which indicates the results are even more in line with each other. When converting the applied forces to stresses at the location of failures, (these locations are determined based on the DIC footage to check where the actual failure initiated) this results in widely spread stresses at failure. What is especially noticeable is that the coupons with imperfections have higher stresses at failure than those coupons without imperfections. The average failure stress σ_{max} is 651.61 MPa which is approximately 70 MPa higher compared to coupons without imperfections. Besides that also the standard deviation of the coupons is much higher at 45.65 MPa. Expressing this in terms of the coefficient of variation, it results in a CoV of 7.01% compared to the 3.86% for the coupons without imperfections. So the range of failure stresses for coupons with imperfections is doubled. The reason for this is explained in section 4.2.

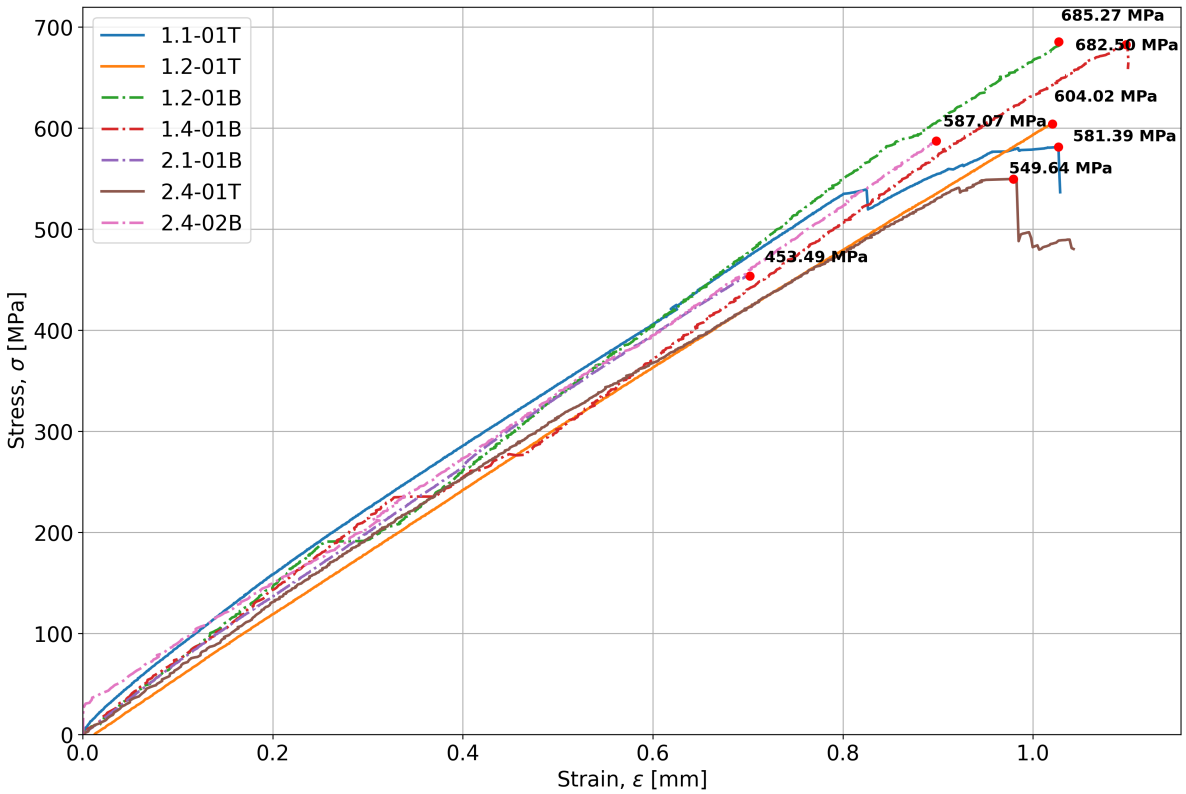

Figure 4.3: Stress - Strain curves from static testing

Figure 4.3 contains the Stress-Strain diagram from all statically tested coupons. The behavior of all tested coupons is very similar, showing a near linear increase of the stresses as the strains increase. All coupons showcase sudden failure behavior except for coupon 1.1_01T, which has a drop in stresses while the strain keeps increasing towards the end. As was already noticed before, the coupons with imperfections reach a higher stress while having the same strain, except for one coupon that has a higher strain and stress. The reason behind this will be further addressed in section 4.2.

4.2. Failure mechanisms

After all the performed static tests, it was clear that the coupons failed, but more interesting to know is how, why and where the coupons all failed. That is why a more detailed analysis was performed on the failure modes of the coupons. This is done based on observations with the DIC system, the data gathered during testing and a visual inspection of the coupons.

Looking at the moment of failure, there is a clear difference in the stresses at failure between the coupons with and without imperfections. The reason behind this is twofold. Firstly, all the coupons with imperfections selected for this test are originating from the bottom flange of the bridge deck profile. As explained in section 3.1.1, the bottom flange contains a lot of imperfections due to the way the GFRP decks were produced. Not only does it contain a lot of imperfections due to the production method, but another side effect is that the overall thickness of the bottom flange was lower compared to the top flange. While the width of each of the coupons is the same due to the cutting, this does not hold for the thickness. This decreases the cross-sectional area of the three coupons from Table 4.3. The difference in the averaged cross-sectional area is given in Table 4.4. This shows that there is a difference of almost 30 mm^2, resulting in an increase in stresses of approximately 13% that was noticed earlier on.

Table 4.4: Cross-sectional areas of static coupons

	Without imperfections	With imperfections
Average area [mm^2]	238.5	209.1

The second reason for the higher failure stresses is that the cross-sectional areas for the calculation are taken at the place of failure. The imperfections mainly consist out of dimples in the coupon. These dimples locally affect the thickness, resulting in lower thicknesses. So in the case where the failure actually occurred in the dimple, the calculated stresses are also higher. This was the case for one of the three coupons, PU 1.2_01B, here the failure initiated at the dimple (Figure 4.5b). The other two coupons' damage initiated at the middle and eventually progressed in the middle.

As for the types of failure that all coupons showed, there were three types, including the failure in the clamp as shown in Figure 4.2. The other two types are shown in the figures below.

Figure 4.4: Matrix cracking and fibre pull-out

The first type of failure that was occurring in almost all coupons is visible in Figure 4.4. This is a combination of matrix cracking with fibre pull-out. The fibres still remain intact, but are pulled out of the matrix, indicating that there is insufficient bonding remaining during due to the tensile load that was applied.

The second type of failure is found for the coupon containing a dimple as imperfection. The failure here occurred precisely at the dimple, this was as expected beforehand. Therefore, the extensometer was placed in this exact region, as shown by the tape location in Figure 4.5.

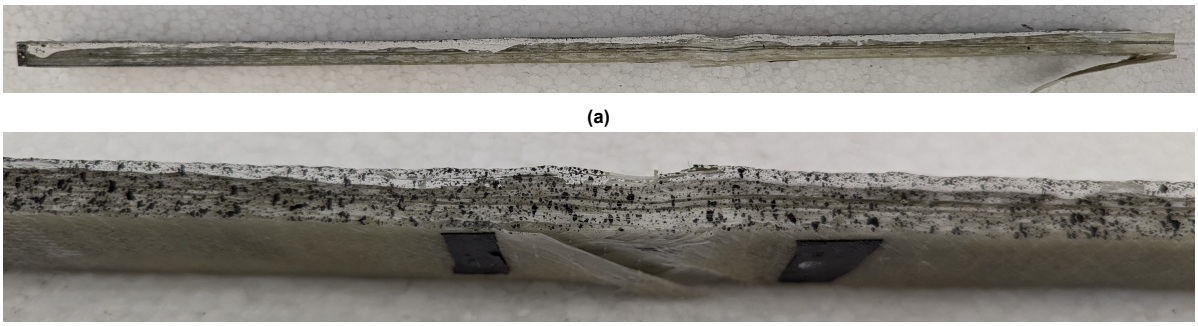

(a)

(b)

Figure 4.5: Delamination and fibre breaking at the imperfection for (a) overview of the coupon and (b) close up of failure

The type of failure is delamination, there is a clear separation between the layers. This occurs due to the increased stresses due to the dimple. In addition to this, there is a combination with fibre breaking and the $\pm 45^\circ$ layer breaking, this is the layer located at the outside, normally wrapped around the foam core.

All pictures of the coupons after the static tests are provided in Annex B.

4.2.1. DIC Findings

Before, the inspections of the damage were mainly visually. To get a more accurate indication how the strains within the coupons are developing, and at which location, the DIC system is used. For the coupons without imperfections, the DIC system was in place for one out of the three coupons.

The only DIC analysis for coupons without imperfections is for coupon PU 2.4_01T. The results are shown in Figure 4.6.

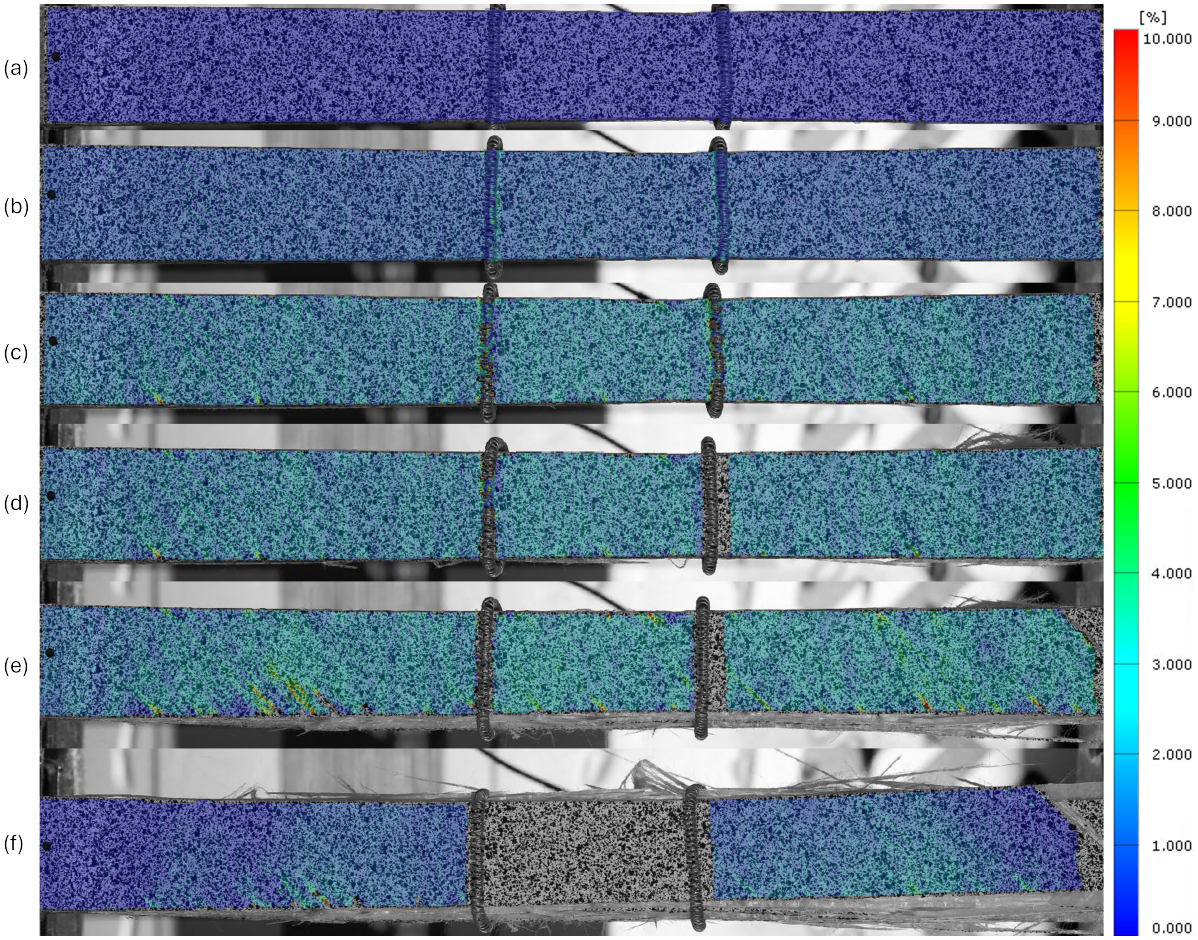

Figure 4.6: PU 2.4_01T strain distribution for (a) Initial stage, (b) 75 kN load, (c) before initial failure at 132 kN, (d) after initial failure, (e) before final failure and (f) final failure at 105 kN

A total of six stages are presented. It starts with the coupon before testing (Figure 4.6a), showing no strains present yet. The second stage (Figure 4.6b) is at a load of 75 kN, approximately halfway of the ultimate limit strength. There appears to be a uniform distribution of the strains along the entire coupon, no particular region exhibits high local strains. Figure 4.6c is just before the first moment of failure occurs, this is at the tensile load of 132 kN. At this stage, the displacement already is 11.5 mm. Figure 4.6d is after the first fibres broke, as can be seen at the sides of the coupons. As a result of the first fibres breaking, the extensometer has shifted. That is why a virtual extensometer is used for the determination of the strains for this coupon. After this failure, the bearing load capacity of the coupon drops to approximately 120 kN, before gradually decreasing further. The final failure as shown in Figure 4.6f occurred at a load of 105 kN with a displacement of 12.3 mm. Fibre pull-out behavior is clearly visible at the sides of the coupon.

For coupons with imperfections, the DIC system was in place for all four coupons, this is including the disregarded coupon PU 2.1_01B due to failure in the clamps. The first coupon is PU 1.2_01B, which is shown in Figure 4.7.

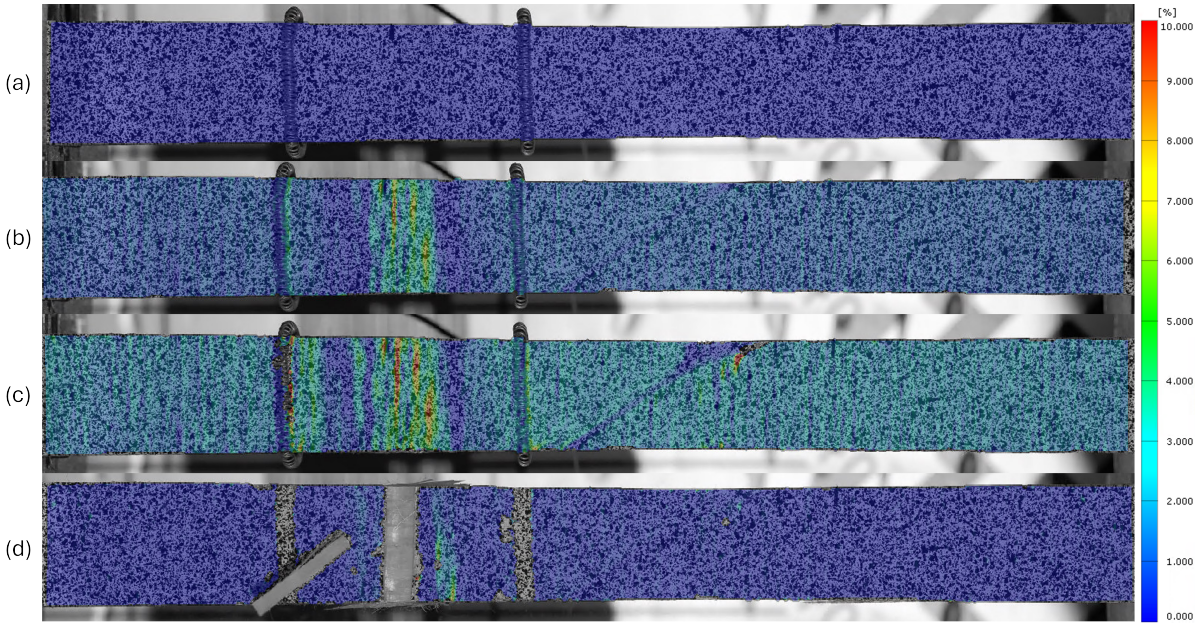

Figure 4.7: PU 1.2_01B strain distribution for (a) Initial stage, (b) 75 kN load, (c) before final failure and (d) final failure at 135 kN

This coupon has four noteworthy stages, starting with the coupon before testing (Figure 4.7a). Again for reference purposes, Figure 4.7b contains the strain distribution at a tensile load of 75 kN. Immediately a big difference is visible compared to the analyzed coupon without an imperfection. Here, a high local strain concentration is visible in the region of the extensometer. This is the region at which the imperfection is located, in this case a dimple. The imperfection has a large influence on the strain distribution of the coupon. Figure 4.7c captures the moment before failure, at 135 kN, this is slightly after reaching the maximum load value of 136.9 kN. The highest strains have increased even further locally near the dimple, with the remainder of the coupon also having increased strains. Figure 4.7d shows the coupon after failure, the outer layer has come off at the location of the dimple, and the extensometer has fallen off as well. Breaking of the fibres is visible as well towards the sides, as is also highlighted in Figure 4.5b.

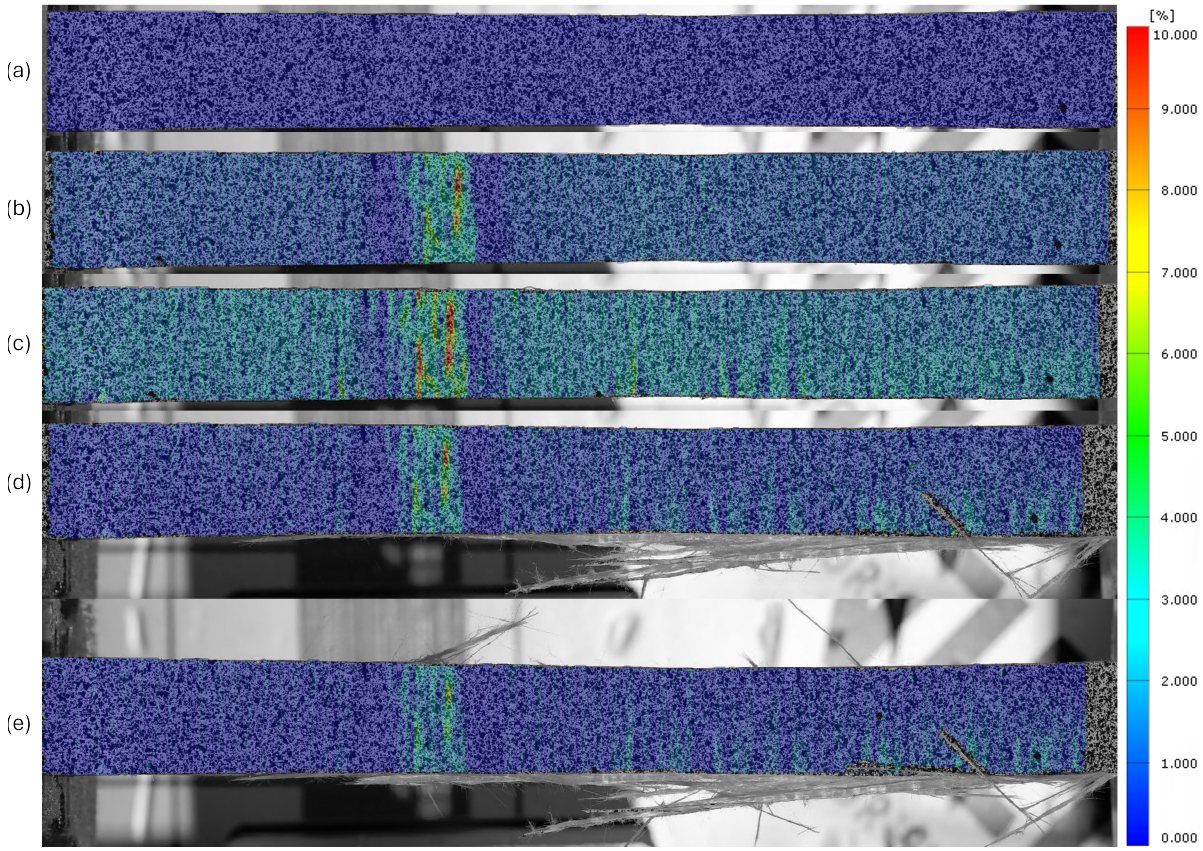

Figure 4.8: PU 1.4_01B strain distribution for (a) Initial stage, (b) 75 kN load, (c) before initial failure, (d) initial failure at 132 kN and (e) final failure at 60 kN

Five stages are shown for the second coupon PU 1.4_01B, containing a dimple as imperfection again. For this test, no extensometer was available due to the gauge arm being bent during the previous static test. As with the previous coupon, again a high local strain concentration is visible in the region of the imperfection, while surrounding the dimple an area containing lower strains. Before the initial failure, the highest strains are near the dimple. Interesting about the analysis is that after the failure at 132 kN, still a bit of load bearing capacity is remaining. The coupon still withstands approximately 60 kN of load, while having relative high strains near the dimples. This is due to the failure not occurring precisely at the location of the dimple, but more towards the middle instead. The final failure is shown in Figure 4.8e, with reduced strains already near the dimple. Also, an increase of fibre breakage is visible.

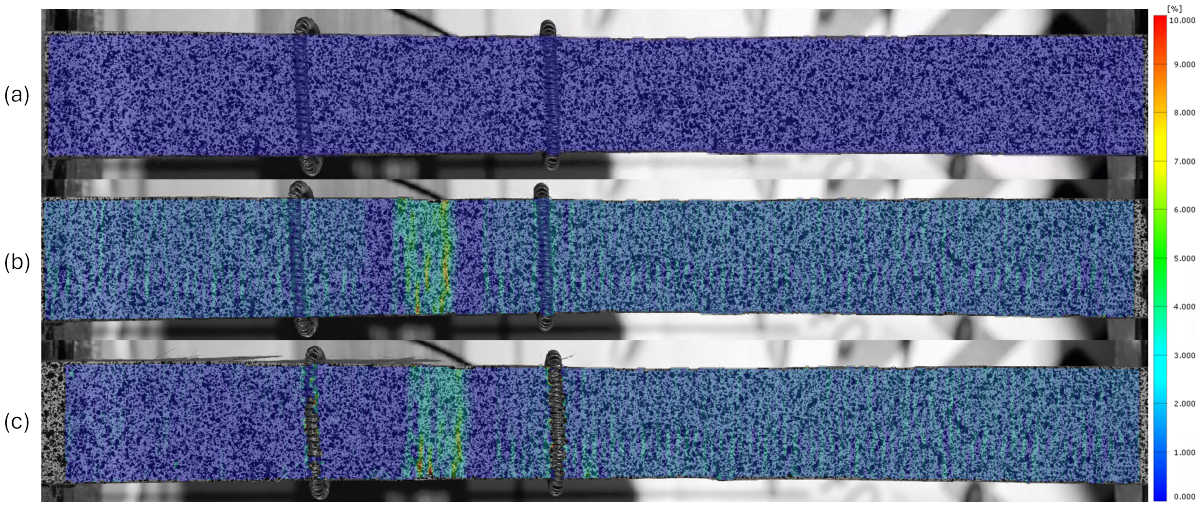

Figure 4.9: PU 2.1_01B strain distribution for (a) Initial stage, (b) 95 kN load and (c) after failure in the clamps at 105

The DIC analysis for coupon PU 2.1_01B is missing a lot of data, due to the storage of the camera being full during the test. That is why instead of 75 kN, the strain distribution at 95 kN is taken. Again, the strains appear to be induced at the location of the imperfection. Unfortunately, this coupon failed in the clamped area, at a load of 105 kN. The moment of failure is shown in Figure 4.9c, but is hardly visible due to failing in the clamps. The exact failure is shown in Figure 4.2. The results from this test were disregarded for the determination of the ULS.

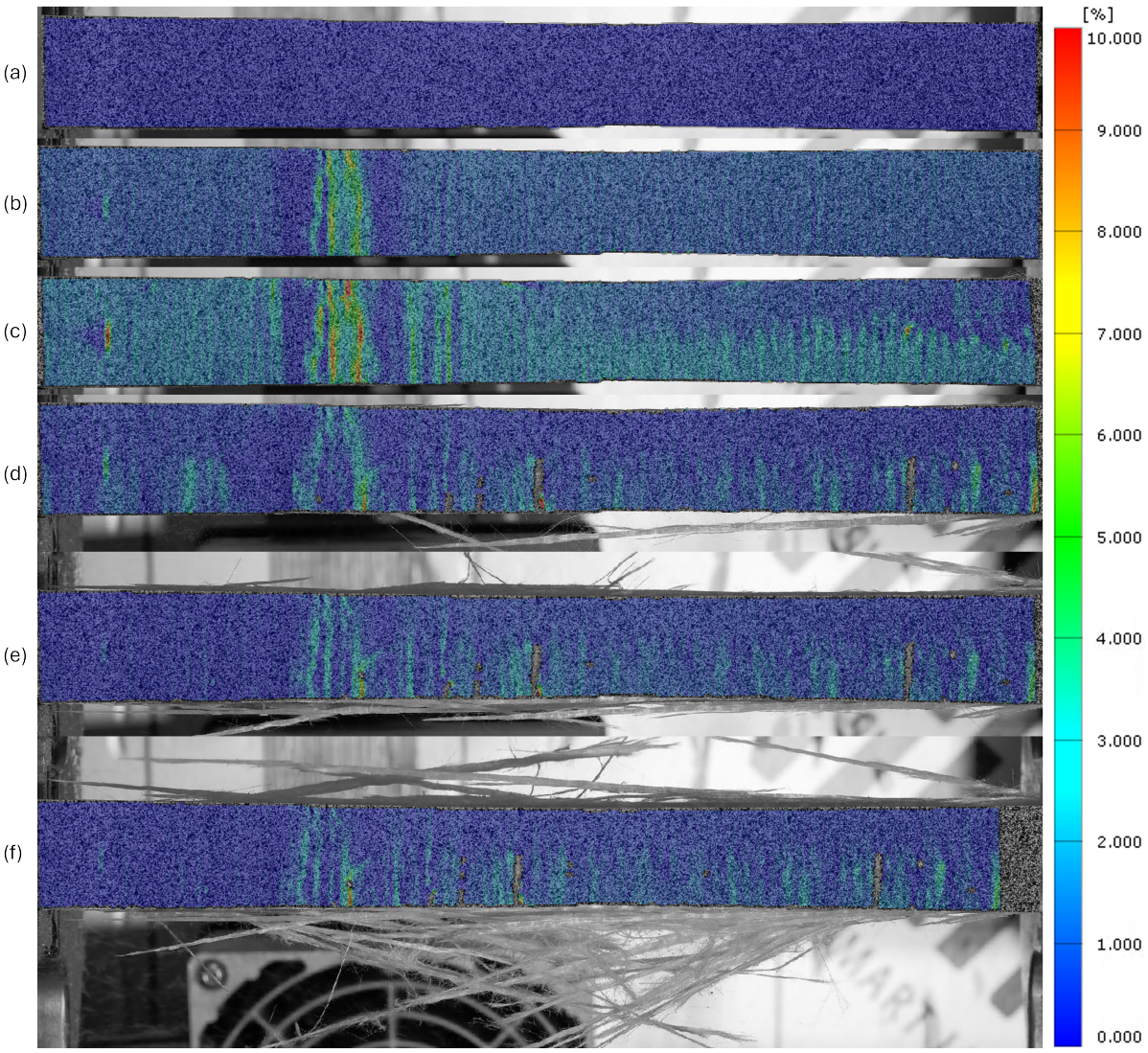

Figure 4.10: PU 2.4_02B strain distribution for (a) Initial stage, (b) 75 kN load, (c) before initial failure at 131 kN, (d) after initial failure, (e) before final failure and (f) final failure at 120 kN

The last coupon that was analyzed with the DIC system is coupon PU 2.4_02B. This coupon again had a dimple as an imperfection. As with all coupons containing a dimple, the highest local strains are located at the dimple. Interesting to see is that right before the initial failure occurs (Figure 4.10c), many higher strains are located at the lower side of the coupon, indicating that the most tension is present there instead of evenly distributed over the entire coupon. Right after the first failure at 131 kN, multiple cracks on the lower side of the coupon have occurred (Figure 4.10d). Due to these cracks, the overall strain near the dimple has significantly reduced as well. As the test progresses, more fibres start to pull out and break. The final failure of the coupon occurs at a tensile load of 120 kN, as shown in Figure 4.10f. Again, the failure is not specifically located at the dimple, indicating that this did not have a large influence on the tensile resistance.

With all the gathered results, the conclusion was drawn that the impact of the imperfections on the tensile resistance is close to negligible. The ultimate tensile resistance of the coupons was set to 135 kN. Based on this conclusion, the next phase of testing could start, which is the dynamic tests for the fatigue resistance of the coupons.

5

Fatigue testing

The static tests were important to perform first in order to gather the data required to determine the parameters of the dynamic tests. All findings for the static tests are bundled in section 4.1. One of the important parameters was the Ultimate Limit State (ULS) for the tensile strength of the coupons. From static tests, the ULS was set to be approximately 135 kN in longitudinal direction of the coupons. The next step in the testing phase was the fatigue tests. These fatigue tests were the main objective of the testing phase to gather insights in the stiffness degradation behavior until failure at different loads levels, which were eventually required for the Finite Element Analysis stage.

5.1. Test Matrix

To perform the fatigue tests, first a plan was set up to get a clear approach for the fatigue tests, which was done in the form of a test matrix. This test matrix is based on the matrix in Table 4.1 and extended with the fatigue tests. The complete test matrix is given in Table 5.1.

Table 5.1: Test matrix for Static & Fatigue tests

Test type	Static (ULS)	Fatigue (FLS)		
Ratio	-	0.1	0.5	
F_{max},kN	135	70% ULS	50% ULS	30% ULS
Frequency, Hz	-	2	4	6
Temperature	Room (23 °C)			
Speciments type	Non-aged and non-postcured			
	Top facing	Bottom facing (with imperfections)		
Number of tests	3 + 3	3-5 specimens per load F_{max}		

The first fatigue tests were performed at 100 kN with a load ratio of 0.1 which is approximately 70% of the ULS, This resulted in failure occurring almost immediately in several plies. Based on this knowledge, it was believed that the initial estimations for the fatigue loads seemed to be too high. With this fatigue load, the coupons would fail before a stiffness degradation curves could be determined. As a result, Table 5.2 contains the updated load levels based on the determined ULS from the static tests.

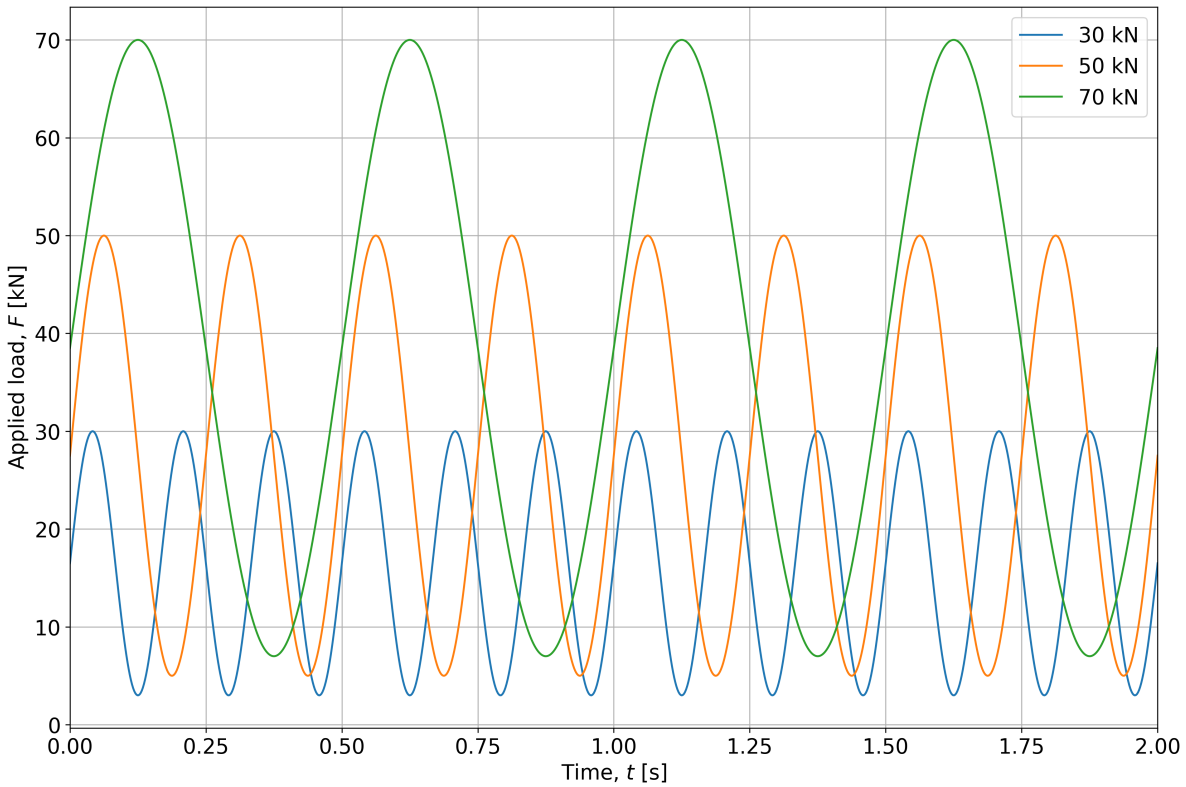

Figure 5.1: Visualization of the three load levels performed during fatigue testing

Table 5.2: Updated test matrix for Static & Fatigue tests

Test type	Static (ULS)	Fatigue (FLS)		
Ratio	-	**0.1**		
F_{max},kN	135	**50%** ULS	**37%** ULS	**22%** ULS
Frequency, Hz	-	2	4	6
Temperature	Room (23 °C)			
Speciments type	Non-aged and non-post cured			
	Top facing	Bottom facing (with imperfections)		
Number of tests	3 + 3	3-5 specimens per load F_{max}		

All limits of the load levels have been altered, the new limits are set based on the forces. The high load is now set to 70 kN which is equal to approximately 50%, the medium load level is set to 50 kN which is equal to 37% and the low load is set to 30 kN which is equal to 22% of the ULS. These loads were all tested and gave better results in terms of noticeable stiffness degradation till failure. Another change in hindsight was to only investigate the load ratio 0.1. This decision was made due to the time and resources it would take to investigate this ratio as well, which would not fit in the time window. A total of 3 successful tests per load level were required to get enough results to draw conclusions. Since chances are that coupons fail in for example the clamped region, the number of tests per load level was set between 3 and 5, resulting in a total amount of successful tests of 18.

With each test having a load ratio of 0.1, there are differences in the stress amplitudes. As a safety measure, different frequencies are chosen per load level. Since the amplitude of the 70 kN load level is so high, a low frequency was chosen to prevent failure of the coupons due to rapid changing stresses, the frequency was set to 2 Hz. This risk is less for the 50 kN load level, so a higher frequency of 4 Hz was chosen, while the 30 kN load level will have a frequency of 6 Hz. A representation of the different load levels and frequencies is given in Figure 5.1.

5.2. Non-uniform thickness

With the updated test matrix in place, fatigue testing could start. However, after performing the first dynamic test immediately a problem arose. As mentioned in section 3.1.1, the panels of the bridge deck are produced with vacuum-infused GFRP panels. One of the drawbacks of this production method was the introduction of imperfections such as local dimples, the effect of imperfections will be discussed further on as well. Imperfections were already considered as part of the scope at the start of the project, but one other problem due to this production method was not taken into account. Another downside of vacuum-infusion is that it also causes thickness differences over larger areas which are not directly noted as local imperfections. This results in coupons having varying thicknesses per side. An example is given in Figure 5.2.

Figure 5.2: Thickness differences of coupons

Figure 5.2 shows a clear contrast between the different coupons in terms of how much they can deviate per coupon. Some thickness differences are almost negligible, while other coupons contain excessive differences, sometimes up to 3 mm. The main reason why this is problematic is because of the way that the coupons are held in the machine. They are held in place by hydraulic wedged clamps that have a flat surface. These clamps are aligned such that they fit perfectly flat on each other when closed. But since the clamps in this case will only clamp a part of the coupon surface instead of the whole surface, this will induce high local stress concentrations at the locations where the clamps are touching the surface. In the static tests that were performed first, this did not cause an issue since the test was static and the coupons could handle this. However, for the dynamic tests it turned out to be a problem. The force generated in the coupons is exerted by cyclic loading at a ratio of 0.1 for thousands of cycles. Tests performed at the high and medium load resulted in almost immediate failure of the coupons in the clamped regions (shown in Figure 5.3). Therefore, a solution had to be found in order to tackle this problem.

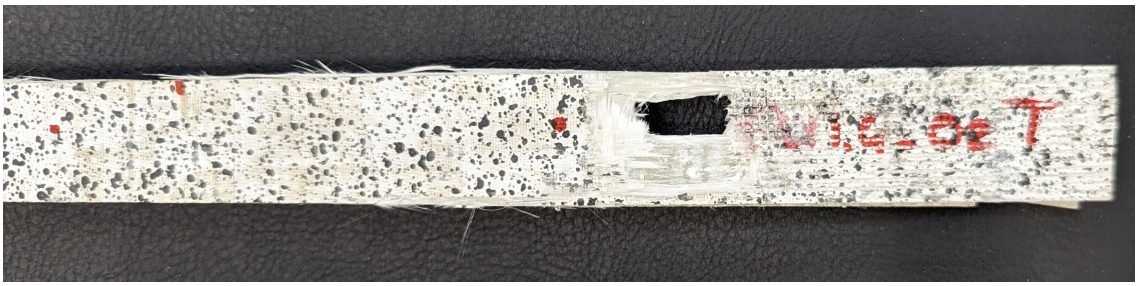

Figure 5.3: Failure in the clamped region

A brainstorm session was initiated, this resulted in several ideas to overcome the non-uniform thickness in the clamped region. One of the ideas that was investigated is the appliance of aluminum tabs at the

ends of the coupons. The main principle is to glue thin aluminum tabs to the GFRP coupons at the ends of the clamped regions. It is important that the tabs are aligned parallel to each other, so there will not be any introduction of high local stresses. This is immediately the biggest challenge that needs to be tackled by ensuring that the tabs are perfectly parallel to each other. The most evident method to achieve this is by applying the adhesive at the coupon and spreading it such that it results in a uniform thickness. This adhesive can either be some kind of resin or glue, as long as its viscosity is low enough such that it can be placed and spread easily. It also needs to be possible to apply a thin layer, because the clamps of the machine have a limit to the thickness they can hold, and in combination with the thickness of the aluminum tabs it easily becomes too thick. A sketch of this idea is shown in Figure 5.4.

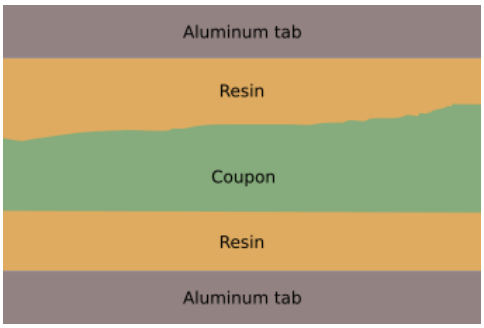

Figure 5.4: Aluminum tabs

After a more in depth look at this solution, several points of attention came up. The main concern was the thickness of the coupon + resin + aluminum tabs. The limit of the clamps was 25 mm, but since the coupons sometimes contain thicknesses up to 12 mm, this only left for 13 mm for the tabs + the adhesive used. Taking into account that the available tabs in the lab had a thickness of 5 mm, this would only leave a small margin for the adhesive. Another concern related to this was regarding the thickness of the layer of the adhesive that sometimes could be very thin, as illustrated in Figure 5.5. In the case where the aluminum tab would be very close to the coupon (5.5a), or when the tab would be in direct contact with the coupon (5.5b), this would still raise problems. If the adhesive layer's thickness non-uniform, this will result in higher stresses towards the thinner side. If the tab is in direct contact with the coupon, this will result in high contact stresses in the coupon instead of evenly distributing the surface stress over the entire width, both of which the goal was to prevent from occurring.

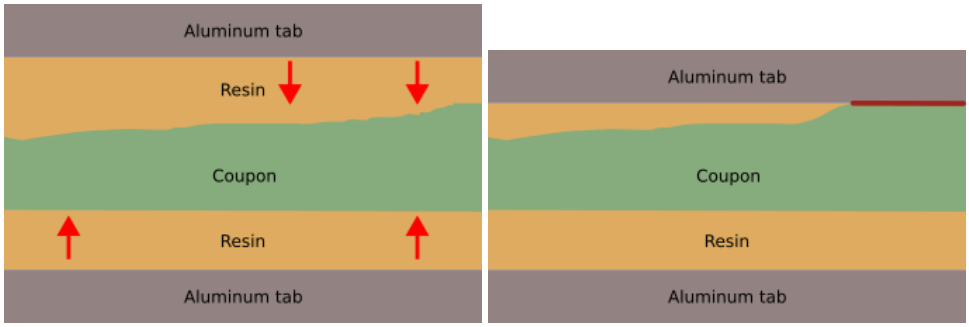

(a) Stress distribution **(b)** High local contact stresses

Figure 5.5: Challenges with aluminum tabs

The last concern with this approach was the challenge of making sure that the tabs will be parallel to each other. If there is a deviation in the alignment of the tabs, the problem will still continue. To make sure the tabs are perfectly aligned, a flat surface or special mold should be created which can align the tabs while the adhesive is poured and cured. This mold also needs to help with the spacing between the coupon and tab such that the resin can be distributed as required. Due to all these challenges, it was decided to investigate another solution instead.

The second idea was to solely use resin around the coupon in the clamped region. For this idea to be implemented, a mold would need to be created in which the coupons could be placed such that the resin could be poured in the desired shape. There were several requirements for the mold in order to get the best specimens possible. To speed up the process of fabricating the resin ends, the mold should be able to hold multiple coupons at once. A total of 3 coupons can be treated at the same time. Another important aspect was that the mold could be reused. It would be very costly if for every batch a new mold needed to be made. To improve reusability, the mold was made with screws instead of glue and nails, so each part could be removed when necessary. Just like with the aluminum tabs alternative, it was crucial that the resin would not be too thick to fit in the clamps, but it should be long enough such that the clamps had sufficient area to clamp. The inner dimensions of the final mold design were set to 100 × 35 × 20 mm. An important requirement was that the inner surface of the mold would be smooth, deviations in this could result in high local stresses as well. In order to get a smooth surface, the choice was made to build a mold from shuttering plywood, also known as betonplex. This is a type of wood with a surface layer of epoxy which is extremely smooth. The advantages of this are the fact that no dirt will stick to it, it does not let liquids through, and will provide the required flat surface for the clamps. The choice was made to pursue this idea, the initial design of the mold is shown in Figure 5.6.

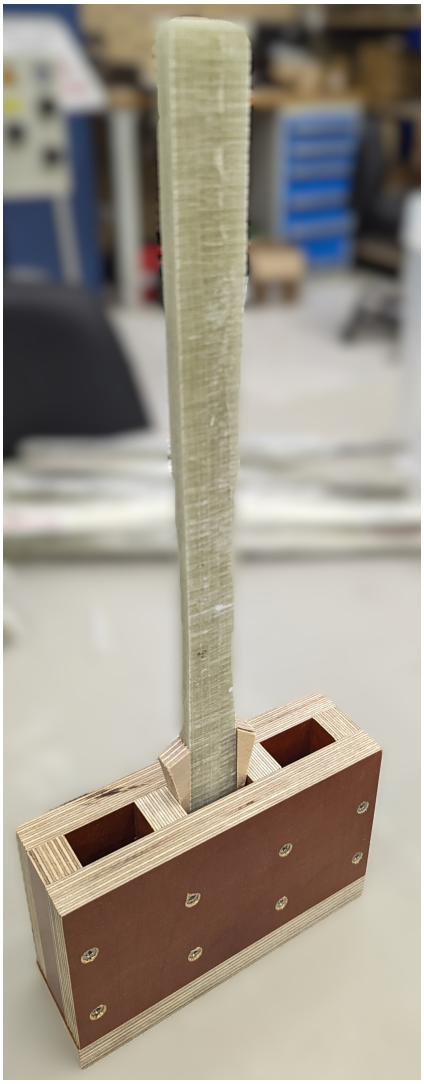

Figure 5.6: First mold design

Due to the way the mold was intended only one side of the coupon could be resin coated at once, this resulted in a new challenge of aligning the coupon such that it would be perfectly parallel with the mold.

The coupon had to be kept vertically in place but due to eccentricities of the coupon and a very liquid resin it would immediately tumble over, so a new system had to be invented to keep the coupons in place. So alterations were made to the initial design, resulting in the final design of the mold which is shown in Figure 5.7. It contains two metal rods at the sides of the mold, which are placed perpendicular in the mold. These rods contain screw thread for nuts, on top of the rods an altered mold will be placed which main purpose is to vertically hold the coupons. With the use of two nuts, the top mold will be pressed against the coupon, creating enough tension to fully clamp the coupon as soon as it's aligned vertically. Inside the top and bottom mold were reference lines present to help align the coupons in place. These were necessary to avoid a twist or misalignment in the coupon between the bottom and top side of the coupon, this would initiate initial bending forces and/or torsion in the coupon as soon as the test would start. This would affect the fatigue life, so needed to be prevented as much as possible.

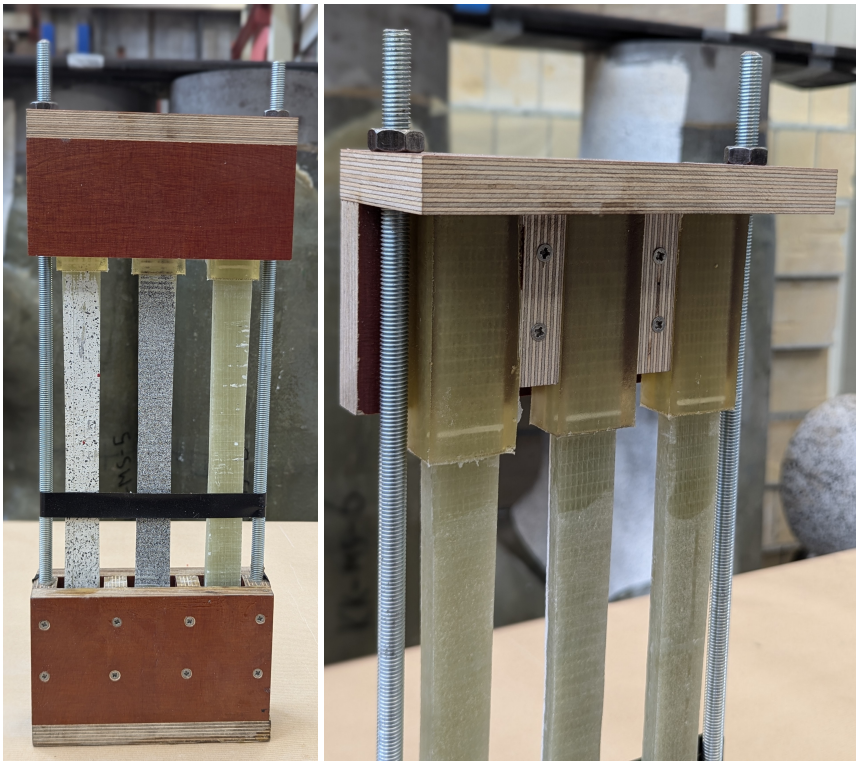

(a) Entire mold design **(b)** Top side final mold

Figure 5.7: Final mold design

5.3. Resin

As explained in section 5.2, the problem with the non-uniform thicknesses was tackled with the help of a plywood mold in combination with a resin. In order for this solution to work, it was crucial that the resin would meet certain requirements and points of attention, these points of attention are listed below:

- The resin has sufficient strength to handle the compressive clamping force from the machine.
- The bonding between the coupon and the resin should be sufficient.
- The resin should not get attached to the mold.
- The resin should have enough time to cure to reach its full strength.
- The resin viscosity should be low.
- It should be easy to purchase the resin.

The clamps in the machine were hydraulic controlled, depending on how much pressure was set. The force had to be high enough such that the coupon would not be able to slip in the clamps. However, a downside of this high clamping force was that the resin should have a high compressive strength, while also having elastic behavior such that the clamps would not break the resin immediately. This type of failure is shown in Figure 5.8. To ensure that the resin would not break when applying pressure during the fatigue tests, first a sample was made which was clamped till failure. Just to be on the safe side, the oil pressure for the remaining tests was set 20% below this maximum pressure.

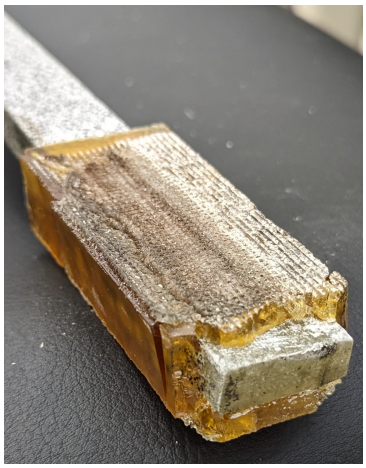

Figure 5.8: Resin compression failure

The next point of attention is regarding the bonding between the coupon and the resin. When there is insufficient bonding between these two, it will result in slip of the coupon in the clamps, which will automatically stop the test. After this slip, the test will not be able to restart on this particular coupon until a new resin is applied, but this needs to be prevented. Figure 5.9 shows the slip failure of the resin surrounding the coupons. In order to prevent slip, a combination of two solutions were applied. As mentioned above, the clamping force was increased until 20% below the capacity of the resin, and the second solution was to perform surface treatment of the coupon. As noted in section 3.4 initially all coupons had received surface treatment with a fine coating of sanding paper, due to this the surface had little texture left. This was beneficial for the DIC pattern and clamped region for static tests without resin ends, but is a disadvantage for the resin bonding. Therefore, sanding paper with a rough texture was used in the area of the resin such that it could better bond to the fibers of the coupon itself.

Figure 5.9: Slip failure resin

Whereas the goal was to get a strong bonding between the resin and the coupon, the complete opposite is the case for the resin against the mold. Since the mold needs to be reusable, it's important that the new coupons can get extracted from the mold without damaging the interior. Therefor, it's crucial to make sure that the resin does not stick to the inside of the mold once fully cured. To guarantee this, a special release agent was applied on the inside of the mold before each new batch, the product is called ACMOS release spray. This could be sprayed on the surface of the mold and once dried up it would ensure that the resin would not attach to the mold's surface.

Resin initially comes in liquid form, but after mixing two or more compounds together a chemical reaction will start resulting in the hardening of the resin. This mixture should have a low viscosity to make sure it's easy to pour it in the mold. Another benefit of having a low viscosity is that it will be able to evenly spread inside the mold on itself, ensuring that there will be no open spaces and such after removing the mold.

A thick substance such as sticky glue would severely limit the workability. Once the resin was evenly spread inside the mold, it was crucial to let the resin cure long enough to ensure that the maximum strength would be reached. If this is not the case, the resin will be soft and jellylike and will immediately deform when applying the cyclic loading for the fatigue tests. The curing time is dependent on the resin properties and environmental conditions such as humidity and temperature, but usually takes several days.

The last and most important point of attention was the availability/purchase ability of the resin. The first batch of coupons was made with a resin made from a mixture of Daron AQR 1025 and Lupranat M20R. This is an extremely strong chemical resin which complied with all points of attention mentioned above. However, after the stock in the lab was used up, it turned out to be extremely difficult to get a new supply due to restrictions to purchase certain chemicals. Therefore, the choice was made to look at alternative resins which would have sufficient strength as well but would be easy to purchase. After thorough investigation, the epoxy resin Poly-Pox THV 500 was found, in combination with hardener 455. This was a fast curing hardener, limiting the curing time to 3 days. An overview of the mechanical properties is given in Table 5.3.

Table 5.3: Material properties Poly-Pox 500 [19]

Property	Value	Unit
Density	1.1	g/cm^3
Viscosity	575	mPa/s
Processing time*	7	minutes
Mixing ratio	100 : 50	epoxy : hardener
Full curing time*	3	days
Flexural strength	79	MPa
Young's Modulus	2830	MPa
Heat Distortion Temperature	42	$^\circ C$
Strain at fracture	7	%
Tension strength	39	MPa

* This is based on a temperature of 20 °C

The final result of the coupon with resin ends is shown in Figure 5.10.

Figure 5.10: Coupons with resin ends

5.4. Results

During the fatigue tests, the focus is on analyzing two phenomenons, stiffness degradation, and the stress life of the coupons. First, the stiffness degradation behavior of the coupons is analyzed. This is the degradation of the material as the amount of cyclic load is increased over time, and will help with insights regarding the stiffness limit per load level. Additionally, the stress life of the coupons is investigated in more depth. This will help to determine the relation between the applied stress and the amount of cycles until failure.

5.4.1. Stiffness degradation

There are multiple aspects contributing to the stiffness degradation. Two aspects that are examined are the influence of the load levels, and the influence of imperfections that were created during production. Both of these distinctions are also indicated in the test matrix in Table 5.2. A total of 21 successful fatigue tests have been performed, varying in the load levels and containing imperfections or not. All stiffness degradation curves are visible in Figure 5.11.

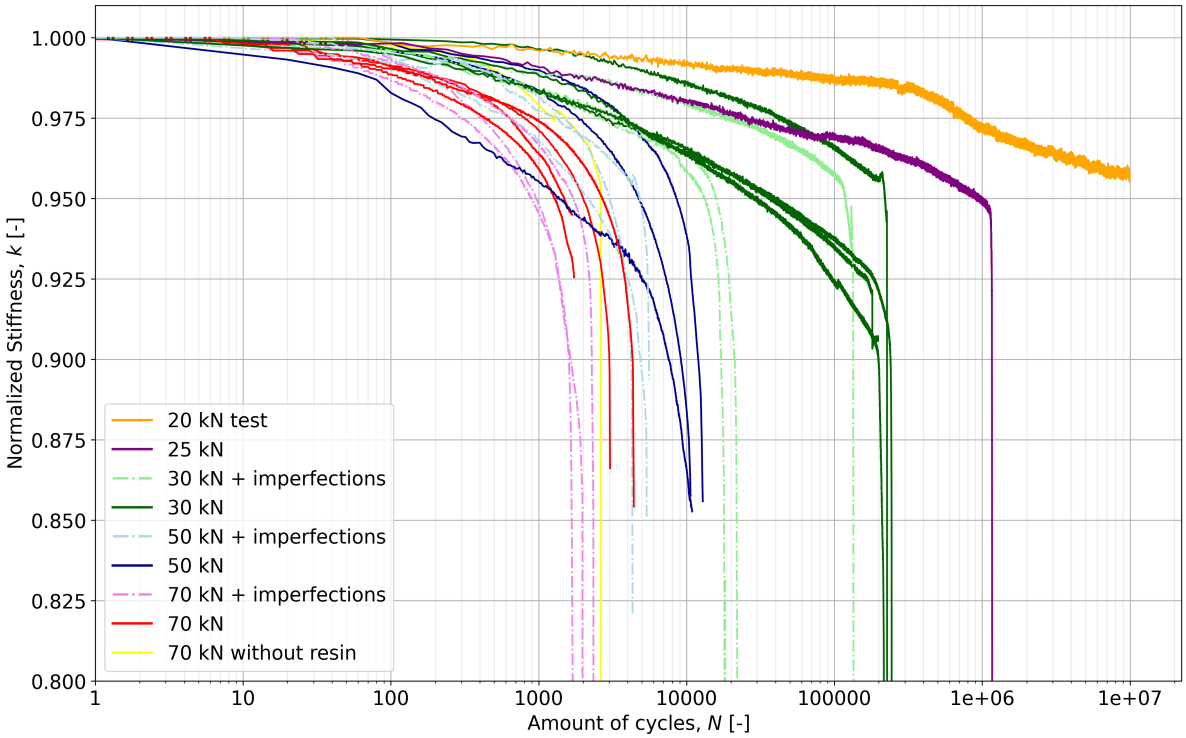

Figure 5.11: Normalized Stiffness degradation curves

The main focus is on three load levels, 30 kN, 50 kN and 70 kN. Two additional tests have been performed, one for 20 kN and one for 25 kN. This was done in order to determine a suitable lowest load level, however, both options were deemed to be too time-consuming to run for multiple coupons. That is why the lowest load level was set to 30 kN. The two extra results will be used for validation purposes later on.

Looking at the influence of the load levels on the fatigue life, a clear distinction can be seen. As one would expect, the lowest fatigue life is examined at the highest load level of 70 kN. The opposite holds for low loads, the lower the load, the longer the fatigue life. Important to note, the 20 kN test coupon actually did not fail. After almost 10,000,000 cycles, the testing machine went into an error and caused the coupon to break in compression. Therefore, the exact amount of cycles until failure for this load level was not determined.

Interesting to learn from all different load levels in one plot, is the fact that the failure limit in terms of stiffness seems to shift depending on the load level. Each average normalized stiffness at failure is listed in Table 5.4.

Table 5.4: Normalized stiffness at failure for each load level

	20 kN	25 kN	30 kN	50 kN	70 kN
Without imperfections	0.956[a]	0.926[b]	0.919	0.882	0.910
With imperfections	N/A	N/A	0.929	0.914	0.898

[a] Coupon did not reach failure
[b] Based on a single test result

First, looking at the coupons without imperfections, there is a clear pattern of the limit decreasing as the force increases. The only deviating load level is 50 kN, that shows a significant drop compared to the other load levels. A possible reason for this can be that micro cracks that occur during longer fatigue tests, play a governing role in the failure of lower loads, while a different failure mechanism might be governing for the high load level. It also partially comes from the fact that it is rather difficult to exactly determine the moment of failure for each coupon. The moment of normalized stiffness failure can be interpreted differently per individual. The implementation of this normalized stiffness failure limit in the user subroutine will be further discussed in section 6.3.2.

As for the average stiffness at failure for coupons with imperfections, it is found that the behavior is different depending on the load level. Both 30 kN and 50 kN fail at a higher stiffness compared to coupons without imperfections. The coupons with imperfections in general have a lower cross-sectional area, resulting in less resistance against deforming. This results in higher deformations locally, inducing more damage internally at the same time. However, the 70 kN load level coupons deteriorate to a slightly lower stiffness before failing. This is most likely related to the very low amount of cycles that has been performed for this load level. Due to this low amount of cycles, even though the damage is increased per cycle, the coupon stiffness is able to degrade more compared to the 70 kN coupons tested without imperfections.

5.4.2. Stress life

When analyzing the fatigue behavior of FRP, besides the stiffness degradation behavior, another behavior is very important to understand how the material behaves. This is the stress-life performance, expressed in S-N curves. S-N curves graphically show the stress (S) against the number of cycles until failure (N). By combining the measurements from all tests, a rough estimation of the lifespan in terms of cycles for each stress level can be expressed by a fitting line.

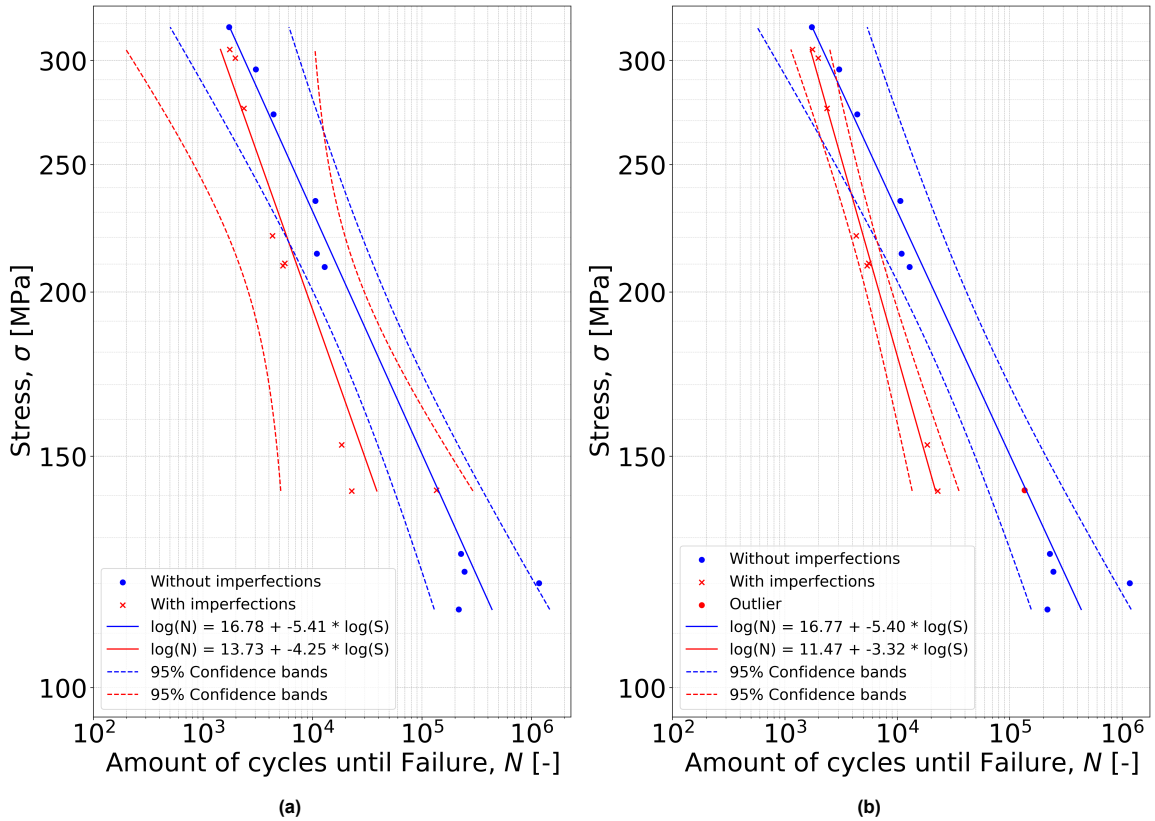

Figure 5.12: S-N curves using experimental data for samples with and without imperfections where a) all original data points presented and b) one imperfection outlier considered as without imperfection

Figure 5.12a shows two S-N curves for the tested coupons, one for coupons with imperfections and one without imperfections. The result of the 20 kN coupon is excluded from this graph since it did not actually fail. In addition to the S-N curves, the 95% confidence bands are also included. Confidence bands take into account the uncertainty that can occur when performing new tests. Based on the data gathered, it is calculated that the new test results are likely to be within this range between the bands, with a certainty of approximately 95%.

Looking at the S-N curves of both types of coupons in Figure 5.12a, a distinction can be observed in the angle of the slope. Both equations for the fitting lines are given in the form of $Log(N) = A + B \cdot Log(S)$, where A relates to the actual fatigue life and B indicates the slope of the line. A higher value of A relates to a better fatigue life in general for all stress levels, so is desirable. From experimental testing, it was found that coupons without imperfections have a higher fatigue life. This same behavior is found by comparing the values of A for coupons with and without imperfections. The value of A for coupons without imperfections is higher than with imperfections. Besides the differences in the fatigue life, there is also a difference in the slope B. A higher slope indicates a higher sensitivity to changing stresses on the overall fatigue life. This implies that the coupons without imperfections actually are more sensitive to changes in the stress.

For the coupons with imperfections, it was found that it is less sensitive to changes in stresses. This comes with both advantages and disadvantages. An advantage is that the coupons perform more stable across varying stress levels. An increase in stresses results in a relatively lower decrease of the fatigue life compared to coupons without imperfections. This is in line with the results found when analyzing the stiffness degradation curves. The disadvantage is that in general it means shorter fatigue life at lower stress levels. The most notable result from the tested coupons with imperfections is the excellent performance of the single coupon at approximately 140 MPa and 135,000 cycles. As will be further explained in section 5.5.1, this is due to the difference in type of imperfection. The two other tests performed at the same load level had large dimples as imperfections, whereas this outperforming coupon only had a small bend as an imperfection. This outlier is within the confidence bands of the coupons without imperfections and fits perfectly in the estimated fitting line for coupons without imperfections. Therefore, the choice was made to assume this result as such.

When excluding this outlier from imperfections, and instead consider it as a coupon without imperfection, a more representative S-N curve and confidence band for both coupons is found. This is shown in Figure 5.12b. The largest impact is on the estimated fatigue life for coupons with imperfections. The fitting line now indicates a steeper slope, implying two things. First, the sensitivity to stresses has reduced, which can be considered beneficial. Secondly, it implies that the estimated performance on lower stress levels is lower. This is logical since the extremely well performing coupon “with imperfections” significantly increased the average performance at the lowest load level. By excluding the outlier for the lowest load, the standard deviation is also significantly reduced, which impacts the 95% confidence bands region. Figure 5.12b provides narrower confidence bands, indicating more confidence in the results from experiments, and less variability in future test results.

One noteworthy data point regarding coupons without imperfections is the result of the 25 kN test, which ran for approximately 1,100,000 cycles and had a cross-sectional stress of approximately 120 MPa. In terms of stresses, this is very similar to the three data points left from this, indicating the 30 kN tests. These tests had an averaged stress of 121 MPa. However, these fail at approximately 220,000 cycles already, a factor five prior to the 25 kN test. This is partly due to the large difference in cross-sectional area from the coupons. The 30 kN coupons had an average cross-sectional area of 247.91 mm^2, while the 25 kN coupon had an area of 208 mm^2. This means that the fibre volume fraction was much higher for the 25 kN coupon. From this single test, it seems that this is very beneficial for the fatigue resistance of the coupon.

5.5. Failure mechanism

All tests were force controlled, with a failsafe for when the resistance of the coupon dropped. However, an additional failsafe was enabled. Tests were automatically stopped when a large displacement was observed by the machine, this mainly is due to the coupon breaking in half. In addition, a visual inspection of the failed coupons is also performed, this helps with analyzing where the coupon failed and also helps with predicting why the failure occurred. Different types of failure mechanisms that have been found in the coupons will be highlighted in this chapter. Important to note is that often not one of the failure mechanisms is occurring, but a combination.

The first failure addressed is matrix cracking, as shown in Figure 5.13. Matrix cracking is one of the most common failure mechanisms during fatigue testing of FRP composites. Due to the cyclic loading, over time the bond between the fibres and matrix starts to weaken. Initially this starts in one layer, but as this weakening progresses, it can transfer to adjacent plies by the creating of micro cracks. As these small cracks start to accumulate, voids start to occur underneath the surface. These small voids turn into lighter areas, as is visible on the top side of the coupon in Figure 5.13.

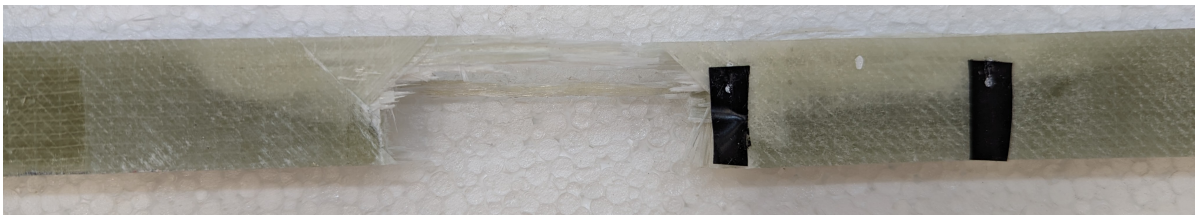

Figure 5.13: Matrix cracks

Closely related to the matrix cracks is the failure mechanisms called delamination. As the micro crack damage progresses in the matrix, eventually this leads to delamination. Delamination is when separation between the plies on a larger scale occurs. One of the disadvantages of delamination is that the layers will start to act independently and not as one part of the entire laminate, resulting in lower strength. Eventually this delamination will lead to failures as shown in Figure 5.14.

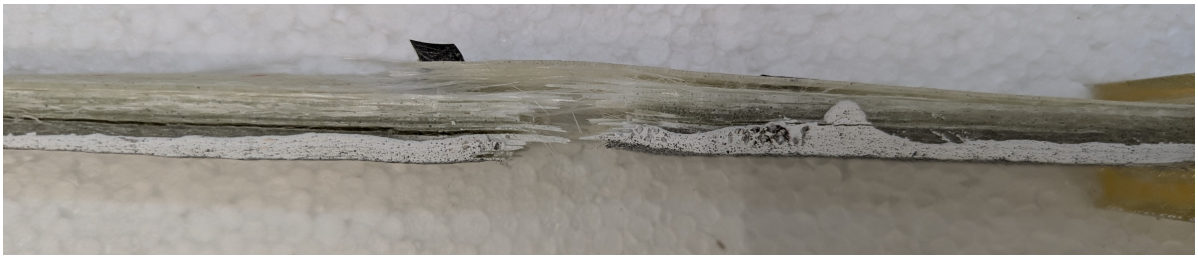

(a)

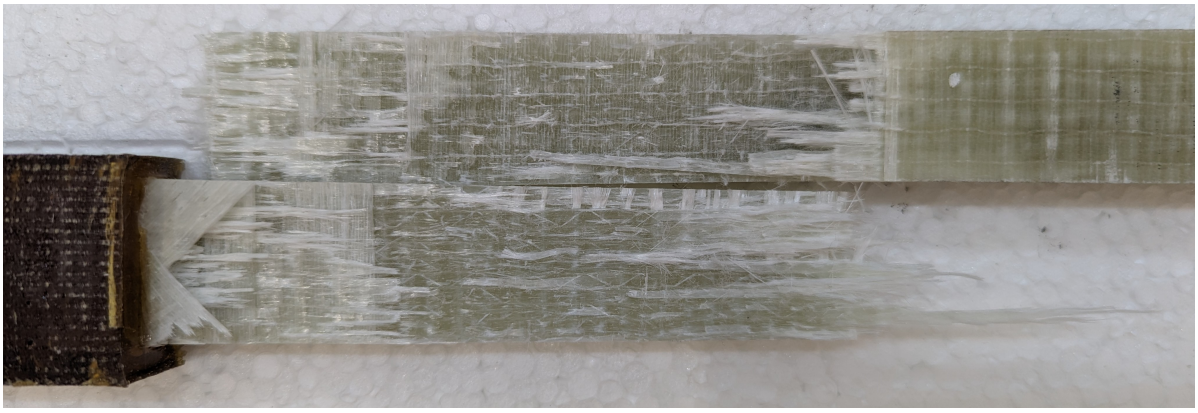

(b)

Figure 5.14: Delamination

In Figure 5.14a you can clearly see the delamination occurring between the layers as a large gap is visible. As mentioned previously, often different kind of failure mechanisms occur at the same time. In Figure 5.14b a completely split coupon is visible due to both delamination and fibre breaking. By looking closely, it is visible that the delamination occurred in multiple layers, since several layers are visible with fibres in all three directions.

In general, the last stage before failure is the fibre breakage. A composite is a combination of a matrix resin and fibres, often orientated in multiple directions. When matrix cracks/delamination occurs, the main load bearing function of the matrix is gone. This leaves only the fibres to take all the remaining load. Usually, not all fibres break at once, but often start at imperfections and/or locations of high local stress concentrations. Fibres from glass are often quite brittle, resulting in sudden failure of the fibres. Once one layer of fibres breaks, this additional load needs to be redistributed to other layers, speeding up this process of fibre breakage as well. Clear examples of fibre breakage are shown in Figures 5.14b and 5.15.

Figure 5.15: Fibre breakage

The coupons tested mostly existed out of UD plies, with only several plies orientated perpendicular and one outer layer of $\pm 45^{\circ}$. One consistent failure was the breaking of this outer ply, which in both static and fatigue tests often was the first ply to fail. This resulted in the clear 45° cut, as shown in Figure 5.16.

Figure 5.16: Failure of $\pm 45^{\circ}$ ply

5.5.1. Impact of imperfections

Earlier, the comparisons between coupons with and without imperfections was done on a more general level. In this section, a more detailed comparison is performed to analyze the differences between coupons with and without imperfections on an individual load level.

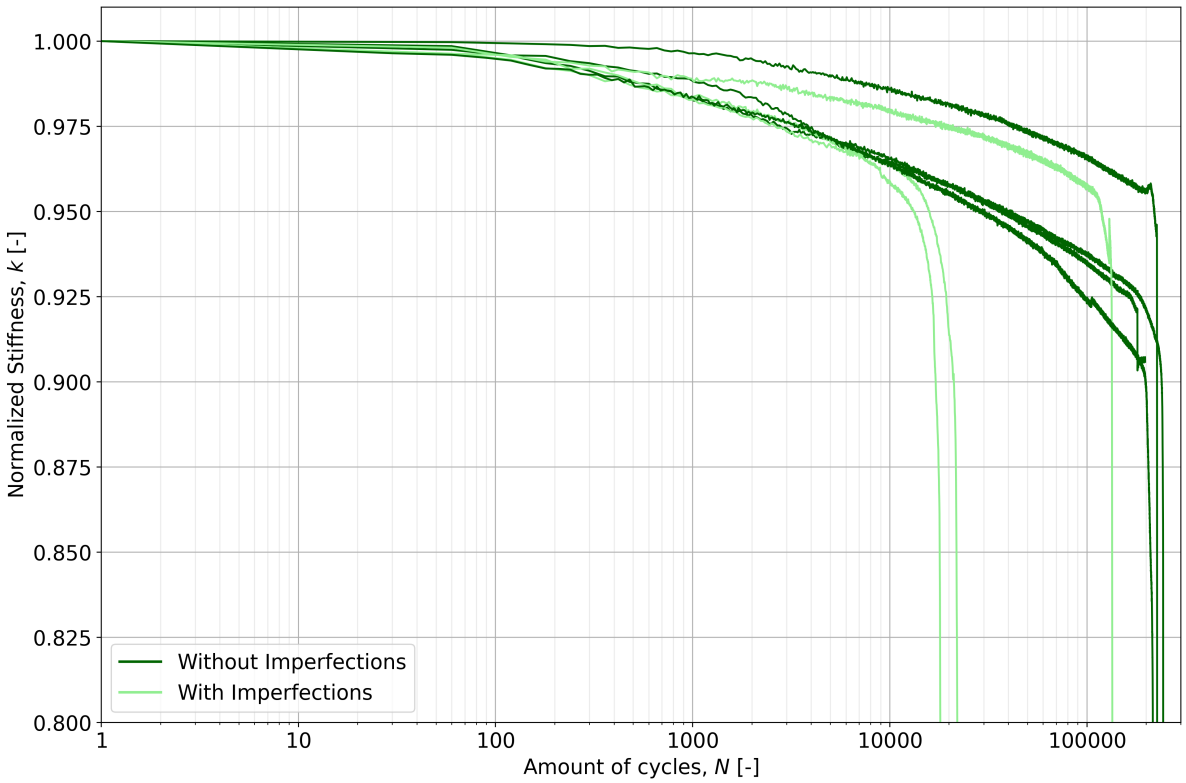

Figure 5.17: Stiffness degradation curves for load level 30 kN

Figure 5.17 shows the stiffness degradation over the fatigue life for the coupons tested on load level 30 kN (22% ULS). Both slopes are relatively similar. Looking at the differences between coupons with and without imperfections, the largest difference is observed in terms of amount of cycles until failure. The stiffness drop starts to deviate about ten times quicker. More data relating to the tests is provided in Table 5.5.

Table 5.5: Fatigue test, Low load

30 kN	Coupon	Normalized Stiffness at failure	Cycles till failure, N [cycles]	Cross-sectional Area, A [mm^2]	Stress at location of failure, σ [MPa]
Non-imperfections	1.1_02B*	0.920	197,760	222.31	179.93
	2.1_03T	0.910	244,268	244.81	122.54
	2.2_02T	0.905	216,878	261.58	114.69
	2.2_04B	0.941	227,547	237.33	126.41
	Average	0.919	229,564	247.91	121.21
	StDv, σ	0.016	11,272	10.140	4.88
	CoV, %	1.7	4.9	4.1	4.0
Imperfections	1.4_04B	0.929	22,871	212.55	141.14
	2.1_02B	0.908	18,498	196.08	153.00
	2.1_03B	0.951	135,600	212.25	141.34
	Average	0.929	58,990	206.96	145.16
	StDv, σ	0.017	54,201	7.694	5.544
	CoV, %	1.8	91.9	3.7	3.8

* Stopped due to slip, not taken into account for data below

The most astonishing finding is the result from coupon 2.1_03B, which has a fatigue life of approximately 6 times above average for the other coupons containing imperfections. After a geometrical comparison of the coupons, it soon was discovered that this coupon contains a different kind of imperfection. Whereas coupons 1.4_04B and 2.1_02B both had a dimple as an imperfection, coupon

2.1_03B only had a slight bend due to the Z-shape lay-up. Based on the fatigue life results, it can be inferred that this type of imperfection only has a relative low influence on the fatigue life, as it reduces by a factor of 2 instead of 11.1. Taking into account the S-N curve results from Figure 5.12b, one can argue that it can be considered as a coupon without imperfection.

In this case, the coupon is still taken into account for the determination of the average and standard deviation, this results in slightly biased results. Another interesting finding is the stress at the location of failure. On average, this is 25 MPa higher. This is due to the lower cross-sectional area for coupons with imperfections, caused by the dimples. This higher stress is another reason for the reduced fatigue life performance of coupons with imperfections.

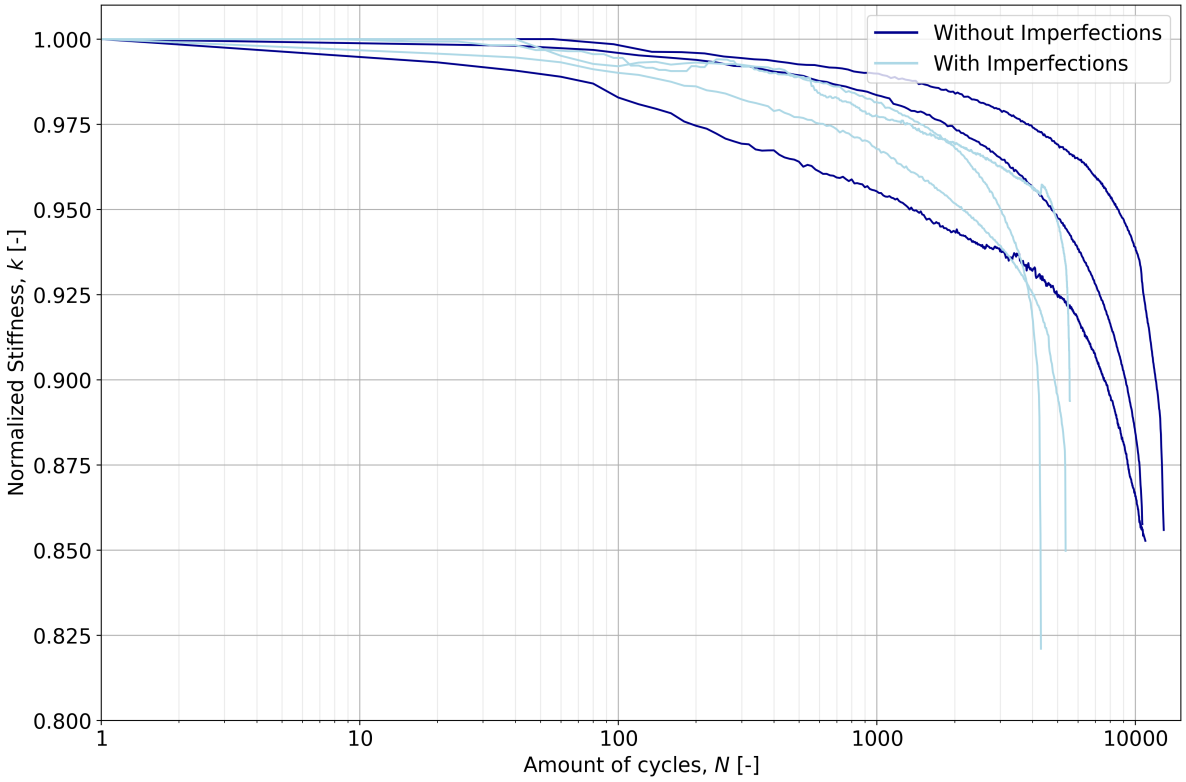

Figure 5.18: Stiffness degradation curves for load level 50 kN

As for the coupons tested on the 50 kN load level (37% ULS), again the stiffness degradation slopes are very similar. The only outlier is coupon 2.3_02B, which has a steeper stiffness degradation starting at approximately 100 cycles. No clear reason for this is found, as the coupon showed no signs of imperfections and geometrically wise is relatively in line with the other tested coupons. One possible reason could be that the coupon did not fail in the region of the extensometer, but below that instead. This could have resulted in deviating measurements for the stiffness.

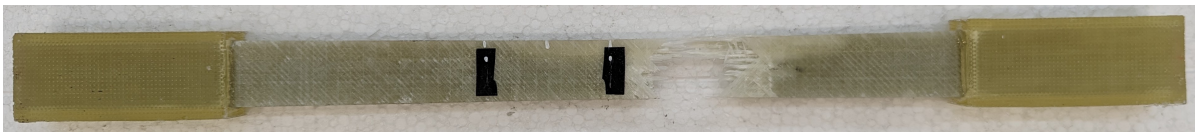

Figure 5.19: Failure coupon 2.3_02B, outside the limits of the extensometer

The extensometer was placed between the two strips of tape as shown in Figure 5.19. The fatigue life performance of this particular coupon is also near average, indicating imperfections did not play a significant role in this stiffness drop as well.

Table 5.6: Fatigue test, Medium load

50 kN	Coupon	Normalized Stiffness at failure	Cycles till failure, N [cycles]	Cross-sectional Area, A [mm^2]	Stress at location of failure, σ [MPa]
Non-imperfections	1.3_04B	0.875	10,651	213.13	234.60
	2.3_01T	0.910	12,885	239.26	208.97
	2.3_02B	0.860	10,939	233.80	213.86
	Average	0.882	11,492	228.73	219.14
	StDv, σ	0.021	992.2	11.254	11.11
	CoV, %	2.4	8.6	4.9	5.1
Imperfections	1.3_01T	0.915	5,377	238.80	209.38
	2.3_01B	0.931	5,583	237.78	210.28
	2.3_04B	0.897	4,316	226.61	220.65
	Average	0.914	5,092	234.4	213.4
	StDv, σ	0.014	555.12	5.52	5.1
	CoV, %	1.5	10.9	2.4	2.4

The influence of imperfections on the medium load is much lower compared to the low load level. On average, the fatigue life is reduced by a factor of 2.3, whereas this factor was approximately 11.1 for low loads. As for the type of imperfections, there again are two kinds of imperfections present. Coupon 1.3_01T has a small thickness increase, whereas the two other coupons both contain dimples. Despite the different imperfections, the fatigue life is relatively equal, with only coupon 2.3_04B performing slightly worse. This is due to the fact that this imperfection is larger compared to the other two coupons (Figure 5.20).In terms of the cross-sectional areas and therefore also the stresses working at the locations of failure, all coupons are nearly identical.

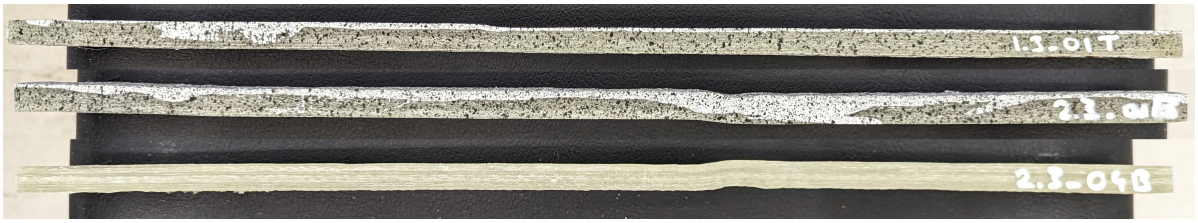

Figure 5.20: Coupons with imperfections tested for 50 kN

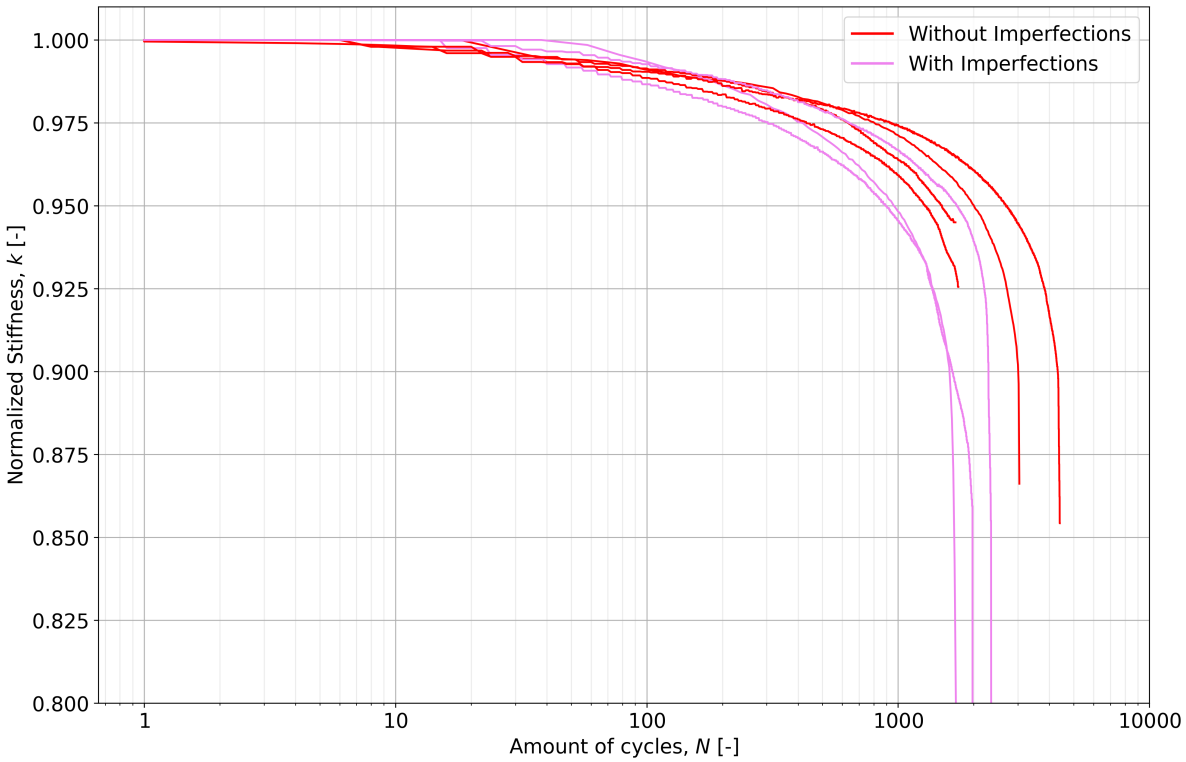

Figure 5.21: Stiffness degradation curves for load level 70 kN

The highest load level consists of cyclic loading with a maximum force of 70 kN (50% ULS). Again, the stiffness degradation slope is very similar for all coupons, as is the stiffness at failure (Figure 5.21). Looking at the amount of cycles until failure, the biggest surprise is coupon 1.3_03T, which fails earlier than all three coupons containing imperfections.

Table 5.7: Fatigue test, High load

70 kN	Coupon	Normalized Stiffness at failure	Cycles till failure, N [cycles]	Cross-sectional Area, A [mm^2]	Stress at location of failure, σ [MPa]
Non-imperfections	1.3_03T	0.925	1,737	220.12	318.01
	1.4_03B	0.900	4,314	256.40	273.02
	2.2_03B	0.904	2,979	236.99	295.37
	2.4_03T*	0.944	1,692	212.15	329.96
	Average	0.910	3,010	237.84	295.47
	StDv, σ	0.011	1052	14.82	18.37
	CoV, %	1.2	35.0	6.2	6.2
Imperfections	1.3_04T	0.900	1,758	228.89	305.82
	2.1_04T	0.915	2,369	253.78	275.83
	2.4_03B	0.878	1,977	232.39	301.21
	Average	0.898	2,035	238.35	294.28
	StDv, σ	0.015	252.75	11.0	13.19
	CoV, %	1.7	12.4	4.6	4.5

* Stopped due to slip, not taken into account for data below

This low fatigue life of coupon 1.3_03T can partly be traced back to the low cross-sectional area. This is the lowest area of all coupons tested, even the coupons with imperfections have a higher cross-sectional area. Due to this, the local stresses due to the 70 kN load are much higher compared to the other coupons, resulting in the early failure as is. By comparing the other coupons, it is noticeable that the influence of the imperfections on the fatigue life again has slightly reduced compared to the medium load level. Instead of a factor two difference, it is now in the region of a factor of 1.5. The types

of imperfections are a mixture between a slight bend and dimple, however, this has an insignificant influence on the fatigue life. Based on this, it can be concluded that as the force increases, the impact of imperfections on the fatigue life drops.

To summarize the influence of imperfections on the fatigue life, a comparison is given in Table 5.8.

Table 5.8: Influence of imperfections on fatigue life

	30 kN	50 kN	70 kN
Without imperfections [cycles]	229,564	11,492	3,010
With imperfections [cycles]	20,685	5,092	2,035
Reduced by factor	11.1	2.3	1.5

Location of failure

One of the interesting findings of the fatigue tests was the relation between the location of failure and the presence of imperfections. Figure 5.22 shows the locations of failure for all coupons without imperfections. All three coupons from the same load level are bundled together.

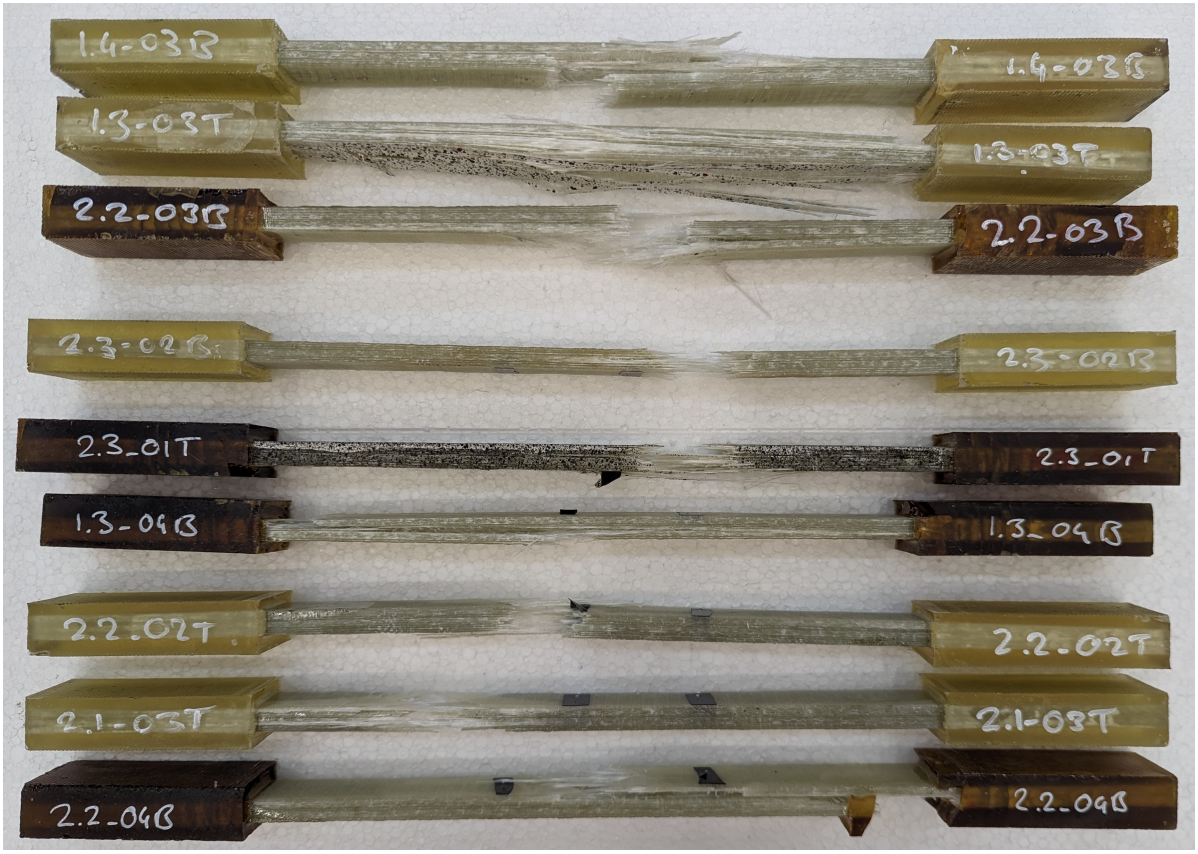

Figure 5.22: Coupons without imperfections after failure

Most of the coupons without imperfections have the failure in the middle region, as one would expect based on the chosen geometry in section 3.2. The locations of failure for coupons with imperfections is shown in Figure 5.23. When looking at the locations of failure for coupons that contain imperfections, it is noticeable that all coupons containing imperfections actually did fail at or nearby the imperfection.

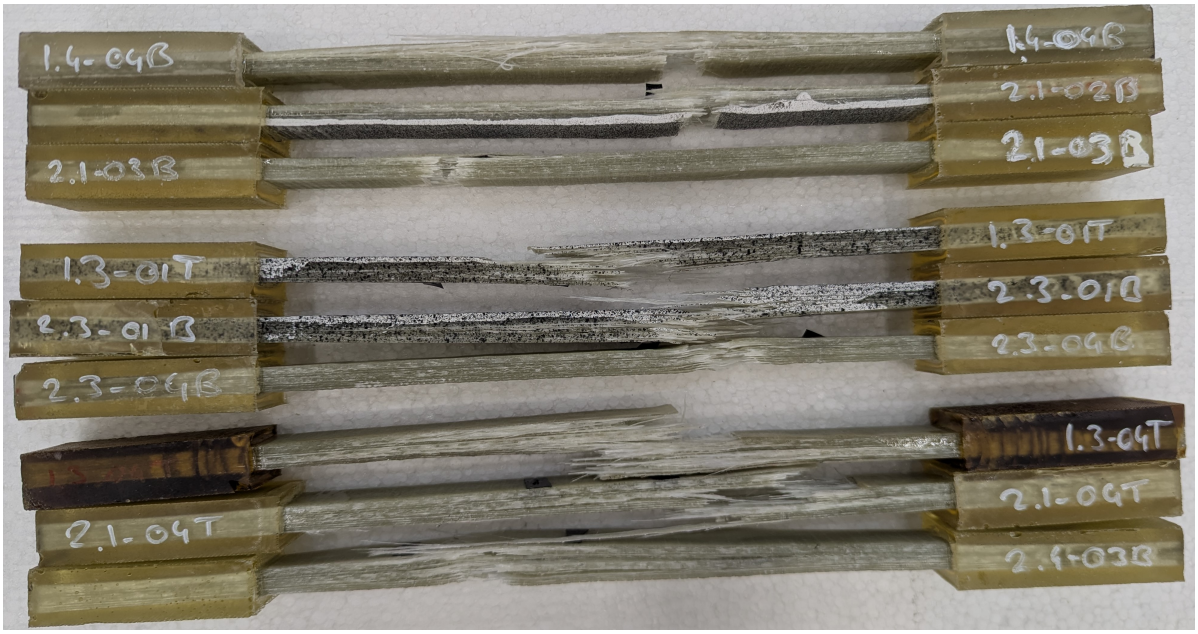

Figure 5.23: Coupons with imperfections after failure

6

Finite Element Analysis

In order to conduct a Finite Element Analysis (FEA) a numerical model is created. This model is made in Abaqus/CAE 2022, which is a powerful tool for pre- and post-processing for different types of geometries and materials on a material level. This chapter provides a detailed description of the model itself and the fatigue analysis performed.

The model itself consists out of solid, homogeneous elements called C3D8R. These are eight-noded linear hexahedral solid elements, commonly used because they provide a good balance between accuracy and computational time. The geometry of the model is based on the dimensions given in section 3.2. Since the coupons are small objects, a small mesh size of approximately 4 mm is chosen, consisting out of brick shaped meshing. Defining the material properties can be done via several methods. Since we are dealing with a composite consisting out of 32 layers in different directions, the properties of the material are non-isotropic. Two common methods to define the material properties are either by:

- Model the coupon per layer with the material properties of the fiber glass. By modelling each layer and assigning the correct orientation to the layers, you end up with a model representing the correct coupon properties. With this method, you can evaluate the stresses per ply level.
- Model the coupon with solid elements which are assigned by the homogenized material properties, determined by using the Classical Laminate Theory (CLT).

The second option, basing it on solid elements with homogenized material properties, is used here. The new material properties with the CLT are determined below. This method was chosen since with this model for now we are mostly looking at the fatigue life performance of the entire coupon and not at the occurring failure of individual plies.

For determining the homogenized material properties of the coupon, the entire lay-up of the facings are inserted in the CLT-tool [21], created by the TU Delft. This results in the ABD-matrix, which are used for determining the stiffness and strength of the material. The only matrix that is used here is the A-matrix, which is given in Table 6.1.

Table 6.1: A-Matrix facings

A-matrix		
331043.15	41493.75	0.00
41493.75	225255.70	0.00
0.00	0.00	43275.51

With the help of a set of equations, this can be transformed to the required material properties.

$$E_1 = \frac{1}{t} \cdot \left(A_{11} - \frac{A_{12}^2}{A_{22}} \right) = \frac{1}{10} \cdot \left(331043 - \frac{41494^2}{225256} \right) = 32340 \text{MPa} \tag{6.1}$$

$$E_2 = \frac{1}{t} \cdot \left(A_{22} - \frac{A_{12}^2}{A_{11}} \right) = \frac{1}{10} \cdot \left(225256 - \frac{41494^2}{331043} \right) = 22005\text{MPa} \tag{6.2}$$

$$G_{12} = \frac{1}{t} \cdot A_{66} = \frac{1}{10} \cdot 43276 = 4328\text{MPa} \tag{6.3}$$

$$\nu_{12} = \frac{A_{12}}{A_{22}} = \frac{41494}{225256} = 0.184 \tag{6.4}$$

$$\nu_{21} = \frac{A_{12}}{A_{11}} = \frac{41494}{331043} = 0.125 \tag{6.5}$$

In addition to these elastic material properties, the user defined field properties option is turned on. Allowing the material properties to be changed by the subroutine. If the failure threshold is reached, all material properties of the specific element will be reduced to 0 instead, simulating the element deletion.

6.1. Boundary conditions

After analyzing all dimensions of the coupons used for fatigue testing, it was found that in general, the cross-sectional area of the 30 kN tested coupons is larger. That is why two models are created. They are identical in all ways except for the thickness. The coupons are build up as a solid extrusion with a thickness of 9.64 mm for the coupon tested on 30 kN load level and a thickness of 9.2 mm for the load levels of 50 kN and 70 kN. On both sides it has a partition destined as the surface which will be clamped in the machine during testing. To simulate this in the model, boundary conditions will be applied to these partitions, shown in Figure 6.1a.

Once the coupon is fully clamped in the machine, displacement, and rotation is restricted in all directions except for the y-direction. The machine performs cyclic loading by moving one of the two sides in longitudinal direction. This process is being simulated by fully constraining displacement and rotation in the bottom partition and allowing the top partition to move in longitudinal direction. How far this displacement is, is based on the applied load and the strain that is related to this.

To achieve these constraints in the model, the clamped surface area is kinematically coupled to Reference Points located on the ends of the coupon (Figure 6.1b & 6.1c). This surface is completely constrained in all degrees of freedom, leaving only one reference point able to move in Y-direction.

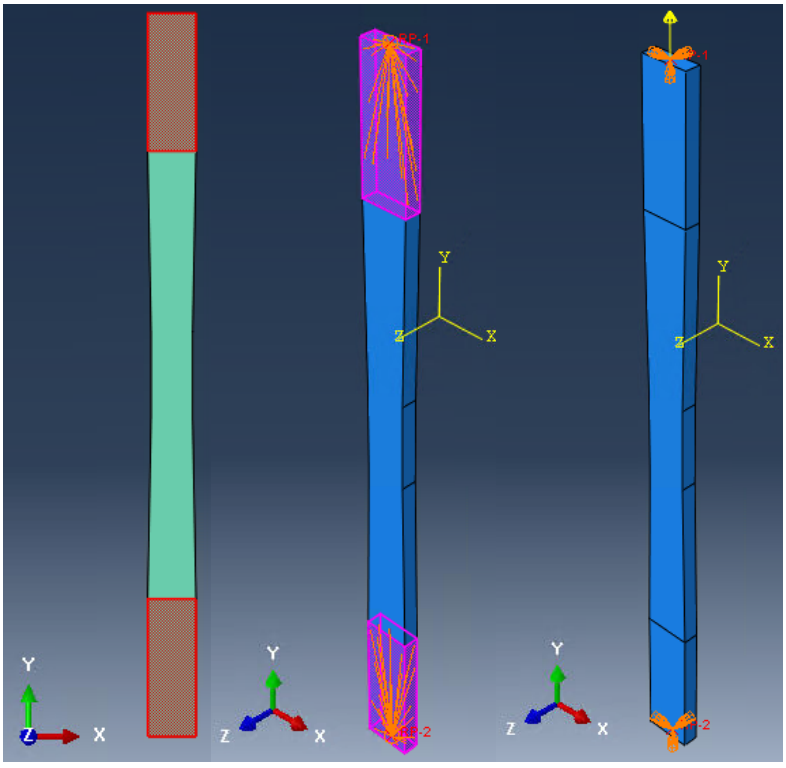

(a) Partitioned areas **(b)** Kinematic coupled areas **(c)** Reference points with BC's

Figure 6.1: Boundary condition set-up

6.2. Load conditions

With all boundary conditions in place, the next step is to apply the loading conditions to the model for the fatigue test. The first loading stage is applying the initial load in the coupon, making sure that the tensile force is present in the coupon. This load is equal to the maximum force that will be applied for the load level. To make sure the load is applied gradually and does not cause immediate damage to the material, a smooth step function is used. After the initial tensile load is in place, a tensile-tensile cyclic loading (Figure 2.3b) is applied with a certain load ratio. For this study, the only load ratio applied is 0.1 (eq. 2.5). The two different stages are shown in Figure 6.2, this example is showing the load stages for the 50 kN load level. For this load level, a load ratio of 0.1 indicates that the stress will fluctuate between 5 kN and 50 kN.

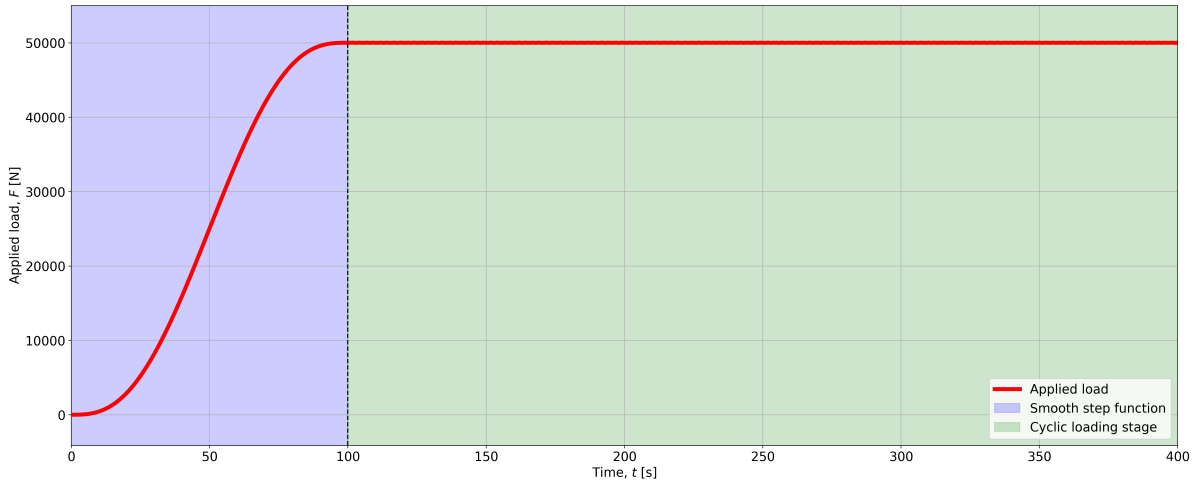

Figure 6.2: Two different loading stages

As can be noticed in the figure, the actual cycles are not exerted during the cyclic loading stage. Instead, the load is held constant at the maximum force at each increment during the analysis for the entirety of the calculation until failure occurs. This procedure is called the simplified cyclic loading (SCL) procedure [14]. During the analysis, the effects that are created by the different stress ratio are processed within the constitutive model. In addition to this, the amount of cycles and damage accumulation will be handled inside the constitutive fatigue damage model as well.

The main reason for using this SCL approach is that it offers more efficiency in terms of computational time. It no longer requires simulating the constant amplitudes of the cyclic loads, but instead can keep a constant force. If you model the full cyclic loading during the entire simulation, you need many increments for each cycle. This is comparable to the situation of applying the initial load with the smooth step function shown in Figure 6.2. Due to mass inertia effects, you need to take a large amount of seconds to apply the full load. For reference, based on the smooth step function shown in Figure 6.2, one cycle is performed in 200 seconds. The 200 seconds can be reduced depending on the load level as long as the increments remain stable, but is currently taken as the reference time step. During these 200 seconds, a total of 50,000 increments have been performed. In this same reference period, with the SCL method in combination with a cycle jump factor (further explained in sections 6.3.1, 6.4.1 and 6.6.3) of 0.05, one can instead perform 2500 cycles. This makes the SCL approach highly effective for high-cycle fatigue tests.

There are two types of solvers available for performing analyses in Abaqus, implicit and explicit solvers. Both solvers use a different algorithm to solve analyses, mainly differing in the method that time increments are handled. The implicit solver is offering short computational time due to performing large time increments at once. However, if many shorter time increments are required for the analysis, this will result in a longer computational time since the computational time per time step is more time-consuming compared to explicit solver. For highly non-linear problems with a very small time increment step, the explicit solver is best suited. The computational time per time step is much lower, due to the fact that the

explicit solver is able to calculate the new state directly from data available from the old state. Whereas the implicit solver first needs to solve a set of nonlinear equations before continuing with the calculation.

That is why the Abaqus/Explicit solver is used for the dynamic calculations. The stable time increment is targeted at 0.004, with the amount of increments varying between 100,000 and 3,000,000 increments, depending on the load level. The implicit solver does not only take longer to calculate, but might also struggle with finding the converged solution in this nonlinear problem.

6.3. User subroutine

In Chapter 2, one of the topics addressed is the different types of fatigue damage models that can be used in order to predict the fatigue life. The last model addressed, the progressive damage model, is the method which is chosen to use here. There were two possible damage model classes, based on physically observable phenomenon or based on damage growth of a specific residual mechanical property of the composite. The FEA will be based on this last class, for which the material property chosen is the residual stiffness of the composite.

To implement fatigue damage based on the residual stiffness, a user subroutine will be used in Abaqus. The user subroutine which is used is the VUSDFLD user subroutine. The characteristic of this subroutine is that you can define field variables to each element output point, based on a function of time or any other element output point quantities such as strains and stresses. These field variables can be assigned to any variable you choose, after which it can be used to perform calculations or set limits. All the results from the field variables are stored and can be read in Abaqus after an analysis is performed. The user subroutines are based on the programming language Fortran. The main advantage of this programming language is the computational power. However, since it is relatively old, it does come with some limitations. If an error occurs, a general error will be given. There is no detailed error information to retrace back why the code is incorrect. This means that one has to retrace back all lines of code until the error is found. In addition to this, a limited amount of support can be found online discussing these use cases.

The aim of the analysis is to perform a full numerical analysis, predicting the fatigue life of a homogenized material as a function of damage. In this particular case, the damage is expressed in terms of reduced stiffness, based on local stress states in the material. This will be expressed as a function of the amount of cycles. As a result, the amount of cycles at the failure limit are established, as well as the location where failure will occur. An overview of the steps taken is given in Figure 6.3.

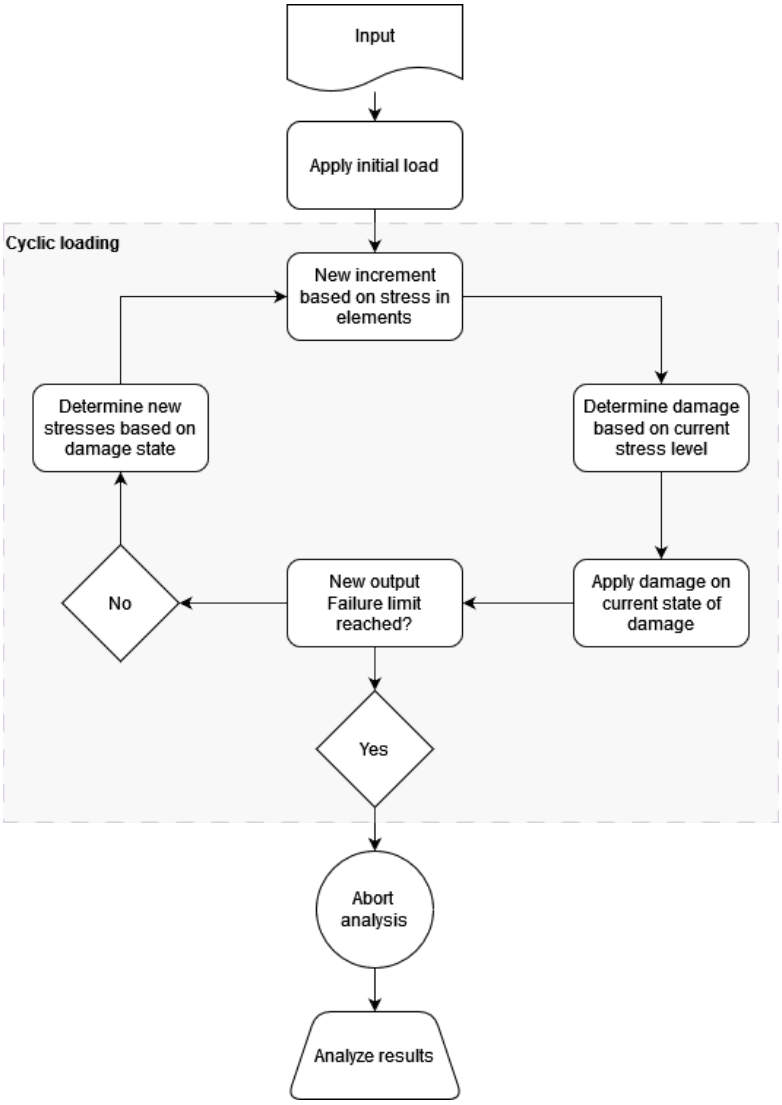

Figure 6.3: Procedure User subroutine

A more detailed explanation about the code itself is given below, providing more insight in the different sections of the code. The complete code is not included in this report due to confidentiality reasons. The first part of the code contains all variables which are defined for the user subroutine, most of these variables contain information that is passed on from the Abaqus model itself to the code, some of these variables can be used later on in the code where needed.

Next up is defining the material properties of the homogenized material in the script. These are the Young's Modulus in longitudinal direction and the stress/strain damage criterion. The Young's modulus is already determined with the Classical Laminate Theory (CLT) (32340 MPa from eq. 6.1) and the stress/strain parameters are based on the static tests that have been performed.

The stress/strain parameters are implemented with a simplified method. Figure 4.3 contains the stress/strain diagram on which this simplification is based. Five points along the line are chosen which are indicated with the letters e, p, c, b and f. The coordinates of the points are given in Table 6.2.

Table 6.2: Coordinates of Stress/Strain fitting line

Location	Stress [MPa]	Strain [mm]
Origin	0	0
e	135	Stress/EEt + 0.2
p	300	Stress/EEt + 0.4675
c	425	Stress/EEt + 0.675
b	578	Stress/EEt + 0.98
f	0	Strain_b + 0.05

The resulting fitting line with these coordinates is shown in Figure 6.4, this line is what determines the stress/strain damage criterion for the homogenized material in tension.

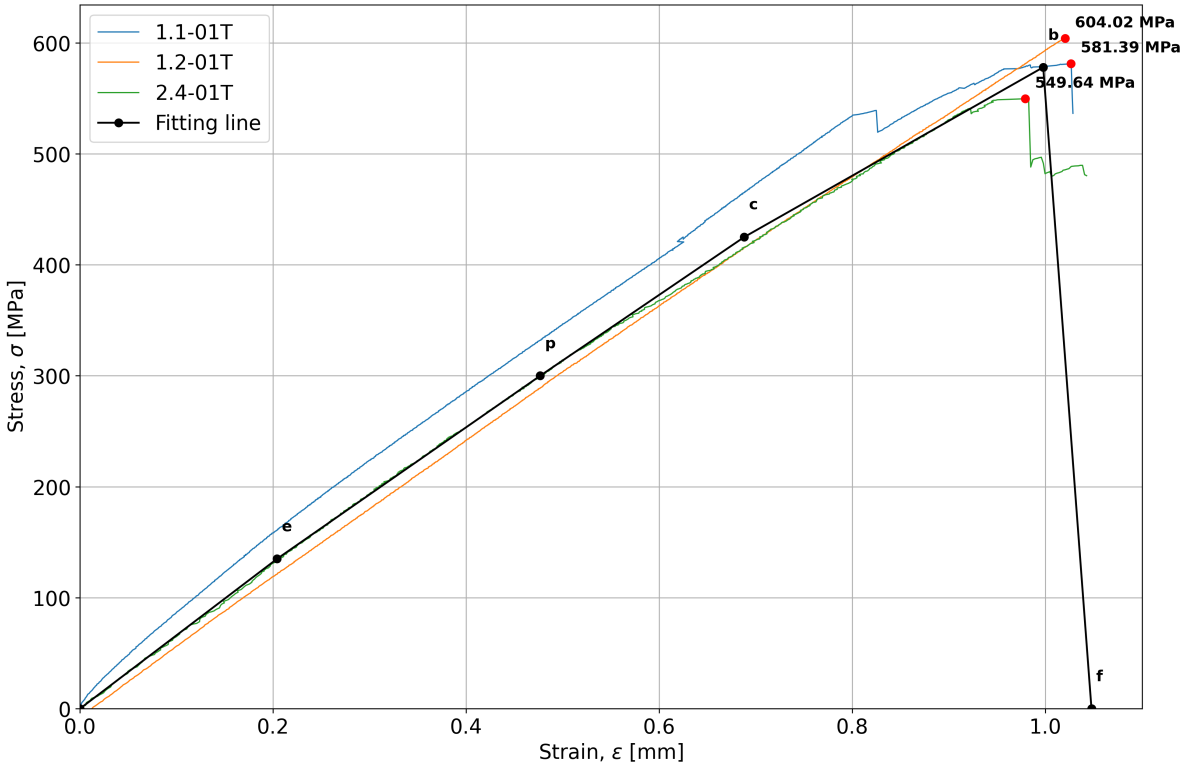

Figure 6.4: Determining of Stress - Strain damage fitting line based on experimental results

As mentioned before the analysis contains two load stages, first is the loading stage during which the tension force is applied, secondly is the cyclic loading stage. The user subroutine directs both stages after each other. To define how long this initial loading stage should take, a parameter is defined as tp_load. During the specified amount of time, the load is linearly increased until the required mean load is reached. This is the final step in the initial loading stage.

6.3.1. Continuum Damage Mechanics model

For the second part of loading, the model simulates cyclic loading to mimic the stiffness degradation that occurs due to fatigue. The method chosen is based on a Continuum Damage Mechanics (CDM) model, which determines the damage D occurring in the material, in this case the GFRP coupons.

Unlike other models that for example base damage on the number of cycles, the CDM model here recalculates the current damage and stress at each material point with every time increment. In more detail, the process works as follows:

- For each material point, the current stress is calculated.
- Based on this existing stress, the model determines the amount of damage occurring at that specific element.
- This new damage is added to the material element.
- The process repeats for all elements in the model.

This approach allows the model to compute the exact increment of damage for each element after every cycle, based on the current stress concentrations. This process continues until one of the elements reaches the failure limit. There is a relation between the time increment given in the model, and the amount of cycles that is represents. For all models, a time step of 0.004 is chosen, this means that for every virtual second, a total of 250 increments are performed. To express the relation between increments and cycles, the cycle jump factor 'dN_fix' is introduced in the subroutine. The value 'dN_fix' indicates the amount of cycles that each increment represents. This will be further explained in sections 6.4.1 and 6.6.3.

The inner workings of this user subroutine will be explained in more detail now. As mentioned, the subroutine is based on the stress levels. For each increment executed in Abaqus, a new stress is calculated, which will be transformed into damage being exerted on the material. In order to determine the amount of damage that is done each cycle, a special methodology is used. This entire process for determining the amount of damage per cycle is explained in subsection 6.3.2. This is implemented by setting up an equation for the damage, depending on the stress (eq. 6.11). Following implementing this in the subroutine script, the entire calculation process listed above can be executed.

The model will run until the failure in the coupon has occurred, this is at the point where the stiffness degradation limit is reached. Once this simulation is successful, the results can be exported and interpreted for further analysis.

6.3.2. Methodology for determining the variables

As explained earlier, the entire CDM model is based on the damage that is occurring in each element due to the stresses involved. The chosen variable to express the limit when failure occurs, is the stiffness degradation. Based on data gathered during the experiments performed in the lab, stiffness degradation curves are determined for all load cases. In order to implement the stiffness degradation curves, a method for expressing these curves is required. A method for formulating the curves was set up in Excel. The foundation of the Excel was created by Dr. M. Pavlovic, who previously experimented with the same concept for a different material and application.

All the data used for the determination of the stiffness degradation curves is originating from experiments performed on coupons without imperfections. Data for three load cases was gathered, 30 kN, 50 kN and 70 kN, all with a load ratio of 0.1. These curves are shown in Figure 5.11. As a method of creating a fitting curve along the path of the stiffness curve, a formula for a similar shape had to be found. The shape that was used is based on an ellipse, expressed in terms of parameters that are related to the stiffness degradation curve. Only the first quadrant of the ellipse is required for fitting the stiffness degradation curve. The standard formula for an ellipse centered in coordinate point (h, k) is shown in equation 6.6.

$$\left(\frac{x-h}{a}\right)^2 + \left(\frac{y-k}{b}\right)^2 = 1 \tag{6.6}$$

For this particular case, the parameters are altered to the following form shown in equation 6.7.

$$\left(\frac{log(n)}{log(N)}\right)^{\alpha} + \left(\frac{\frac{E}{E.0} - \frac{E.end}{E.0}}{1 - \frac{E.end}{E.0}}\right)^{\beta} = 1 \tag{6.7}$$

Several new parameters are introduced here, but they are all known or can be determined. E is the stiffness over time, $E.0$ is the stiffness at the start, and $E.end$ is the stiffness at failure. At the beginning, $\frac{E}{E.0}$ is equal to 1.0 for all cases. Over time this ratio progresses towards the failure stiffness limit. $\frac{E.end}{E.0}$ depends on the stiffness at which the failure occurred for each load. Section 5.4.1 goes into more detail at which normalized stiffness value each load level fails. For simplification reasons, the choice

was made to set this at 0.90 for all cases. A possible alternative for this simplification is to do make this parameter as a variable. This approach will be discussed in section 6.6.5. N indicates the final amount of cycles at failure, n is shifting over time. By tweaking the parameters α and β, the desired fitting curve can be achieved. An overview of the used parameters is provided in Table 6.3.

Table 6.3: Parameters for stiffness degradation fitting curves

	30 kN	50 kN	70 kN
α	3	4	4
β	1.4	2	2
N [Cycles]	220000	12000	3000
$\frac{E.end}{E.0}$	0.90	0.90	0.90

The resulting fitting curves are displayed in Figure 6.5. The black line indicates the fitting curve, while the underlying lines are the ones based on the data gathered during experiments. The fitting curve is based on $\frac{E}{E.0}$, this is determined by rewriting equation 6.7.

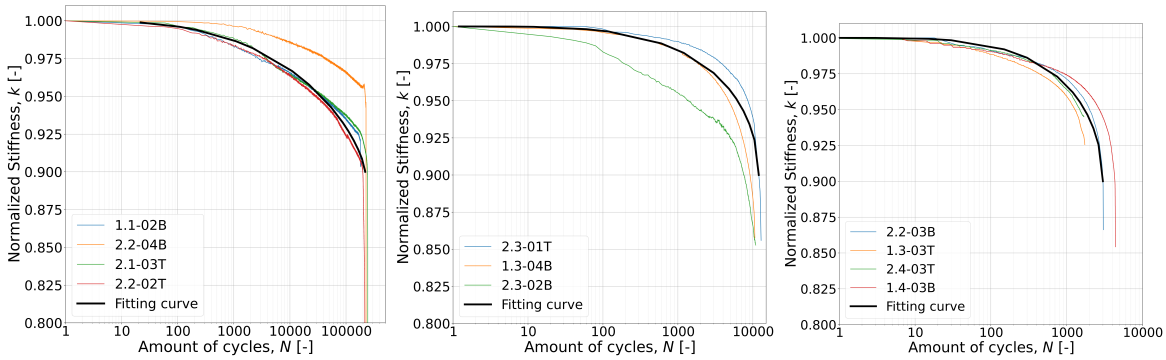

Figure 6.5: Fitting curves stiffness degradation for load levels (a) 30 kN, (b) 50 kN and (c) 70 kN

As $\frac{E}{E.0}$ is determined for a range of cycles to plot the fitting curve, the overall damage D in terms of stiffness can be extracted as well (eq. 6.8). The damage will be plotted in two forms, one over the amount of cycles (Figure 6.6), and one over the total amount of damage (Figure 6.7). Both of these lines are based on interpolation between two points. The later one is the most important plot that will be used further.

$$\text{Damage} \quad D = 1 - \frac{E}{E.0} \tag{6.8}$$

$$\frac{dD}{dN} = \frac{D_n - D_{n-1}}{n_n - n_{n-1}} \tag{6.9}$$

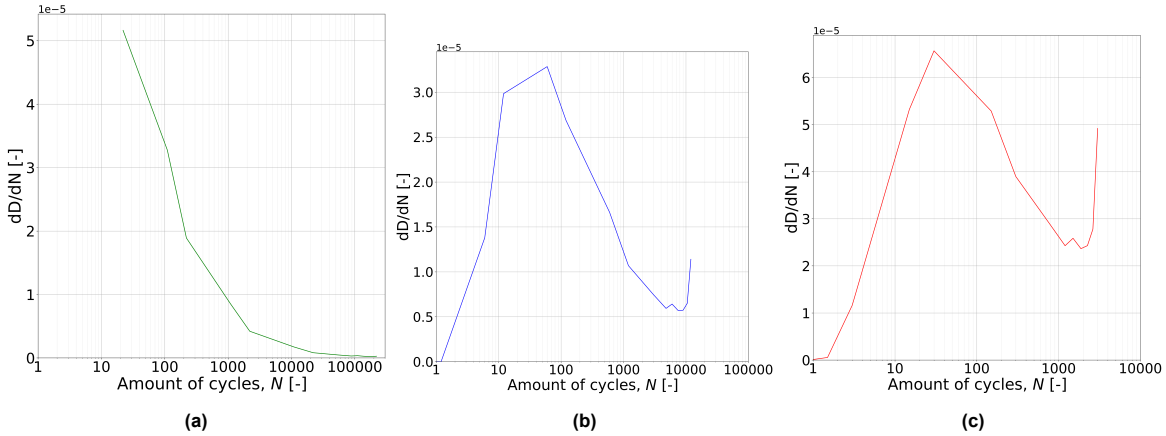

Figure 6.6: Damage per cycle vs. amount of cycles for load levels (a) 30 kN, (b) 50 kN and (c) 70 kN

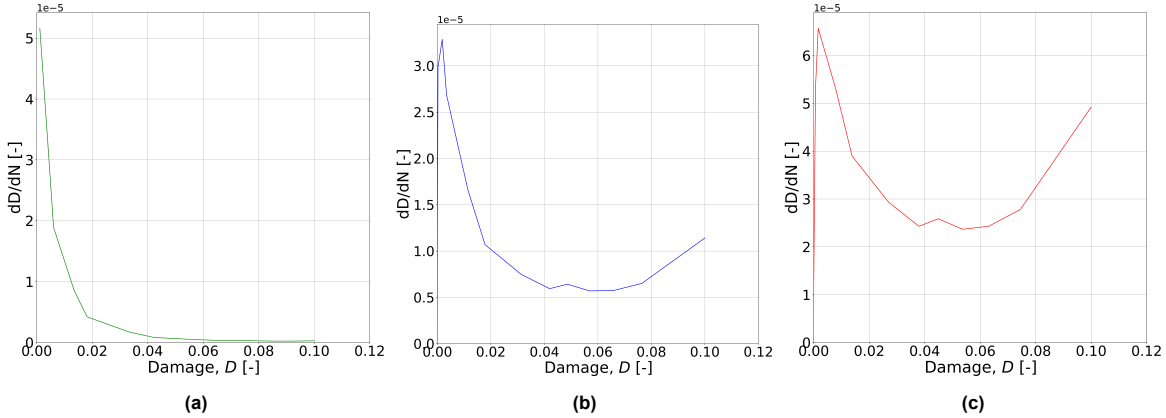

Figure 6.7: Damage per cycle vs. total damage for load levels (a) 30 kN, (b) 50 kN and (c) 70 kN

As mentioned, Figure 6.7 is the main plot that will be used in the next part of implementing the damage into the script. The plot illustrates the amount of damage being done per cycle on the vertical axis, while illustrating the total amount of damage that is already done on the horizontal axis. This line is based on fifteen points, with fitted lines between the points. Immediately, the observation is made that the shapes of the lines differ. The graph for 30 kN is shaped as an ellipse, while the graphs for 50 kN and 70 kN both show a parabola shaped line instead. This is in direct relation to the behavior of failure that is occurring for the coupons under each load case.

The failure at 50 kN and 70 kN appears to be more sudden towards the end. There is a quick decline in the stiffness before failure. Under the 30 kN load, the failure appears to be more graduate, the degradation starts relatively early and declines slowly over the amount of cycles. The slope becomes constant over the amount of cycles, which is more difficult to see now because of the logarithmic axis. This phenomenon of low damage near the end is confirmed by the graph in Figure 6.7a. For 30 kN the $\frac{dD}{dN}$ starts off high and slowly declines, with eventually very low damage per cycle until the limit of 0.1 ($D.th$) is reached. This is in clear contrast with 50 kN and 70 kN its behavior. They both start with high damage per cycle which slowly declines until midway, after which a sudden increase in damage is started. This results in high damage for the last couple of cycles, causing the sudden failure of the coupons.

To implement this behavior into the script, a new method with fitting curves is created. For the first attempt, a new fitting curve based on an ellipse is tried. The equation for the ellipse is now dependent

on different parameters. The equation for the fitting curves is:

$$\left(\frac{\log(D)-\log(D.0)}{\log(D.th)-\log(D.0)}\right)^{\gamma}+\left(\frac{\log(\frac{dD}{dN})-\log(\frac{dD}{dN.th})}{\log(\frac{dD}{dN.0})-\log(\frac{dD}{dN.th})}\right)^{\theta}=1 \tag{6.10}$$

From this equation, you want to extract the value $\frac{dD}{dN}$ which you will plot over the total amount of damage D. This can be achieved by transforming the equation such that all other parameters are moved to the other side. Several parameters are taken as input, an overview of all the parameters is given in Table 6.4.

Table 6.4: Parameters for damage fitting curves

	30 kN	50 kN	70 kN
σ [MPa]	124.2	218.6	302.5
$\frac{\sigma}{\sigma_{ult}}$	0.215	0.378	0.523
D.0	$1.0\cdot10^{-8}$	$1.0\cdot10^{-8}$	$1.0\cdot10^{-8}$
D.th	0.1	0.1	0.1
γ	15	11	11
θ	0.3	0.475	0.475
$\frac{dD}{dN.0}$	$5.5\cdot10^{-5}$	$4.0\cdot10^{-5}$	$7.5\cdot10^{-5}$
$\frac{dD}{dN.th}$	$3.9\cdot10^{-7}$	$3.5\cdot10^{-6}$	$1.8\cdot10^{-5}$

In this table, the σ_{ult} is taken as defined in Table 4.2. As explained in section 6.3.1, the code is build up around the parameter $\frac{dD}{dN}$, indicating the amount of damage added per cycle. To be able to define this value for all load cases containing different parameters, a variable has to be defined to express all other parameters. This variable is the ratio between the stress σ, and the ultimate stress limit σ_{ult}. Abaqus can determine the stress in each element, and accordingly, calculate all other parameters required to determine $\frac{dD}{dN}$.

$$\frac{dD}{dN}=10^{\left(\left(1-\left(\frac{\log 10(D)-\log 10(D.0)}{\log 10(D.th)-\log 10(D.0)}\right)^{\gamma}\right)^{\frac{1}{\theta}}\cdot\left(\log 10(\frac{dD}{dN.0})-\log 10(\frac{dD}{dN.th})\right)+\log 10(\frac{dD}{dN.th})\right)} \tag{6.11}$$

Table 6.4 contains four variables that are changing depending on the load, θ, γ, $\frac{dD}{dN.0}$ and $\frac{dD}{dN.th}$. Three of these have been expressed, depending on the $\frac{\sigma}{\sigma_{ult}}$ ratio. The method used is by first plotting the data points in a graph on the vertical axis, while having the stress ratio on the horizontal axis, and create trend lines between the points such that the line predicts the locations of the points as accurate as possible. The resulting initial equations are equations 6.12 to 6.14, also shown in Figure 6.8.

$$\gamma=79.426\cdot\left(\frac{\sigma}{\sigma_{ult}}\right)^{2}-71.605\cdot\frac{\sigma}{\sigma_{ult}}+26.72 \tag{6.12}$$

$$\theta=0.5779\cdot\frac{\sigma}{\sigma_{ult}}+0.2016 \tag{6.13}$$

$$\frac{dD}{dN.th}=0.0003\cdot\left(\frac{\sigma}{\sigma_{ult}}\right)^{4.2584} \tag{6.14}$$

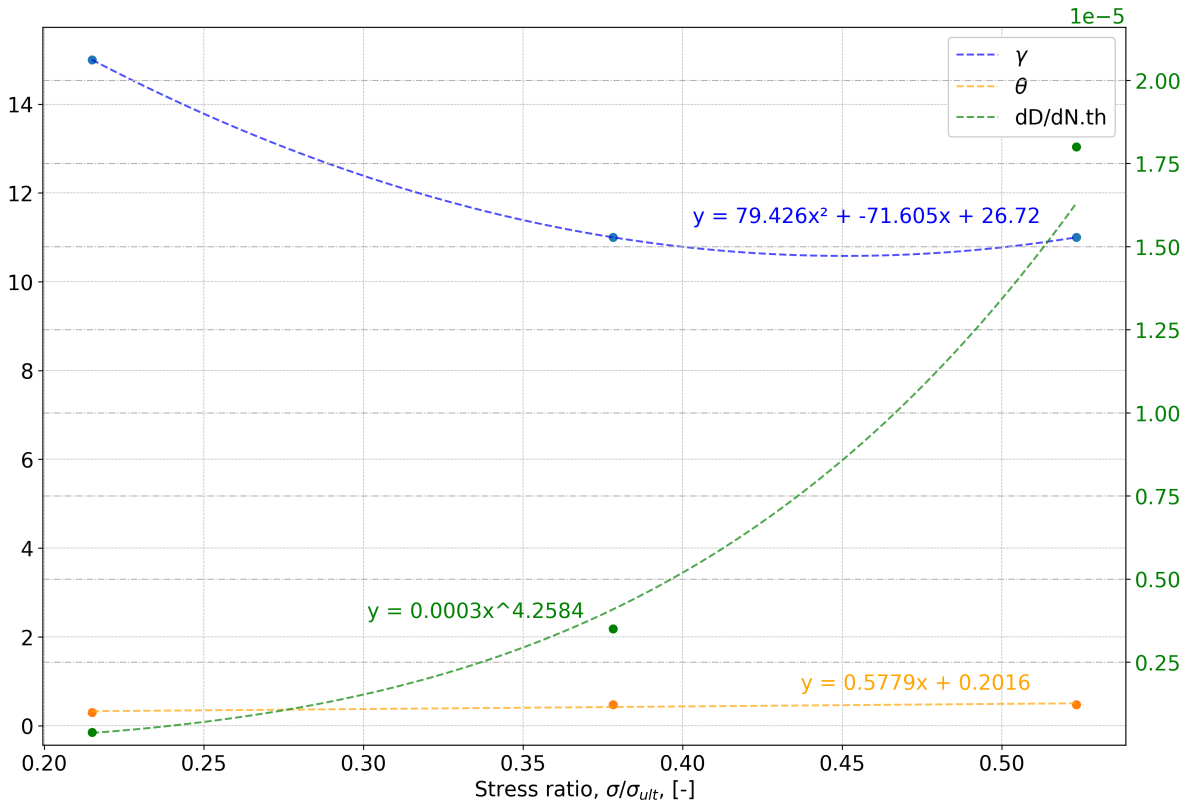

Figure 6.8: Trend lines for damage variables for first iteration, expressed in terms of stress ratio

The shapes of the trend lines are different, depending on what fits best. That is why γ is parabola shaped while θ is linear and $\frac{dD}{dN.th}$ is based on a power function. The resulting fitting curves per load level are shown in Figure 6.9.

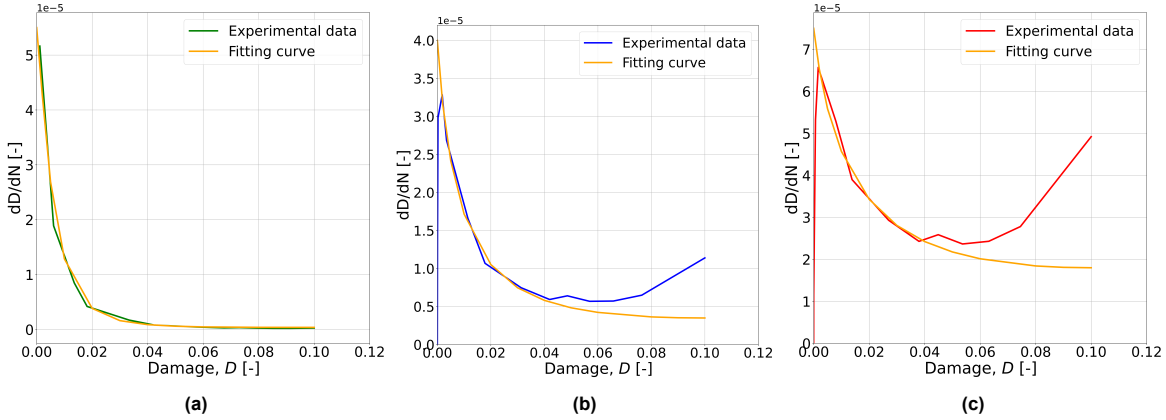

Figure 6.9: Damage per cycle vs. total damage incl. fitting curve first iteration for load levels (a) 30 kN, (b) 50 kN and (c) 70 kN

As explained, the fitting curves are based on an ellipse. Due to the difference in shapes between the various loads, not all the resulting fitting curves are accurate. The graph in Figure 6.9a has the most accurate fit, being a near copy of an ellipse. Due to the 50 kN and 70 kN curves having a parabolic shape, only the first part of the fitting curve describes the actual damage being done. After this threshold midway, the damage based on the fitting curve holds a linear decrease while in reality the damage increased again. For a complete overview, all curves are shown in Figure 6.10.

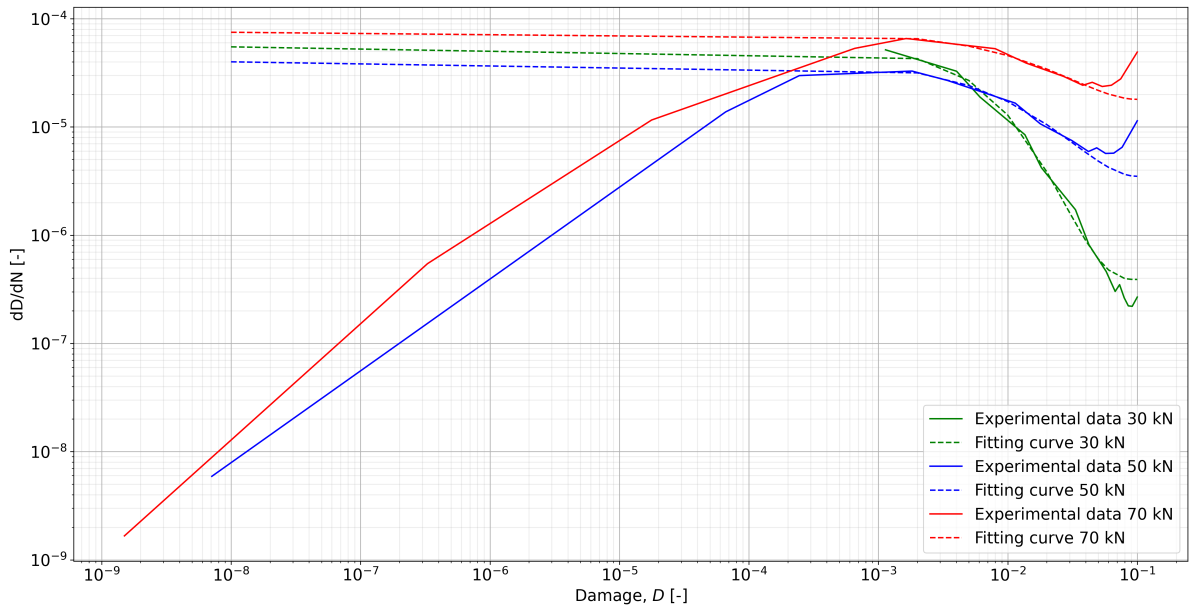

Figure 6.10: Experimental data compared to fitting curves

The most important part of this graph is the last part, starting from 10^{-3}. All lines show a clear fit, only starting to deviate towards the final stage of damage. Here can be noted that even the fitting line of 30 kN starts to deviate. However, since this is only in the region of $1.5 \cdot 10^{-6}$, this difference is considered negligible.

6.4. Initial results

6.4.1. Exporting the results

Despite knowing that the fitting curves to describe the damage are only fitted accurately in the first half of the damage curve, still an initial simulation was performed. In Abaqus, certain parameters are defined as state variables, these values will be stored for reading after the calculation. This allows for good insights in the values that are used for each variable during the calculation. In addition to this, the stiffness degradation curve can also be determined with an intermediate step.

For the determination of the stiffness degradation curve, a limited amount of information is exported from the Abaqus model.

- Displacement
- Reaction Force
- Increment

Starting with the displacement of the coupon, this is required for determining the strain ϵ. As part of the Abaqus model, a simulated extensometer is created. This extensometer is located in the middle of the coupon, and has a gauge length of 50 mm. During each increment of the test, the displacement of both sides of the extensometer (U1 and U2) are measured and logged into the database. One of the ends of the coupon is clamped while the other side is displaced in longitudinal direction. In this clamped edge, the reaction force is exported for further analysis. The last information exported from Abaqus is the number of increments that is performed at each data point. The amount of increments between each step can be set beforehand, affecting the amount of data points and accuracy of the intertwining values.

The above exported parameters are in direct relation with the required information for the stiffness degradation curve. The parameters you want to determine are; the stress, the strain, the stiffness, and the amount of cycles for each of these data points. The strain is determined based on the displacement

provided by the extensometer.

$$\epsilon = \frac{\text{U2 - U1}}{\text{Gauge length}} = \frac{\text{U2 - U1}}{50} \tag{6.15}$$

The stress is determined based on the reaction force and the cross-sectional cross area of the coupon.

$$\sigma = \frac{\text{Reaction Force}}{\text{Cross-sectional Area}} \tag{6.16}$$

The stiffness is calculated with the determined stress and strain.

$$K = \frac{\sigma}{\epsilon} \tag{6.17}$$

And lastly, the amount of cycles is determined based on the amount of increments that are performed. In order to determine the ratio between the amount of increments and the amount of cycles, the cycle jump factor 'dN_fix' is used. When Abaqus performs the calculation, this parameter defines the amount of cycles worth of damage should be done during each increment. As an example, if 'dN_fix' is set to 0.05, and 100,000 increments have been performed until failure, this corresponds to a total amount of 5,000 cycles until failure. The influence of this parameter on the accuracy of the calculation will be investigated in more detail in subsection 6.6.3.

All mentioned above parameter values have been exported from the Abaqus model. This results in the following stiffness degradation curves shown in Figure 6.11. The black line represents the results extracted from the FE model.

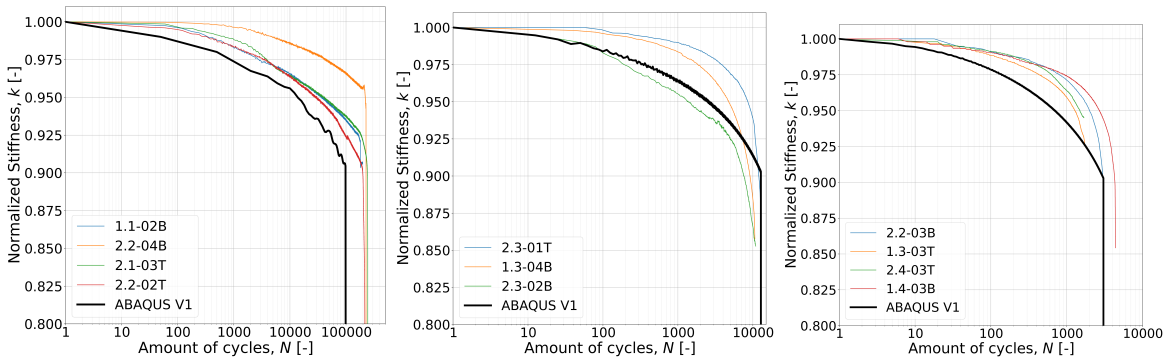

Figure 6.11: Results first iteration, stiffness degradation curves for load levels (a) 30 kN, (b) 50 kN and (c) 70 kN

Between the load levels, a variance can be found in terms of amount of data points available. Figure 6.11a has a limited amount of data points, resulting in a non-fluent line, while Figures 6.11b and 6.11c are much more fluent. This is caused due to a difference in amount of intervals recorded, initially this was set for a large interval to save on computation time. However, after running several models, the conclusion came that decreasing the interval between points did not affect the computation time too much. So the decision was made to create a lot of data point intervals, one every second.

The largest difference between the results from the model compared to the experiments is regarding the slope of the stiffness degradation. For the Abaqus model, the damage starts almost immediately and gradually increases over the amount of cycles. This is in direct contrast with the experiments, the stiffness drop is low initially, only increasing rapidly in later stages of the tests.

Looking at the moment of failure, in terms of both the amount of cycles and the remaining stiffness left, they do match with each other. This indicates that the foundation of the user subroutine is solid, however, it requires adjustments to more accurately predict the damage behavior. The only exception in this case is with the low load case (Figure 6.11a). The amount of cycles until failure is underestimated by a factor of two. This is a point of attention in new versions of the subroutine. The next subsection will discuss the process of new iterations until the final version of the user subroutine.

6.5. Iterations

As explained, the first version of the subroutine makes use of an ellipse shaped fitting curve to fit with the damage predicting models. This resulted in an accurate fitting curve for the low load, but only a half fit for the parabola shaped curves. Therefore, a new approach will be tried.

6.5.1. 4th order polynomial

The second iteration is based on a polynomial shaped function. First, the idea rose to fit a 2nd order polynomial, also known as a parabola. But since the curves for 50 kN and 70 kN both have a horizontal part near the lowest point, known as the vertex, this was not possible to fit accurately. That is why a 4th order polynomial was tried to fit the curves as accurate as possible. Equation 6.18 is used for the new fitting curve for the damage per cycle over the accumulation damage. The graphs shown in Figure 6.5 until Figure 6.7 remain the same.

$$\log\left(\frac{dD}{dN}\right) = a \cdot D^4 - b \cdot D^3 + c \cdot D^2 - d \cdot D + \frac{dD}{dN.0} \tag{6.18}$$

The function is dependent on the amount of damage that has been accumulated, in combination with the variables that need to be defined, a until d. Each value is chosen such to represent the most accurate fit. The values used for each variable are shown in Table 6.5.

Table 6.5: Parameters for 4th order fitting curves

	30 kN	50 kN	70 kN
a	7.31	3.2	3.859
b	1.746	0.747	0.862
c	0.14306	0.06315	0.076
d	0.00468	0.0023	0.00305
$\frac{dD}{dN.0}$	$5.25 \cdot 10^{-5}$	$3.70 \cdot 10^{-5}$	$7.0 \cdot 10^{-5}$

The fitting curves created with the above-mentioned parameters are shown in Figure 6.12.

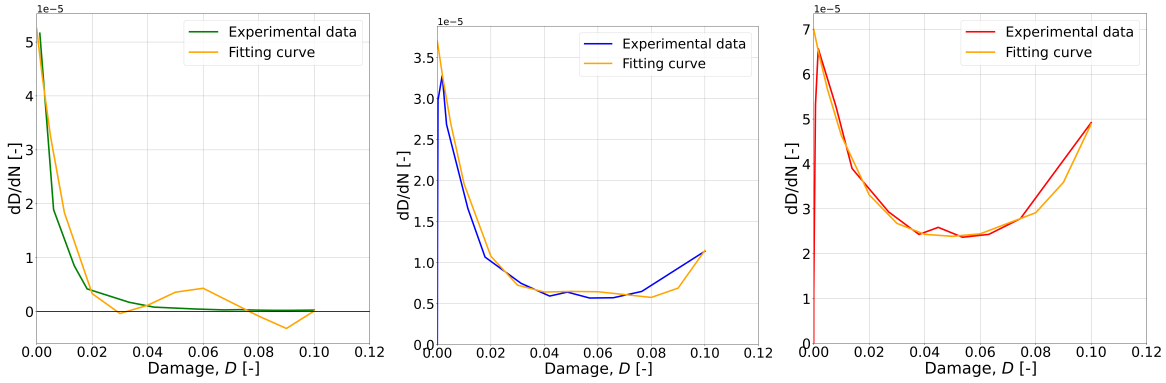

Figure 6.12: Damage per cycle vs. total damage incl. fitting curve based on 4th order polynomial for load levels (a) 30 kN, (b) 50 kN and (c) 70 kN

Both Figure 6.12b and Figure 6.12c showcase fitting curves that certainly for the first region describe an accurate fit. In the final stages, they deviate slightly, but still give an accurate value for the last stage. However, the most noticeable feature from these fitting curves is Figure 6.12a, which predicts the damage for the load level of 30 kN. When trying to fit a 4th order polynomial to this line, it is almost

unavoidable that the fitting curve goes into the negative domain for short periods. This is undesirable, since this implies that in certain cases negative damage would be applied to the material, resulting in additional fatigue life performance.

On top of that, the middle part of the fitting curve for 30 kN prescribes a large upwards peak. In order to remove the negative and peak values, certain restrictions should be tried to be implemented. Instead of pursuing this, the choice was made to switch to a different approach.

6.5.2. Cut-off ellipse

The third attempt is based on the first principle, the ellipse. The alteration here however is in the point at which the ellipse is cut off. Initially, the moment of failure, expressed by $D.th$, was set to 0.10. This indicates that at failure, the coupon still had 90% of its original stiffness (Figure 6.11). However, as shown in Figure 6.9, the resulting fitting curves did not fit with the parabola shaped damage curves.

The graph indicates the amount of damage that is being applied each cycle, based on the current state of damage. As mentioned before, the parabola shape is a clear indication that at the final stages of the test, the damage increases rapidly. This is resulting in the rapid failure behavior/stiffness degradation at the end. Based on this knowledge, it can be argued that the last 2.5% of damage only represents a very limited amount of cycles compared to the full test. This hypothesis is tested by again using an ellipse shaped fitting curve, but this time cut it off at 92.5% of the stiffness remaining.

The formula for the fitting curve is still the same as equation 6.10. The parameters however, have changed slightly. The altered values are given in Table 6.6, all other values remain the same.

Table 6.6: New parameter values for damage fitting curves, cut-off ellipse

	30 kN	50 kN	70 kN
D.th	**0.075***	**0.075***	**0.075***
γ	**14***	11	11
θ	**0.475***	0.475	0.475
$\frac{dD}{dN.th}$	$3.9 \cdot 10^{-7}$	$5.0 \cdot 10^{-6}$	$2.2 \cdot 10^{-5}$

* Bold values are altered compared to previous version

With these values, the new damage fitting curves are created. All new fitting curves are shown in Figure 6.13

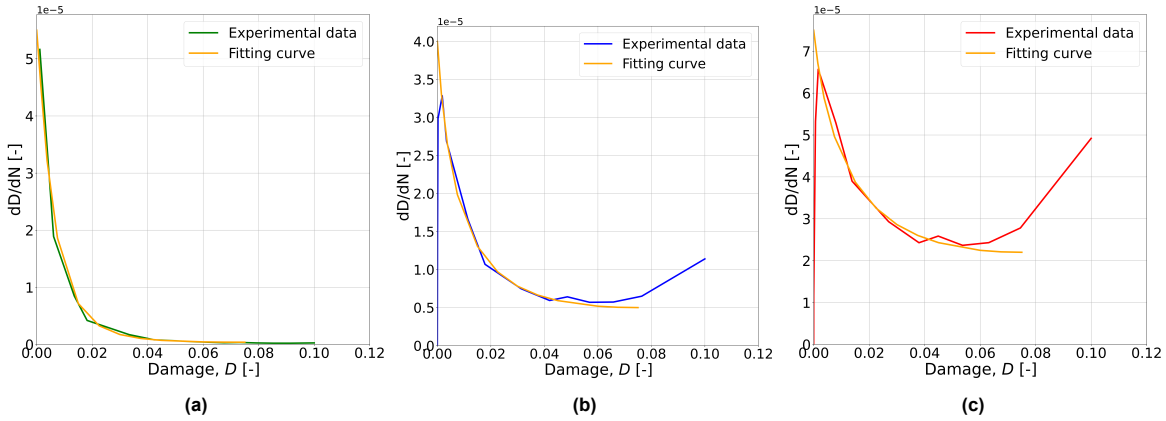

Figure 6.13: Damage per cycle vs. total damage incl. fitting curve based on cut-off ellipse for load levels (a) 30 kN, (b) 50 kN and (c) 70 kN

These new damage fitting curves are providing more accurate fits for all load cases, until the point of failure at 0.075 damage. In order to implement these new values in the user subroutine, new trend lines are established. These trend lines again are dependent on the stress ratio (Figure 6.14).

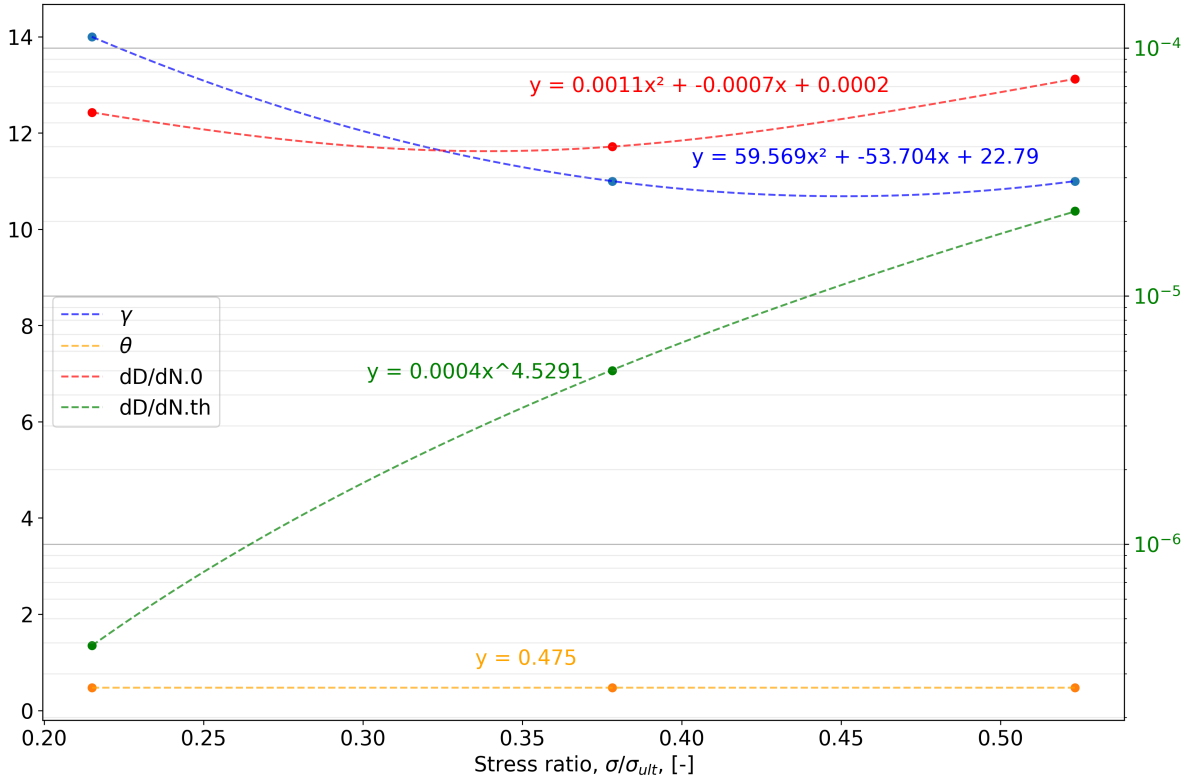

Figure 6.14: Trend lines for damage variables based on cut-off ellipse, expressed in terms of stress ratio

The vertical axis on the left side is related to Gamma and dD/dN.th and uses a normal distribution. The vertical axis on the right side is a logarithmic scale and is related to Theta and dD/dN.0. In this case, Theta is a constant, while dD/dN.th remains a power function and Gamma and dD/dN.0 both are a second-order polynomial function. With the new trend lines implemented in the user subroutine, a new attempt is performed to run the FE model. The new stiffness degradation curves are shown in Figure 6.15.

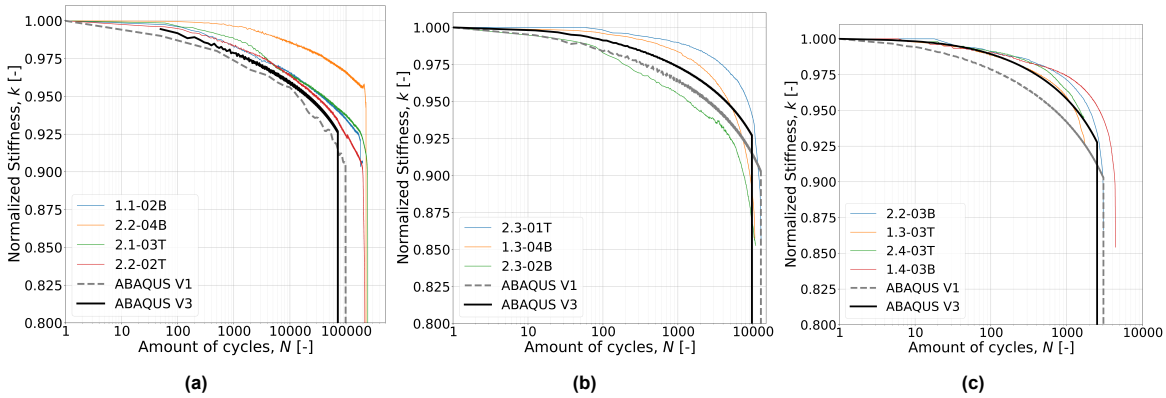

Figure 6.15: Results cut-off ellipse approach, stiffness degradation curves for load levels (a) 30 kN, (b) 50 kN and (c) 70 kN

For a better comparison, the results from the first attempt are also included as 'ABAQUS V1'. As expected, the failure for each load case occurs earlier due to the changed failure limit set. The difference

in amount of cycles is approximately 15-20%. This is slightly less than the failure limit was shifted. The main goal of this new approach was to create a better fitting damage curve prediction. Looking at the new stiffness degradation curves, it is noticeable that the slope of the Abaqus coupon is much more in line with the experimental result slopes. The stiffness degradation process is going more gradually now, as is desired. However, there is still room for improvement. The biggest improvement can be found in the prediction of the amount of cycles until failure, this is still on the conservative side now. On top of that, there is still room for improvement in terms of the slope of failure compared to the experimental results.

6.5.3. Rational functions

The estimation of the damage per cycle over the amount of damage with an ellipse fitting curve still did not provide the desired results. Therefore, other alternative methods were investigated. One of the options that was deemed promising was to create a fitting curve based on two rational functions combined. A rational function is defined as a function that can be written as the ratio of two polynomials combined. An example of a rational function is given in equation 6.19.

$$f(x) = \frac{P(x)}{Q(x)}, \text{where } Q(x) \neq 0 \tag{6.19}$$

$$f(x) = \frac{1}{x} \tag{6.20}$$

In this case, both P(x) and Q(x) should be polynomials of a certain degree. A commonly used rational function is given in equation 6.20. This function provides the foundation on which the new iteration is based. In this case, 1 is a constant, which is considered a polynomial of degree 0, while x is considered as a linear polynomial of degree 1. A rational function always has two asymptotes, a horizontal and vertical asymptote. The location of these asymptotes can be altered by implementing additional variables in the form of equation 6.21. The influence of each parameter is explained below, based on the examples given in Figure 6.16.

$$f(x) = \frac{b}{x + a} + k \tag{6.21}$$

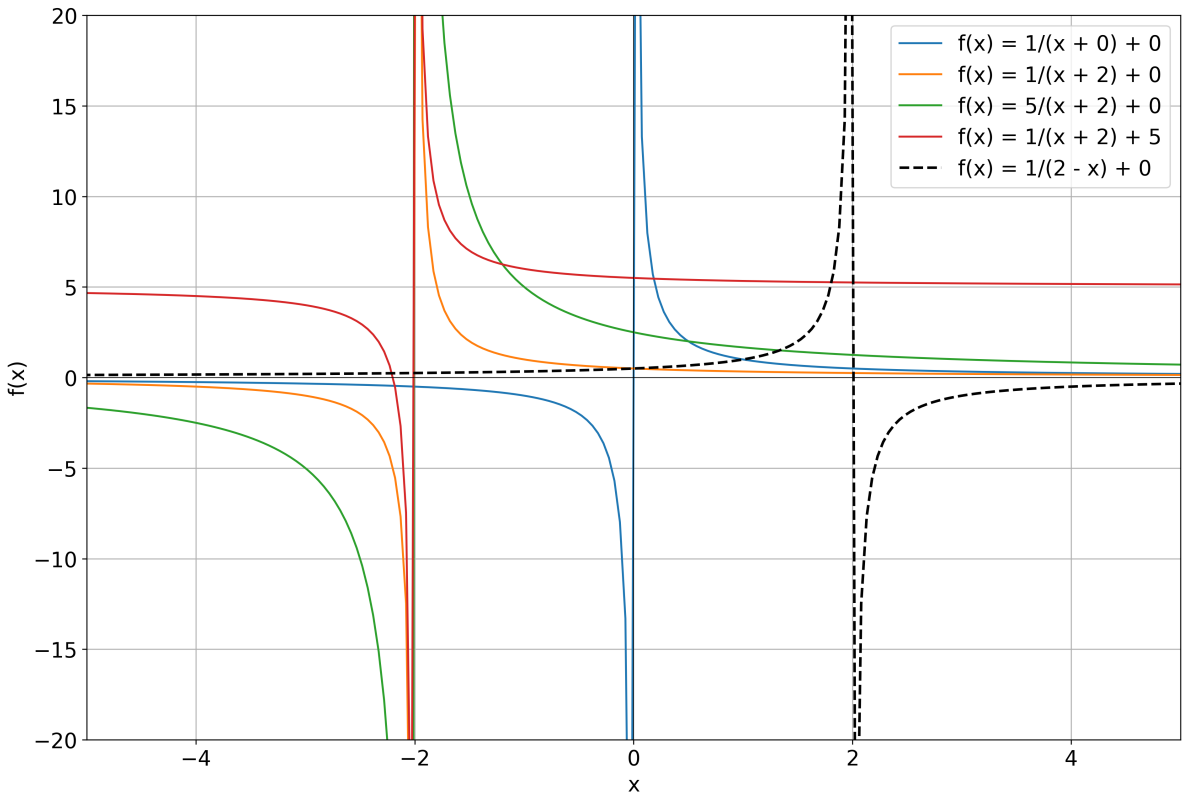

Figure 6.16: Rational functions - Influence of changing parameters

The standard form plotted is equal to equation 6.20, where b is set to 1. a is the parameter responsible for the location of the vertical asymptote. By increasing this value, the location of the vertical asymptote shifts towards the left as shown by the orange line. The parameter b is responsible for the curvature of the line, by increasing b, the curve decreases as can be seen with the green line. The other parameters are identical to the orange line, only the curvature has decreased. By letting b go close to zero, a very sharp curve can be created, this will be of use later for fitting the curves. The last parameter k is the location of the horizontal asymptote. In general, this is set to 0, which is the location of the x-axis. The red line is identical to the orange line, with the only difference being a shift upwards of 5.

Now, all this knowledge is applied to the new fitting curves for the damage per cycle over the total amount of damage. As mentioned beforehand, the new fitting curve will be a composed out of two rational functions. One of these functions will be the reflection across the y-axis of equation 6.21.

An example of a reflected line is shown in Figure 6.16. The black dashed line is a reflection on the y-axis from the orange line. By combining these two lines, in theory you can create a parabola shaped function with a large flat vertex. The final form of this equation used for the damage fitting curves is equation 6.22.

$$\frac{dD}{dN} = \frac{1}{x+a} \cdot b + \frac{1}{c-x} \cdot d \tag{6.22}$$

The major benefit of this setup, is that different forms of fitting curves can be created. This can be achieved by amplifying or suppressing one or both of the functions. The values shown in Table 6.7 are used to create new fitting curves.

Table 6.7: New parameter values for damage fitting curves, rational functions

	30 kN	50 kN	70 kN
a	0.001	0.005	0.007
b	$1.00 \cdot 10^{-7}$	$2.15 \cdot 10^{-7}$	$6.20 \cdot 10^{-7}$
c	0.000	0.115	0.122
d	0.00	$1.50 \cdot 10^{-7}$	$9.70 \cdot 10^{-7}$

The most noticeable values are for the load level of 30 kN. For this load level, both c and d are set to zero. This is done in order to complete suppress the second part of the function, which is responsible for the increase in the second part of the fitting curve. The 30 kN is the only load level without such an increase, for 50 and 70 kN, this part of the function is included. The final fitting curves are shown in Figure 6.17. Opposed to the variant with the cut-off ellipse at 0.075 damage, this model again works on the principle of the damage continuing until 0.1 damage has been inflicted.

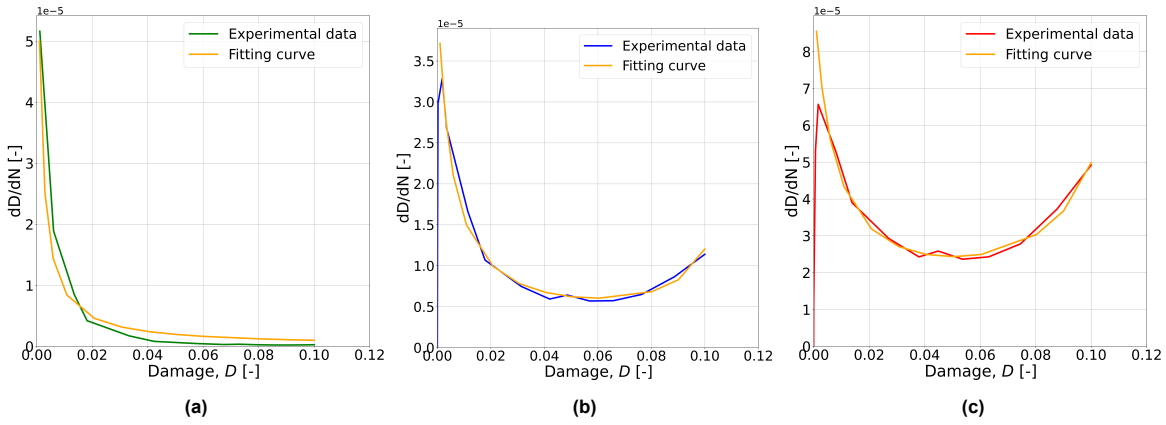

Figure 6.17: Damage per cycle vs. total damage incl. fitting curve based on rational functions for load levels (a) 30 kN, (b) 50 kN and (c) 70 kN

As can be seen, by suppressing the second part of the function, the fitting curve for 30 kN is successfully fitted as a monotonic decreasing curve. Both other fitting curves are a close fit as well, due to the possibility to create non-symmetrical parabola functions with equation 6.22. The next challenge was implementing these parameters into the user subroutine again to simulate the damage behavior. The first attempt is shown in Figure 6.18.

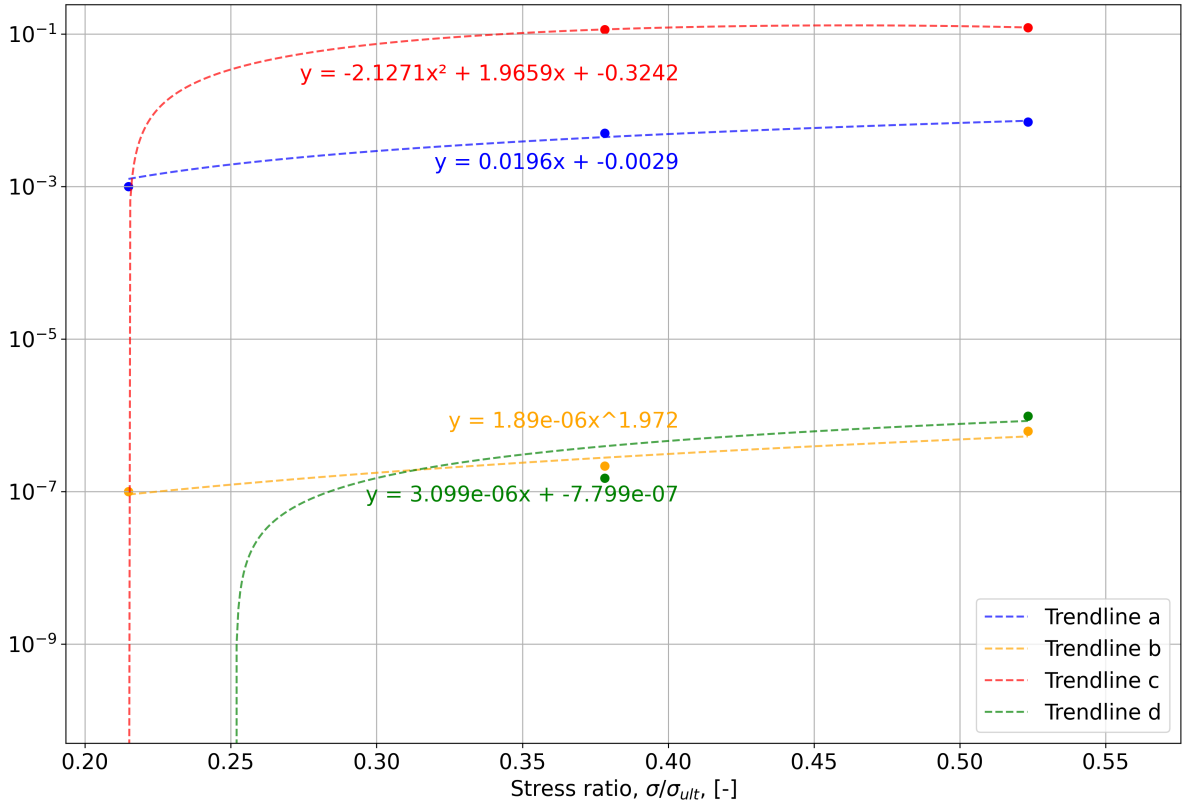

Figure 6.18: Trend lines for damage variables based on rational functions, expressed in terms of stress ratio

It is rather difficult to find a good fit for both c and d since these values go to 0 for the case of 30 kN. Both trend lines going to zero show behavior unsuited for giving stable values at stress ranges near 0.21. This can quickly change when looking near a stress ratio value of 0.25 for example. In this case, it will again provide stable results. Another disadvantage of these type of trend lines is the lack of possibilities for extrapolation of the values below 0.21 since it appears no solutions will be found in that case. Even so, as a first indication, it was still attempted to implement these trend lines to see the results for all load levels.

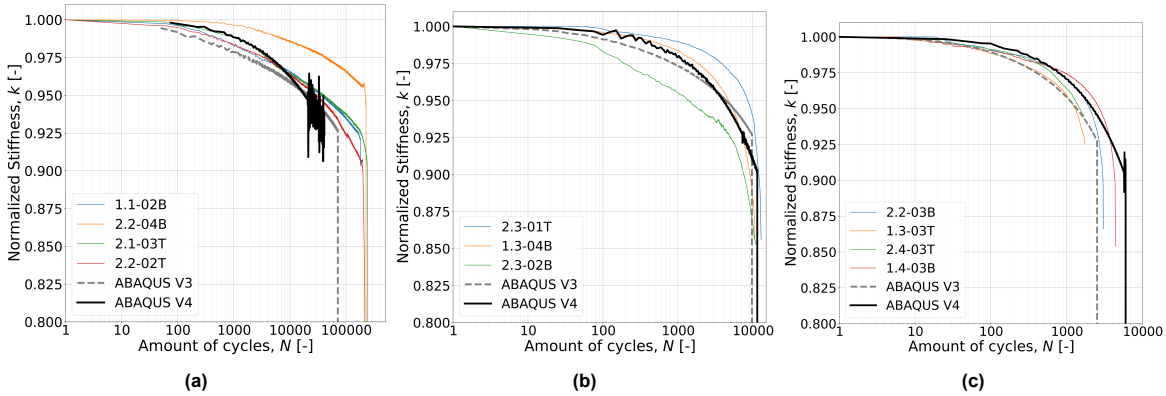

Figure 6.19: Results rational functions approach, stiffness degradation curves for load levels (a) 30 kN, (b) 50 kN and (c) 70 kN

All results from the FE model are shown in Figure 6.19. The 30 kN load level produces the most unstable results. This is partly as was expected beforehand. The main reason behind this unstable result is because of the factors c and d that should go towards zero. Both trend lines have troubles to go towards zero for this case, resulting in heavily oscillating behavior of the value, and stiffness degradation line. Due to being so unstable, the calculation is also stopped before failure is supposed to occur. Compared to the previous version V3, this is considered to produce worse results.

As for the result of 50 kN, those seem to be very comparable with the experimental results. The degradation slope is very similar to the average slope of the tests. The amount of cycles until failure is an almost exact match with the average from the experimental results. The 70 kN result also has a matching slope for the stiffness degradation, it only overestimates the amount of cycles until failure. This is mainly due to the stiffness degradation at the end not being as steep as during the experiments.

The points that still require improvement from this method are:

- Stability for 30 kN load level
- Amount of cycles until failure for 30 kN
- Slope of stiffness degradation for 70 kN
- Amount of cycles until failure for 30 kN

These problems are tackled with a new iteration of the user subroutine.

6.5.4. Non-zero parameter values

The root cause of the problems can be traced back to the trend lines shown in Figure 6.18 not fitting accurately. The main trend lines deviating the most are c and d due to the zero value. For the new iteration, instead of choosing zero values for c and d, a very small non-zero value is chosen.

Table 6.8: New parameter values for damage fitting curves, non-zero

	30 kN	50 kN	70 kN
a	0.001	0.005	0.007
b	$1.00 \cdot 10^{-7}$	$2.15 \cdot 10^{-7}$	$6.20 \cdot 10^{-7}$
c	$\mathbf{0.110}$	0.115	0.122
d	$\mathbf{1.00 \cdot 10^{-9}}$	$1.50 \cdot 10^{-7}$	$9.70 \cdot 10^{-7}$

The bold values in Table 6.8 are the only changes that have been applied. Since the values are changes only so slightly, the damage fitting curves are as good as identical to the ones shown in Figure 6.17. The main difference now is the change in the shapes of the trend lines, and the type of function of the trend line.

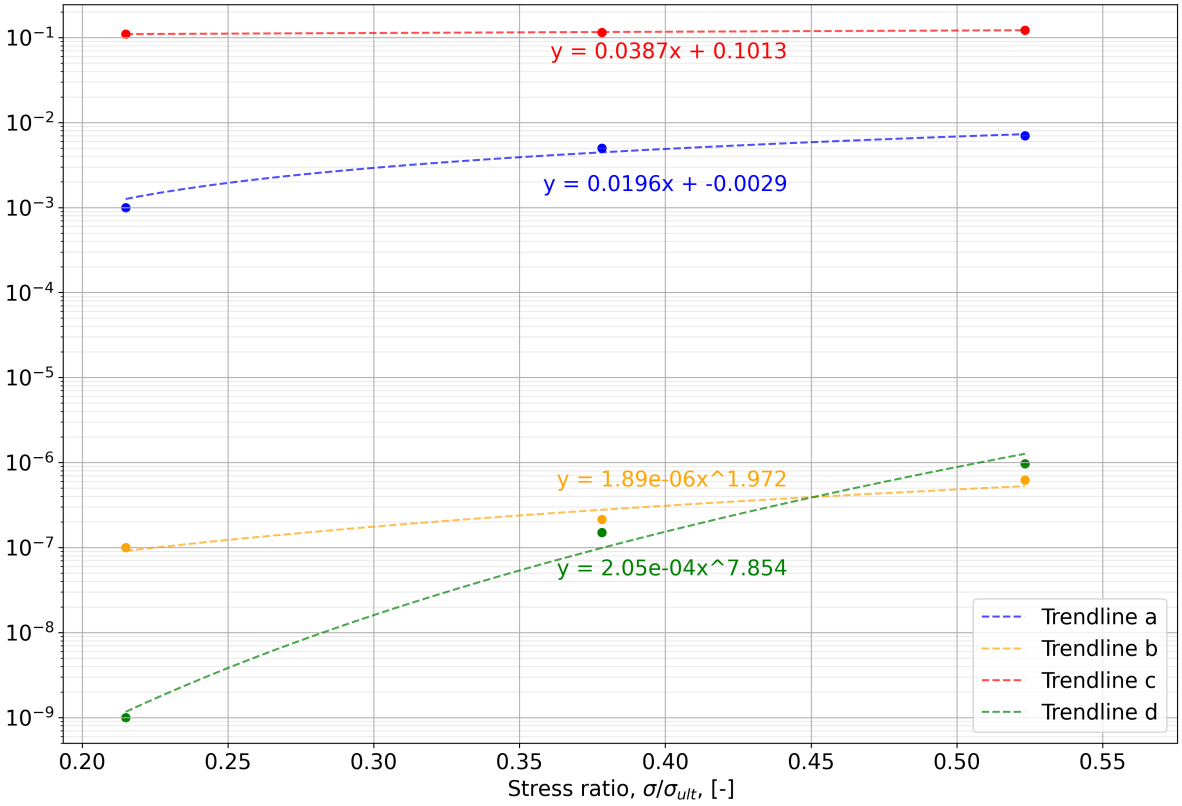

Figure 6.20: Trend lines for damage variables based on rational functions with non-zero values, expressed in terms of stress ratio

The new trend lines are shown in Figure 6.20. There is still a mixture between power functions and polynomials for the trend lines, depending on which shape is considered to fit best. With the zero values gone, all trend lines values are considered to be more stable and accurately predicted by all the equations for each stress ratio.

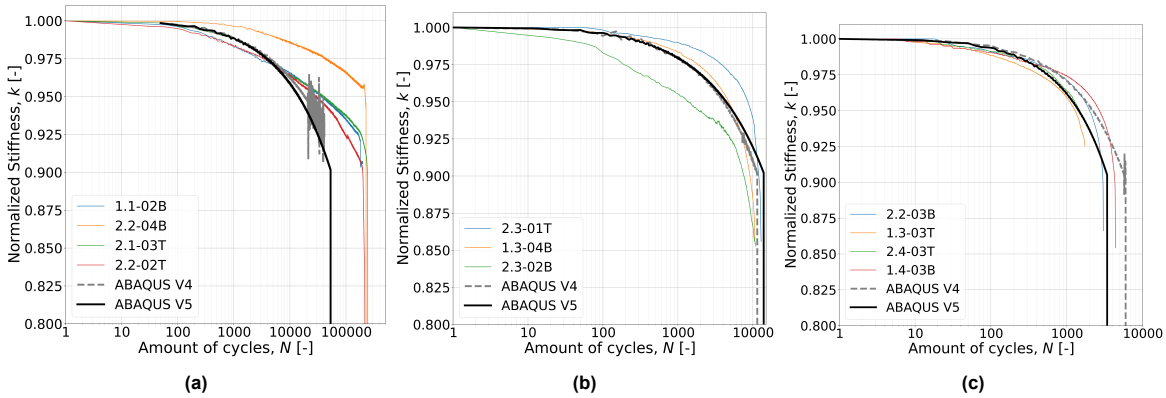

Figure 6.21: Results rational functions approach with non-zero values, stiffness degradation curves for load levels (a) 30 kN, (b) 50 kN and (c) 70 kN

The updated results are shown in Figure 6.21. It is immediately noticeable that the results for 30 kN are stable now due to the addition of non-zero values for c and d. The stiffness no longer oscillates due to incorrect values of the parameters, and the model continues to run until the failure limit of 90% stiffness remaining is reached. Since the 30 kN case does not stop prematurely, the amount of cycles has increased again as well. However, it is still underestimating the amount of cycles by a large factor

of approximately 4. This still needs to be improved by further iterations.

The other two load cases still show promising results. The 50 kN case now has a slight increase of cycles until failure, resulting in a slight overestimation. This will be taken into account for the next iteration as well. The 70 kN load case has significantly better results compared to the previous iteration. The slope of the stiffness degradation curve is now in line with the experimental results. On top of that, the amount of cycles until failure are also improved compared to the previous iteration. The fatigue life is now comparable with the average lifetime determined by the experiments.

6.5.5. Polynomial trend lines

The previous trend lines were a mixture of power functions and polynomials. For this new version, instead of using a mixture, only polynomial functions will be used. This choice is made because, at first sight, the power functions seemed a good fit. But after closer inspection, it was found that polynomials of second order provided better fitting trend lines.

To create these polynomial trend lines, the values of the parameters were slightly altered. The new values are shown in Table 6.9.

Table 6.9: New parameter values for damage fitting curves, polynomial

	30 kN	50 kN	70 kN
a	**0.0005**	0.005	**0.009**
b	$\mathbf{3.00 \cdot 10^{-8}}$	$\mathbf{2.00 \cdot 10^{-7}}$	$6.20 \cdot 10^{-7}$
c	**0.130**	**0.126**	0.122
d	$\mathbf{1.00 \cdot 10^{-10}}$	$\mathbf{2.50 \cdot 10^{-7}}$	$9.70 \cdot 10^{-7}$

The change in values of the parameters are relatively small since the previous fitting curves were already a good fit. The new fitting curves are shown in Figure 6.22

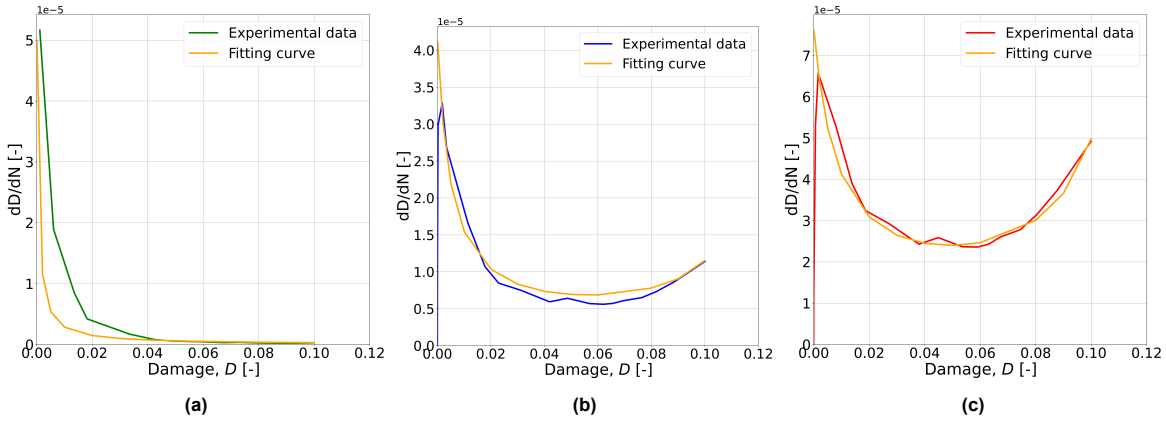

Figure 6.22: Damage per cycle vs. total damage incl. fitting curve based on rational functions with polynomial trend lines

The main change can be seen in Figure 6.22a. Since previously the fatigue life prediction for 30 kN was underestimated severely, it was attempted to decrease the damage per cycle to better fit against the experimental data. For 50 kN and 70 kN the fits are still parabola based and fitted as close as possible. Another reason for the altered parameter values in Table 6.9 was to create better fitting second order polynomial trend lines. The new trend lines are shown in Figure 6.23.

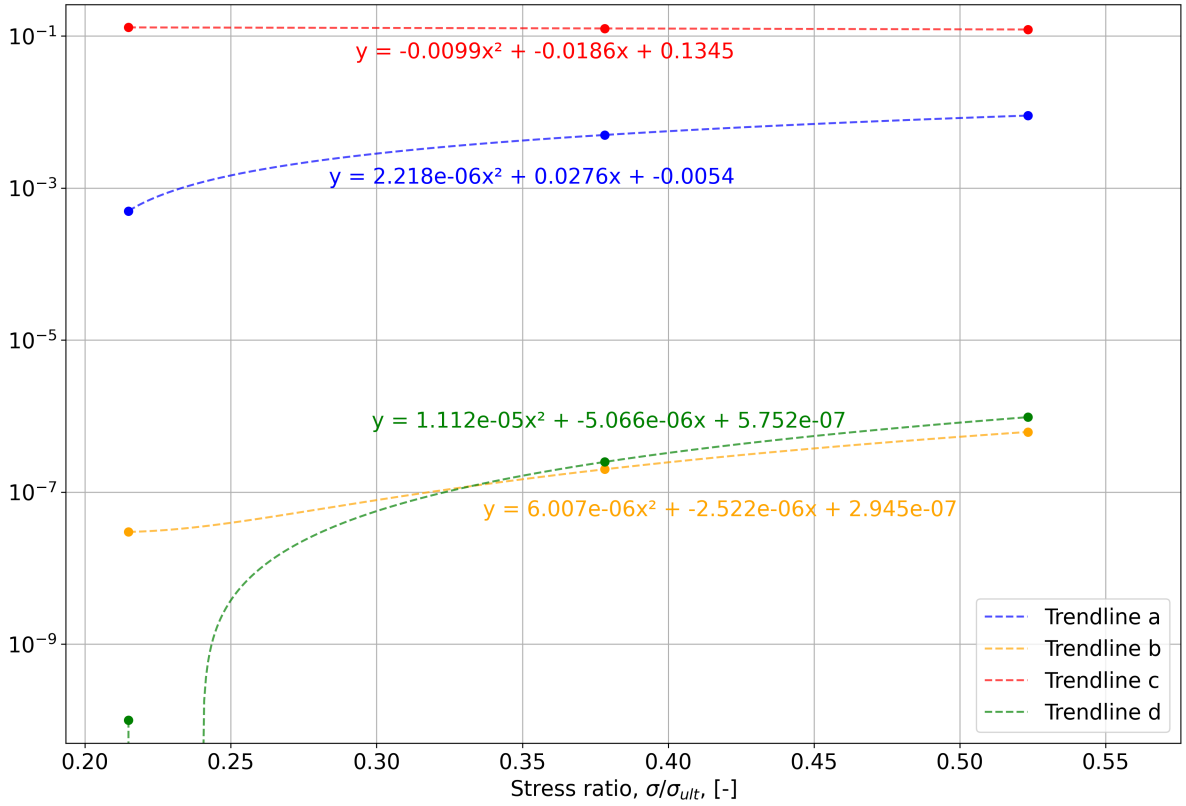

Figure 6.23: Trend lines for damage variables based on rational functions with polynomial trend lines, expressed in terms of stress ratio

All trend lines are now of a second order polynomial nature. Due to the logarithmic scale applied on the vertical axis, a weird phenomenon is appearing for the trend line of d. This is due to the fact that a small part of the trend line is in the negative domain. This is undesirable, so will be a point of attention in the next iteration. The results based on these trend lines is shown in Figure 6.24.

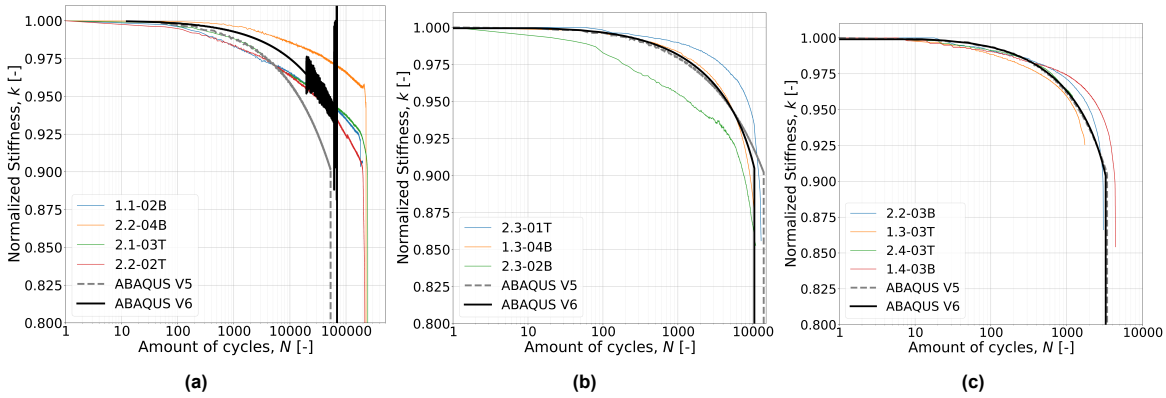

Figure 6.24: Results rational functions approach with polynomial trend lines, stiffness degradation curves for load levels (a) 30 kN, (b) 50 kN and (c) 70 kN

The results for both 50 kN and 70 kN are a very good estimation. The 50 kN load level estimation is no longer overestimating the fatigue life anymore, but now is again equal to the averaged fatigue life of the experimental data. The 70 kN load level is almost identical to the previous model, and still has the correct slope and fatigue life.

However, the same issue arises again for the 30 kN load level at which an unstable behavior is observed.

This can partially be traced back to the trend lines. As seen in Figure 6.23, there is a certain stress ratio region for which trend line d produces negative values. When the stress ratio is within this range, negative values will be introduced, which causes unstable results for the calculation of dD/dN. On top of that, due to stresses relocating to certain regions, the stress ratio, and related to that, the amount of damage per cycle, will severely increase in those regions. At the same time, other elements will experience very low stresses. This results in stress ratio's below what is now plotted in the graph of the trend lines. These new values will be extrapolated based on the equations that each trend line has.

The biggest problem with these extrapolations is the fact that not all functions of the trend lines are monotonic. Meaning that they not strictly increase or decrease. Instead, the trend lines showcase parabola shaped behavior. Towards the stress ratio of 30 kN, the lowest point is reached, but after this point an increase is taking place again. One of the consequences of this is that for super low stresses, for example near the clamped regions, high values for the parameters are calculated again. This sudden increase can result in large increases in the damage per cycle in those elements, thereby causing failure of the entire coupon in this region while realistically speaking this would not occur.

6.5.6. Monotonic functions

Since second order polynomial functions in general are never strictly monotonic, instead a different type of function will be applied for the trend lines. As was tried before for certain trend lines, power functions will be used. These are chosen because they are strictly monotonic increasing. Another benefit of using power functions, is the fact that they never go negative.

Table 6.10: New parameter values for damage fitting curves, monotonic

	30 kN	50 kN	70 kN
a	0.0005	0.005	0.009
b	$3.00 \cdot 10^{-8}$	$2.00 \cdot 10^{-7}$	$6.20 \cdot 10^{-7}$
c	0.130	0.126	0.122
d	$\mathbf{1.00 \cdot 10^{-9}}$	$2.50 \cdot 10^{-7}$	$9.70 \cdot 10^{-7}$

Only one value has changed in Table 6.10, this does not affect the fitting curves, but does help for creating a better fitting trend line for d. All trend lines are shown in Figure 6.25.

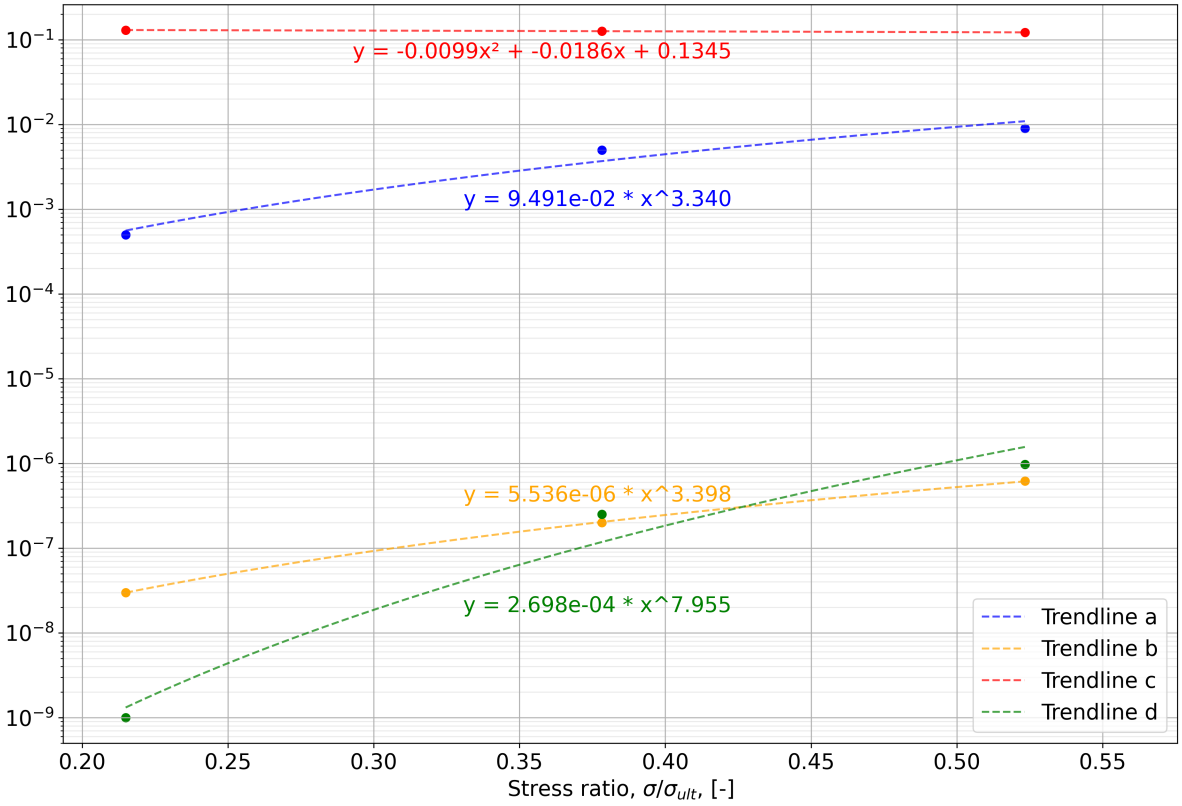

Figure 6.25: Trend lines for damage variables based on rational functions with monotonic trend lines, expressed in terms of stress ratio

All trend lines except for c are now converted to power functions. The choice was made to remain the trend line of c as a polynomial due to the decreasing nature. On top of that, even when extrapolating the line within the domain of [0,1], the function will remain monotonic since the line is almost linear. It does not appear that all lines are a power function, but this is due to the logarithmic scale on the vertical axis. However, it can be noticed that there are limitations to the accuracy of each point compared to the trend line. Trend line b is the only line crossing all three points. Managing this in all trend lines will be a point of attention in the next iteration.

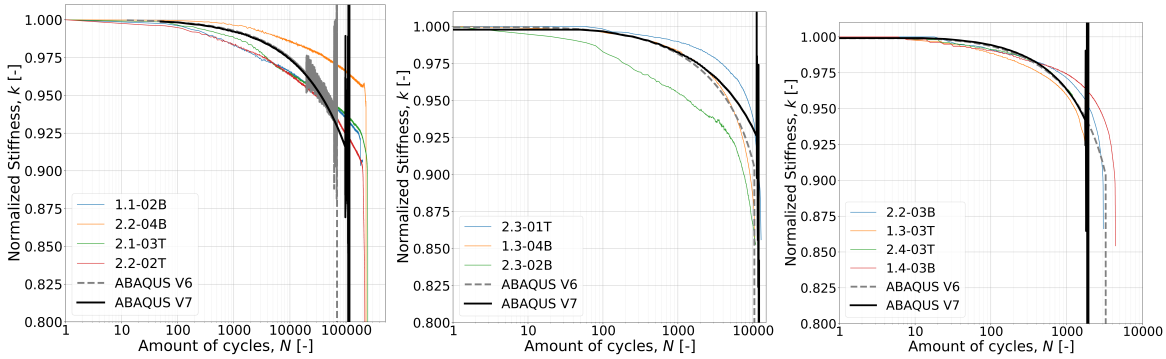

Figure 6.26: Results rational functions approach with monotonic trend lines, stiffness degradation curves for load levels (a) 30 kN, (b) 50 kN and (c) 70 kN

All results are shown in Figure 6.26, but what clearly can be seen is that now all load levels have severe unstable results at the final stages of the test. All unstable results and eventually failures occur well

before the failure limit. The only improvement with this approach is the improved fatigue life of the 30 kN load level. All other results are still relatively accurate, but are slightly worse than before. Looking at the location of failure, all coupons fail in the region of the clamps, at which low stresses should occur. However, the amount of damage and stresses here are relatively high. This problem needs to be tackled in the final version of the user subroutine.

6.5.7. Shifted power functions

The biggest problem with the previous iteration was the fact that the trend lines, which were mainly power functions, did not provide an accurate fit for all points. By overestimating certain values, the increase in damage per cycle was no longer stable, resulting in unstable stiffness degradation curves. To create more accurate trend lines, a method based on shifting power functions is applied.

The parameters that are used, are shown in Table 6.11.

Table 6.11: New parameter values for damage fitting curves, shifted

	30 kN	50 kN	70 kN
a	0.0005	**0.00325**	0.009
b	$3.00 \cdot 10^{-8}$	$2.00 \cdot 10^{-7}$	$6.20 \cdot 10^{-7}$
c	0.130	0.126	0.122
d	$1.00 \cdot 10^{-9}$	$2.50 \cdot 10^{-7}$	$9.70 \cdot 10^{-7}$

All power functions start at coordinate (0,0) and increase starting from there. However, due to this, it can be relatively difficult to create a fitting trend line that cuts through all 3 points. To still achieve this, the concept of a shifted power function is introduced. The inner workings of this concept will be explained in more detail below. The creation of the shifted power function for parameter d will be used to demonstrate the process of this method.

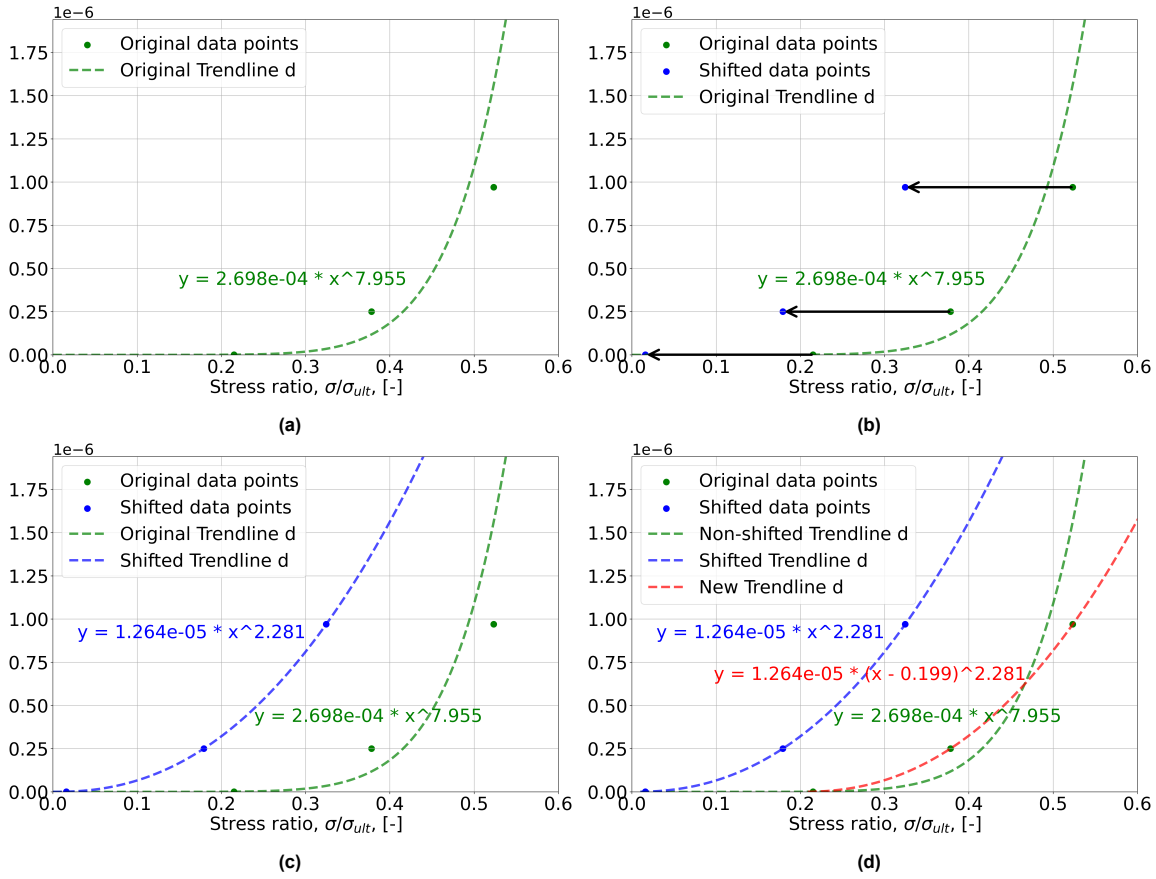

Figure 6.27: Process of shifting power function with (a) Original trend line d, (b) Shifted data points d, offset = 0,199, (c) Shifted trend line d, offset = 0,199 and (d) New trend line d

Figure 6.27a shows the original trend line d as used in the previous version with monotonic functions. When shifting from the logarithmic scale to normal distribution on the vertical axis, the deviation between the data points and the trend line becomes even better visible. To add to that, another negative aspect of the original trend line can be seen. After the last data point, located at a stress ratio of approximately 0,53, the line keeps increasing exponentially. Thus resulting in very large values of d in higher stress ranges. Ideally, you want this increase to be more gradual as well.

To achieve a better fitting trend line, the x-axis coordinates, representing the stress ratio, are offset towards the y-axis. This creates three new points, as shown in Figure 6.27b. Through these points, a new trend line, based on a power function, can be created. The offset is chosen such that the new power function trend line is intersecting all points as precisely as possible. It was found that the best result is occurring with an offset of 0,199. The resulting trend line is shown in Figure 6.27c. This also contains the new equation for the shifted trend line. The last step is to implement this new shifted trend line at the correct location. This is achieved by adding the offset in the equation for x (equal to the stress ratio). The end result of the shifted power function is shown in Figure 6.27d.

Before this equation can be implemented in the user subroutine, another restriction should be implemented. This is required because for stress ratio values below the offset value, an error will occur, this is because the value between the brackets will go negative). To counter this, a maximum function is implemented. This prevents negative values, but instead makes sure that in case of low stress ratios, the value of d will go to zero. The final equation implemented in the subroutine is given by equation 6.23.

$$y = 1.264 \cdot 10^{-5} \cdot \left(max \left(0,0; \frac{\sigma}{\sigma_{ult}} - d_{shift} \right) \right)^{2.281} \tag{6.23}$$

The same method of shifting the power function is applied on the trend line of a. This is shown in Figure

6.28. After investigating the other trend lines, it was found that those fitting lines were already a very accurate match. This results in the final trend lines as shown in Figure 6.29.

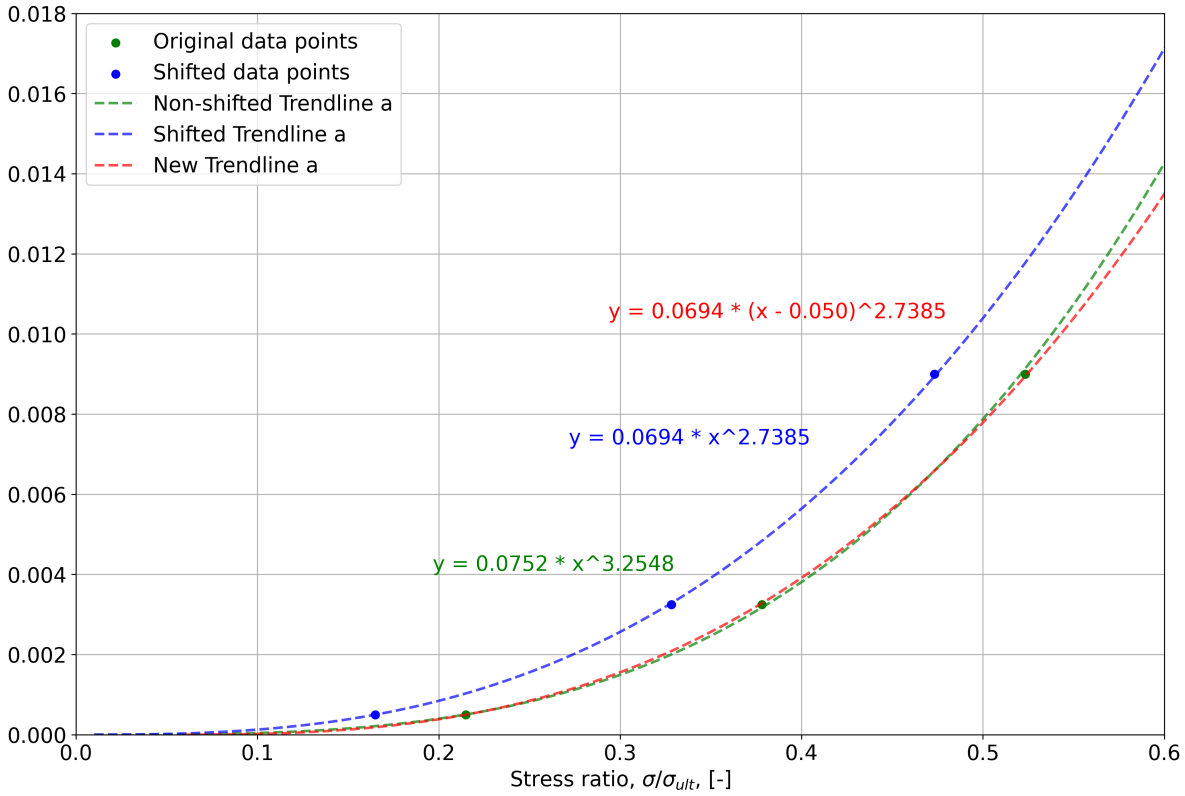

Figure 6.28: Shifted power trend line for a

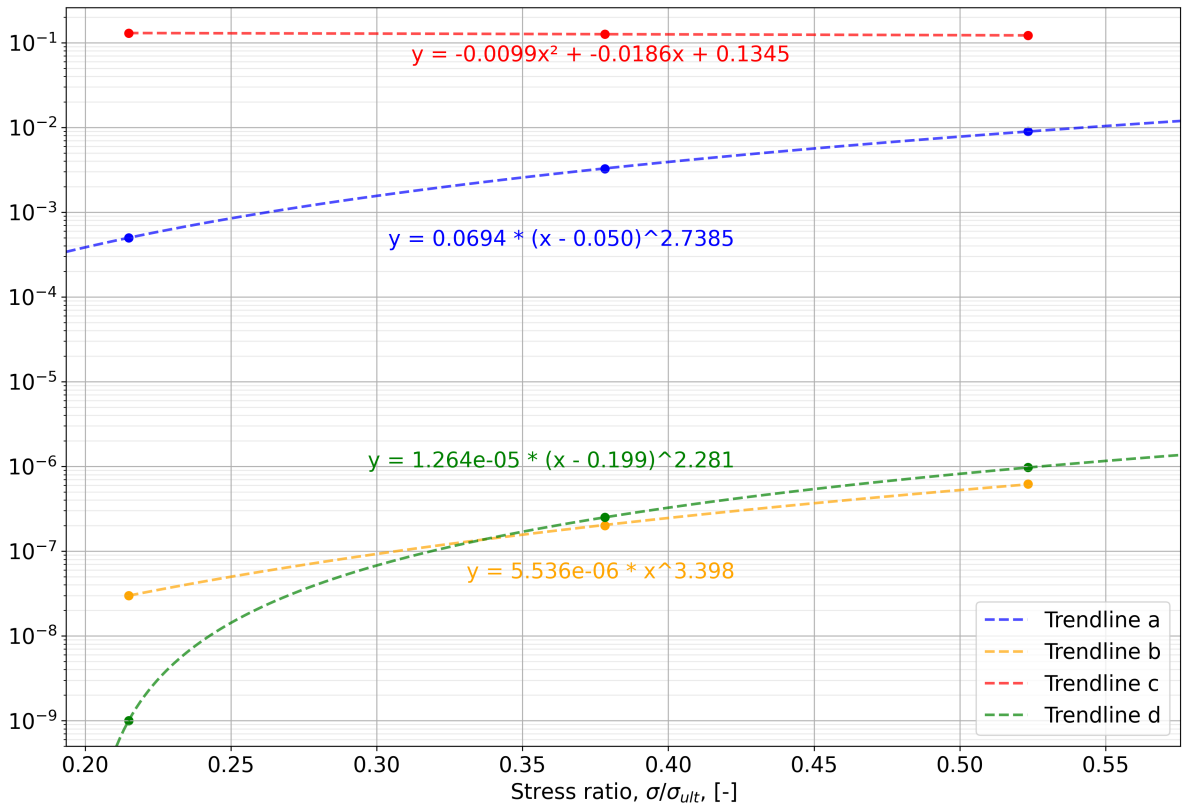

Figure 6.29: Trend lines for damage variables based on rational functions with shifter power trend lines, expressed in terms of stress ratio

A new numerical simulation could be performed with these new trend lines implemented in the user subroutine. These new results are shown in Figure 6.30.

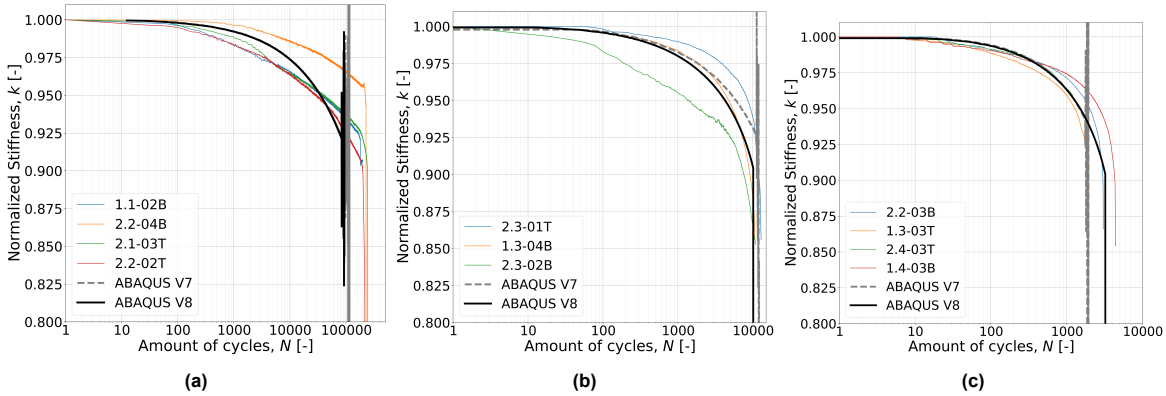

Figure 6.30: Results rational functions approach with shifter power trend lines, stiffness degradation curves for load levels (a) 30 kN, (b) 50 kN and (c) 70 kN

When comparing the results from the numerical model with the previous version, two key points need to be addressed. First is the stability of the results, related to the stiffness degradation curves. The previous user subroutine, solely based on the monotonic functions, showed large unstable results, failing before the stiffness limit was reached. The 30 kN load level simulation still shows this unstable behavior, but now it is slightly reduced and more brief. Unfortunately, this behavior still initiates before the failure limit is reached. In both other load levels, this unstable behavior is completely fixed. Looking at the slopes of each of the curves, they still follow the experimental data results for most of the load levels. A more detailed study into this instability for the low load level is provided in section 6.6.1.

The second key point is the amount of cycles until failure is reached. Load level 30 kN is slightly reduced again compared to the previous version, but both versions are still underestimating the cycles until failure by a large factor. The other load levels provide a more accurate prediction of the amount of cycles until failure. A full comparison for the amount of cycles until failure is provided in Table 6.12.

Table 6.12: Amount of cycles until failure, comparison of Experimental results vs. Numerical results

	30 kN	50 kN	70 kN
Experimental	229,564	11,492	3,010
Numerical	94,500	10,112	3,225
Deviation	- 59%	- 12%	+ 7%

Seeing that the above results are promising for most of the load levels, the decision was made to stop improving the damage model. All further results and comparisons will be based on the subroutine explained in this section 6.5.7.

6.6. Additional investigations

Until now, all research was focusing on the implementation of the damage model in the user subroutine for coupons without imperfections. Several other (short) studies have been performed as well to investigate certain use cases and parameters for the models.

6.6.1. Instability low load level

As was concluded in the final version of the user subroutine, the low load level of 30 kN shows instability as the model progresses towards the stiffness failure limit. In this section, the results are analyzed in more detail in an attempt to establish why this instability is occurring for this specific load case. Upon inspecting the data, it is found that the first unstable result occurs at time step 6794. This instability is visible in both the stiffness degradation curve, as with all the parameters used for the trend lines, affecting the damage implementation. Therefore, specific occurrences around this time step are investigated. First, a closer look was taken at the stresses in the coupon, since these are affecting the values of the parameters a till d. The stresses before and after the start of the instability are shown in Figure 6.31.

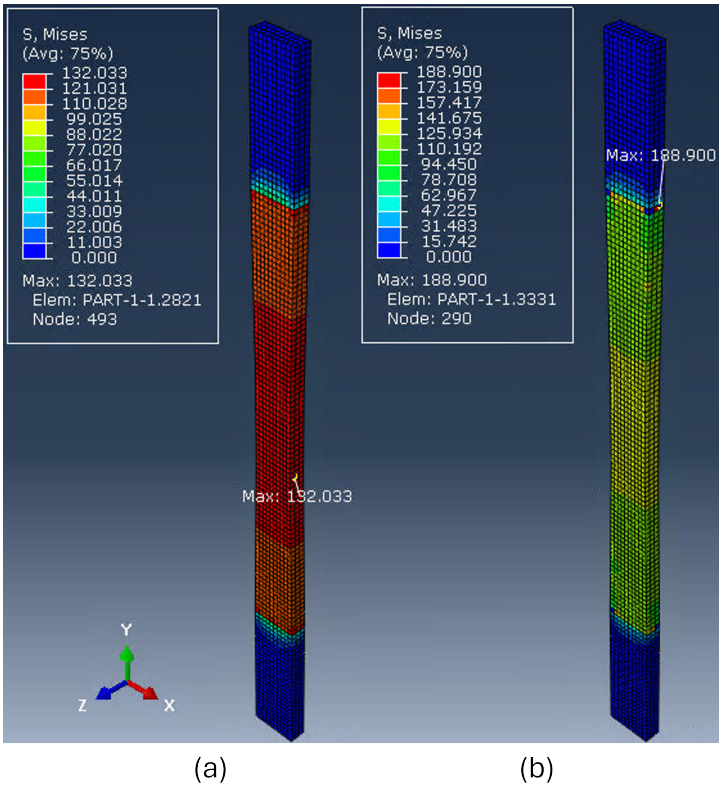

Figure 6.31: Maximum stress in coupon for (a) increment 6793 and (b) increment 6794

This immediately highlights where it appears to go wrong. There is a large increase of stresses near the region of the clamps. An increase in the stress is directly related to higher damage, resulting in more damage being applied locally. Therefore, the next step was to investigate the amount of accumulated damage to each element. From examining this damage throughout the coupon, it was found that the damage is consistently accumulating more near the clamped regions compared to the middle of the coupon. The final increments are shown in Figure 6.32.

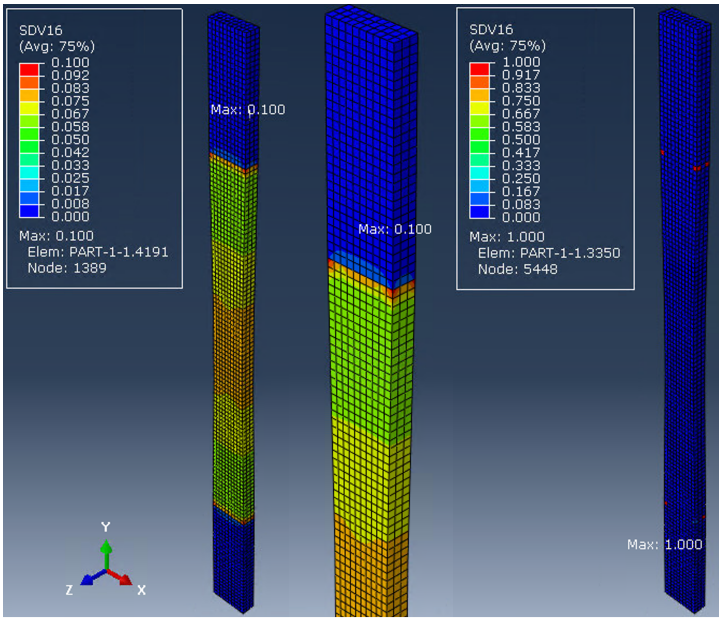

(a) (b) (c)

Figure 6.32: Accumulated damage in the coupon for (a) increment 6793, (b) upper half of the coupon and (c) increment 6794

The main issue is the corner elements that are attached near the kinematically constrained region for the clamps. These elements reach a damage level of 0.1, the threshold for stiffness failure, at increment 6794. This causes the rest of the results to be unstable, because it results in widely varying stresses within the rest of the coupon. That is due to the parameters being dependent on the stress ratio. The calculation still continues despite the damage being reached in several elements, until the entire top region is failed, causing large displacements that abort the entire analysis.

After inspecting the other load levels, the conclusion was that this behavior did not occur here, instead the stresses were highest in the middle, as was the damage accumulation. So the error had to be traced back to the 30 kN coupon model, which had an alternative model due to the thickness increase. Upon checking all boundary conditions and constraints etc., the only difference that was found was the mesh size. Instead of the element size of 4 mm, the 30 kN model had a mesh size of 3 mm instead.

By altering the mesh size of the 30 kN model, new results were found. The difference in damage accumulation per mesh size is shown in Figure 6.33.

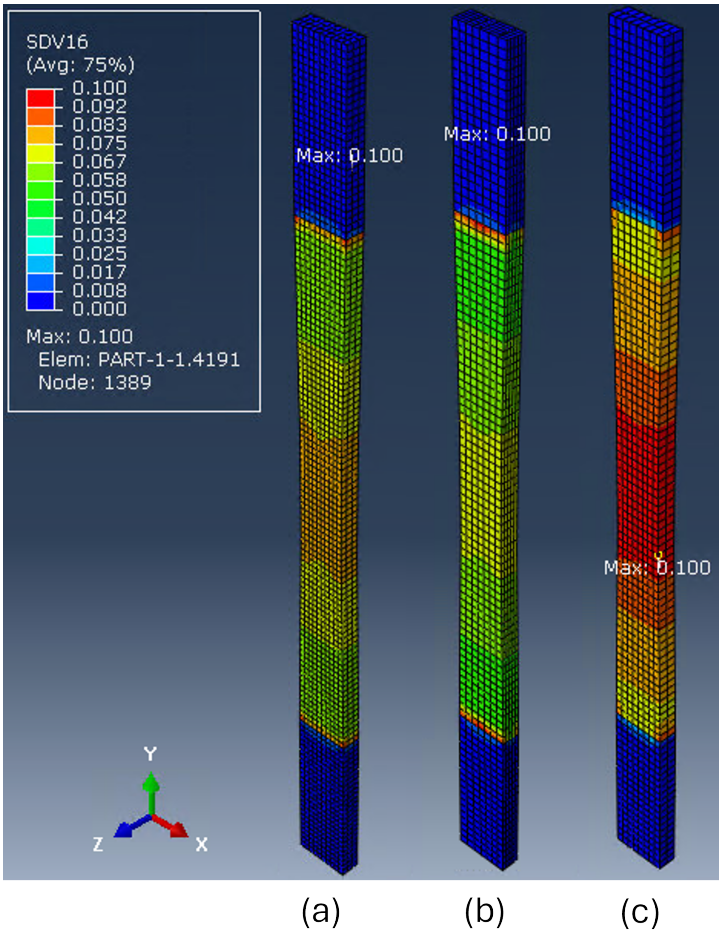

Figure 6.33: Difference in damage accumulation for mesh size (a) 3 mm, (b) 4-2 mm and (c) 4 mm

A total of three mesh sizes are shown. The first is the original model with a mesh size of 3 mm elements, showing the largest damage in the region near the clamps. The second model has 4 mm elements in x-direction, while having a mesh size of 2 mm in z-direction. The third model has 4 mm element sizes in all directions. A clear difference is present in terms of the amount of cycles until failure and instability starts to occur.

Table 6.13: Amount of cycles until failure

	3 mm	4-2 mm	4 mm
Amount of cycles	94,500*	66,600	123,350

* The instabillity already starts to occur at 83,650 cycles (increment 6794)

Furthermore, the amount of damage done in the middle region of the coupon is differing, this is mainly due to the amount of cycles that have been performed. It turns out that the best results are accomplished with a mesh size of 4 mm in all directions, just as was applied for the 50 kN and 70 kN load level. The following stiffness degradation curve is extracted from this model.

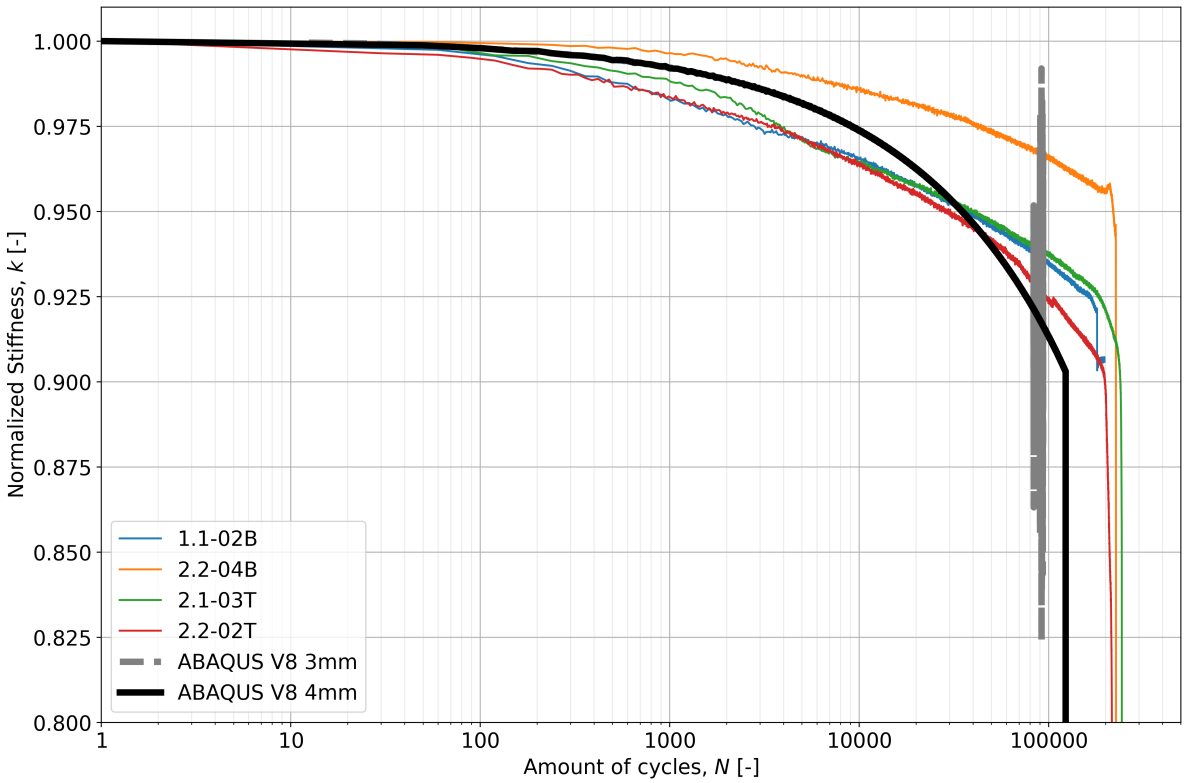

Figure 6.34: Stiffness degradation curve for load level 30 kN, comparing mesh sizes

When comparing the results from both models in Figure 6.34, it can be seen that the slope of the stiffness degradation is identical for both models. This is as one would expect since the measurements in both models are taken in the middle of the coupon, with exactly the same stress concentrations and damage applied. The major difference is in the stability of the calculation. Whereas the model with 3 mm mesh size starts to oscillate at approximately 83,650 cycles, the new model with 4 mm mesh size continues with stable results due to no failure in the clamped region. The fatigue life is extended by approximately 40,000 cycles. From this, it is found that the performance and instability for the lower load region is improved by altering the mesh size.

6.6.2. Imperfections

In this subsection, the effectiveness to apply this on coupons containing geometrical imperfections in the numerical model will be investigated. The whole subroutine is set up according to experimental results from coupons without imperfections. However, experiments have also been performed on coupons containing imperfections. As a method to test the numerical model, a coupon that contains a geometrical imperfection will be modeled and subjected to the user subroutine. This imperfection creates different stress concentrations inside the material. Since the fundamental structure of the model is stress governed, due to this changing stress concentrations, the amount of damage done at these regions should be affected.

As a geometrical imperfection, a dimple is modeled in the middle part of the coupon. All dimensions and depth of the dimples were measured beforehand. The average dimple depth measured was 0.50 mm. That is why the depth in the model is also chosen to be 0.50 mm in depth, and round shaped. A clear side-view of the dimple in the model is shown in Figure 6.35a. Surrounding the geometrical imperfection, a more dense mesh size is chosen to account for irregularities in the model for the stresses and displacements. The mesh size in the 25 mm surrounding the dimple is altered from 10 mm to 1.25 mm instead, this is a factor of 8 more dense. This new mesh is shown in Figure 6.35b.

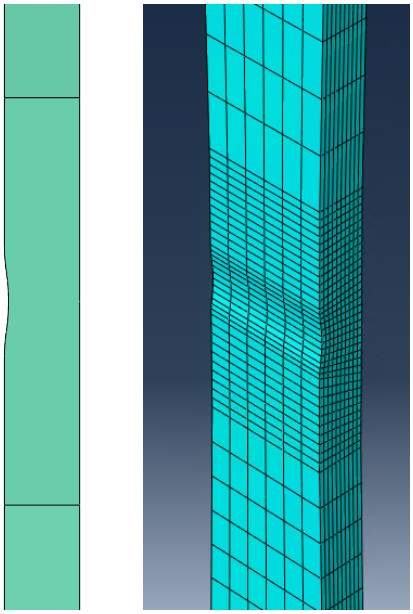

Figure 6.35: Geometrical imperfection of the coupon, shown by (a) side view of the dimple and (b) the mesh size at the dimple

All settings from the subroutine remain the same as for the model without an imperfection. The results are shown in Figure 6.36.

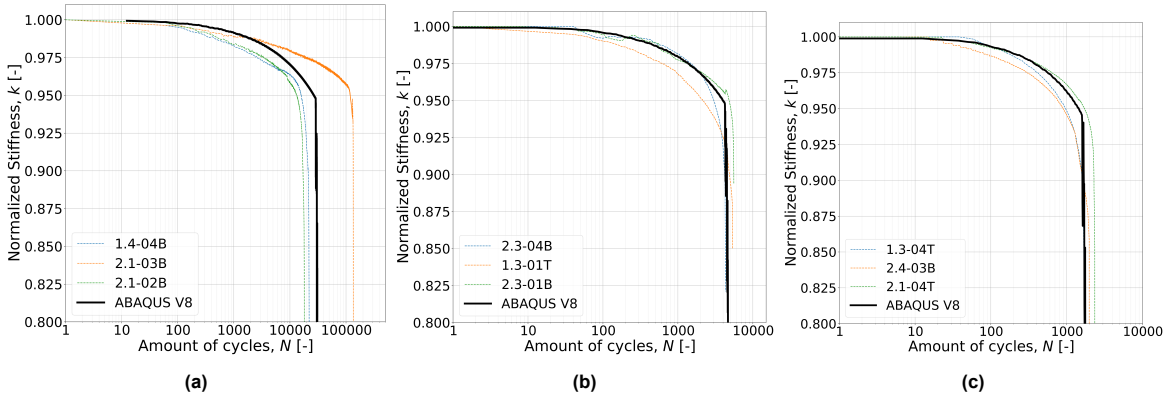

Figure 6.36: Results imperfections stiffness degradation curves for load levels (a) 30 kN (b) 50 kN (c) 70 kN

By implementing the imperfections, the model provides completely new results. The moment of failure in terms of the amount of cycles and the stiffness at failure are differing from the results in Figure 6.30. Comparing the results from Abaqus with the experimental data, a clear overlap is visible. Especially the stiffness at failure is very accurate. All simulations fail at approximately 0.95 of the normalized stiffness remaining. This is in line with the results in the lab. This is encouraging since no new limit was defined in the subroutine.

Looking at the moment of failure in terms of cycles. The largest deviation is occurring at 30 kN, with an estimated fatigue life of approximately 29,000 cycles. As mentioned in section 5.5.1 there were two types of imperfections for the 30 kN load level. Comparing the fatigue life with the two coupons that had a dimple as well, there is an overestimation of approximately 8,000 cycles. For the 50 kN load level, the difference is already much smaller. The model has an estimated fatigue life of approximately 4,500 cycles, compared to approximately 5,050 cycles during experiments. The last load level of 70 kN has an estimated fatigue life of 1,700 cycles. This is relatively comparable with the tested coupons, which failed at approximately 2,000 cycles. Based on these results, it can be concluded that there is still room for improvements of the damage model, but that the initial results look very promising. A suggested solution for improving the imperfections will be discussed in section 6.6.5.

6.6.3. Influence cycle jump factor

The basic principle of the variable 'dN_fix', also known as the cycle jump factor, is briefly described in section 6.4.1. This section dives deeper into if there is an influence on the results by adjusting this jump factor or not. To test the influence, three simulations will be run on the same model, after which the results will be compared. The standard coupon numerical model is used, for the load level of 50 kN. The final version of the user subroutine, discussed in section 6.5.7, is used. The values for 'dN_fix' that are used are 0.02, 0.20 and 2.00. For extra reference, the results from the final calculation, explained in section 6.5.7 will also be included. The value used here is 0.05.

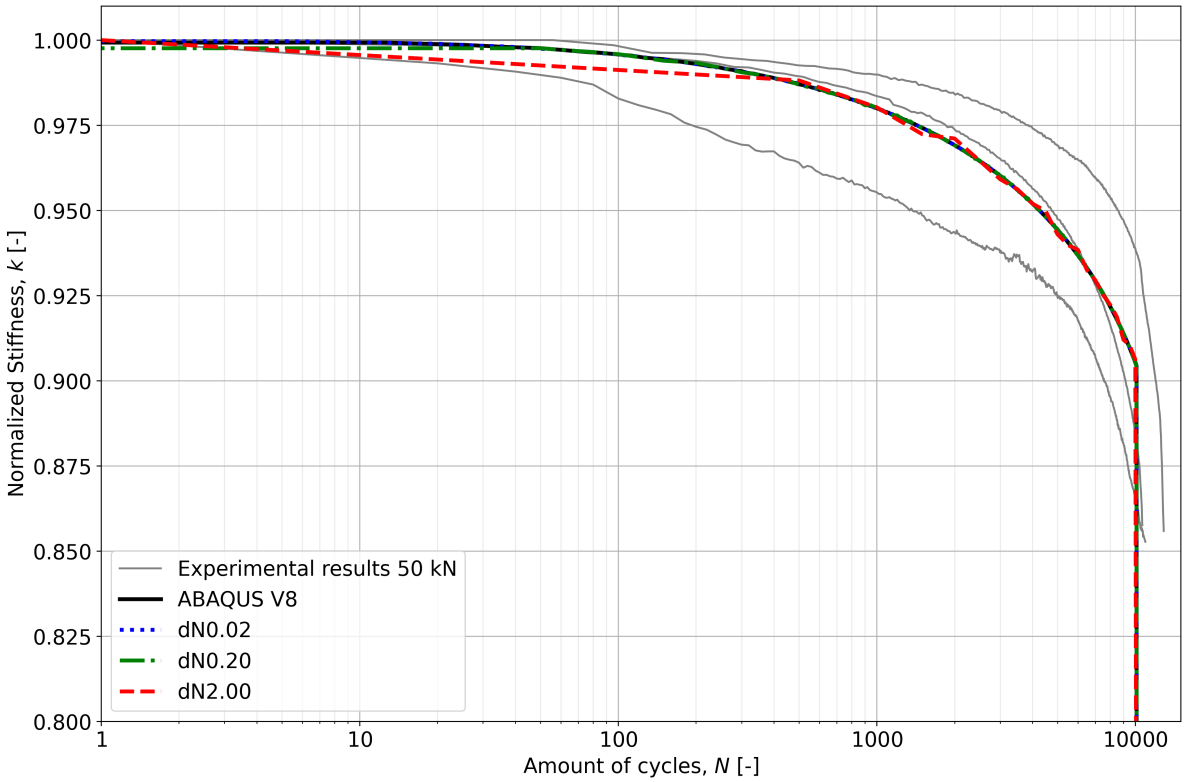

Figure 6.37: Influence of cycle jump factor shown on stiffness degradation curves

All results are shown in Figure 6.37. However, since almost all results are identical, the small differences are hard to see. The biggest difference is in terms of how fluent the curve is. This is due to the different amount of interval data points that each calculation has. A short comparison is provided in Table 6.14.

Table 6.14: Comparison between different cycle jump factors

dN_fix	0.02	0.05	0.20	2.00
Cycles until failure	10125	10125	10150	10500
Amount of data points	2025	809	203	21
Computational time [s]	375	138	71	37

Based on the above numbers, it becomes clear that there in fact is an influence of the results based on the cycle jump factor. Looking at the amount of cycles until failure, a difference can be seen at increased values. However, the reason behind this is not strictly because of the cycle jump factor. This difference can partially be traced back to the calculation settings in Abaqus itself. For all calculations, a stable time increment of 0.004 is set. This means that for every second of the calculation, 250 increments are performed. The amount of cycles that this increment represents, is based on the cycle jump factor. So for a factor of 0.02, each second only represents 5 cycles, while for a factor 2.00, the same second

represents 500 cycles. Since in all calculations, the setting was set to store all information per second, this causes the large difference in cycles until failure for the 2.00 cycle jump factor. The actual failure most likely occurs at approximately 1025 cycles as well, but it is stored in intervals of 500 cycles.

This is also the main reason for the difference in amount of data points and computational time. Due to the low amount of cycles performed per second. A large increase in amount of seconds is required until failure. This directly influences the amount of data points stored, and in addition to that also a large increase in computational time. Based on all this information, it can be concluded that in fact there is an influence by adjusting the cycle jump factor. For more accurate results, it is important to take into account the value for the cycle jump factor that is chosen. For all studies, a cycle jump factor of 0.05 has been chosen since this balances between providing accurate results, while also having a relatively low computational time.

6.6.4. Mesh sensitivity analysis

To get more insights in the influence of the mesh size on the output of the model, a mesh sensitivity analysis was performed. The main focus was to see the influence on the stresses in the coupon and the stiffness that the coupon exhibits. A total of four different mesh sizes are evaluated. The ranges evaluated are 2 mm, 3 mm, 4 mm and 4 mm in x-direction (width) while having 2 mm in z-direction (thickness). All models are subjected to a tensile test where a force of 200 kN is applied in longitudinal direction. First, a closer look is taken at the location of the maximum stress at a tensile load of 200 kN. The results are shown in Figure 6.38.

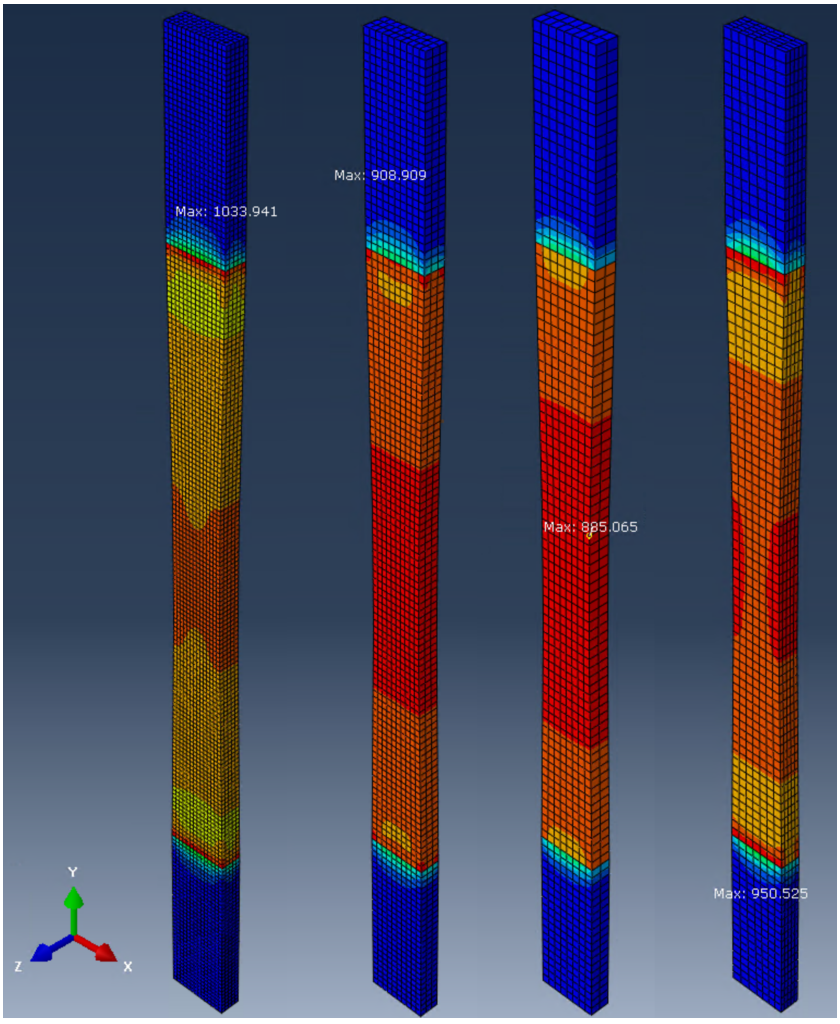

Figure 6.38: Mesh comparison, showing maximum stress at 200 kN load for mesh size of (a) 2 mm, (b) 3 mm, (c) 4 mm and (d) 4-2 mm

The first obvious difference is that the location of the maximum stress is different for smaller mesh sizes. Whereas the maximum stress for the 4 mm mesh size is in the middle of the coupon, all other maximum stresses are located at the interface between the clamped region and the coupon. This coincides with the results that were found when looking into the instability at low load levels as described in section 6.6.1. When inspecting the stresses in the middle of the coupon at 136.5 kN, which is near the estimated ULS of the material, the results shown in Table 6.15 are found.

Table 6.15: Stress at middle of the coupon at 136.5 kN for different mesh sizes

Mesh size	2 mm	3 mm	4 mm	4-2 mm
Stress [MPa]	591.95	591.73	591.95	591.58

Unlike near the clamped region, the stresses in the middle of the coupon are nearly identical. These values are also corresponding with the results gained from static tests provided in Table 4.2. Besides the stresses, also a comparison between the different stiffness values is performed, based on a Load - Displacement diagram. The results are shown in Figure 6.39.

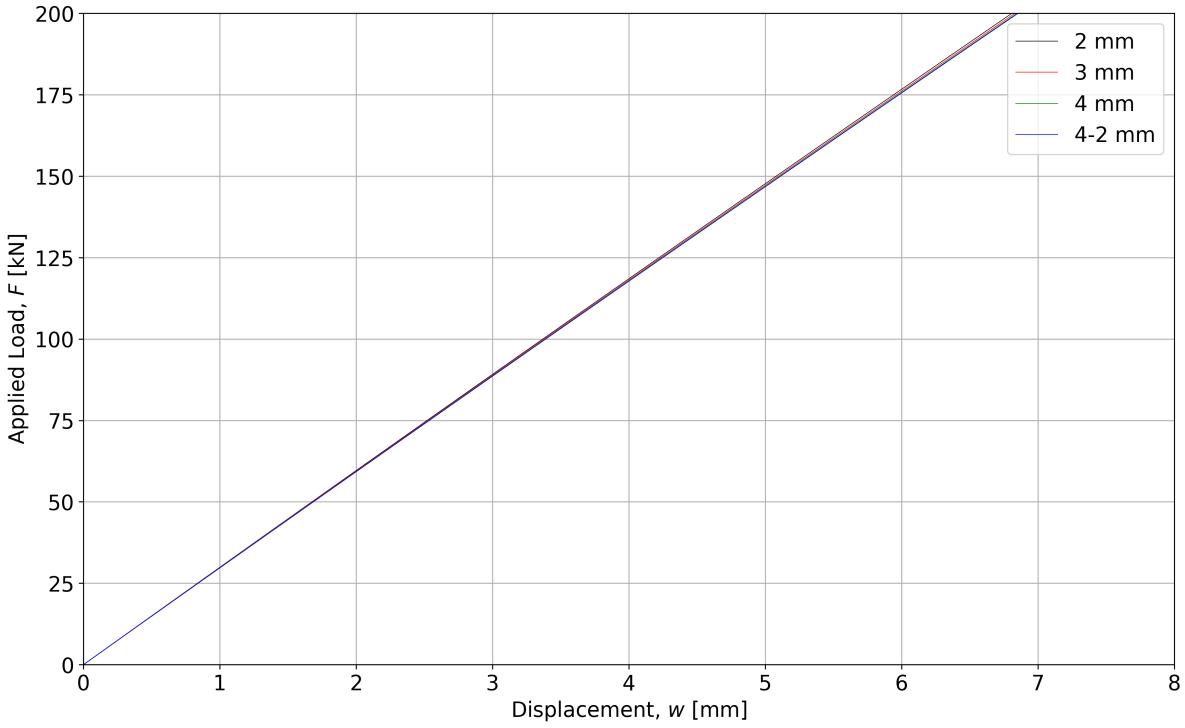

Figure 6.39: Load - Displacement diagram from FEA, showing all four mesh sizes

Looking at the slopes and applied load over the displacement, again, all results are nearly identical. Due to being so similar, most lines are less visible. Based on this information, and the results from the stresses in the middle and clamped region. The 4 mm mesh size was pursued for all numerical models. An additional benefit of choosing this mesh size over a more dense mesh is the favorable computational time. The amount of elements and integration points that need to be calculated reduces, resulting in a lower computational time.

6.6.5. Validation

This section contains several validation studies. First, an attempt to extrapolate a different load level is investigated. Secondly, experimental results are compared with numerical results based on the S-N curves, and lastly the initial stiffness degradation input is investigated versus the output.

New load level, 25 kN

To see if the model also works for load levels outside the range that is defined in the code and was sufficiently tested in the lab, one test simulation is performed on the load level of 25 kN. The trend lines are all based on points within the range of 30 kN till 70 kN. Therefore, this simulation is testing if extrapolation is working as intended. A single coupon was tested on the 25 kN load level, this can be used as reference material for the comparison. The result from the numerical model is shown in Figure 6.40.

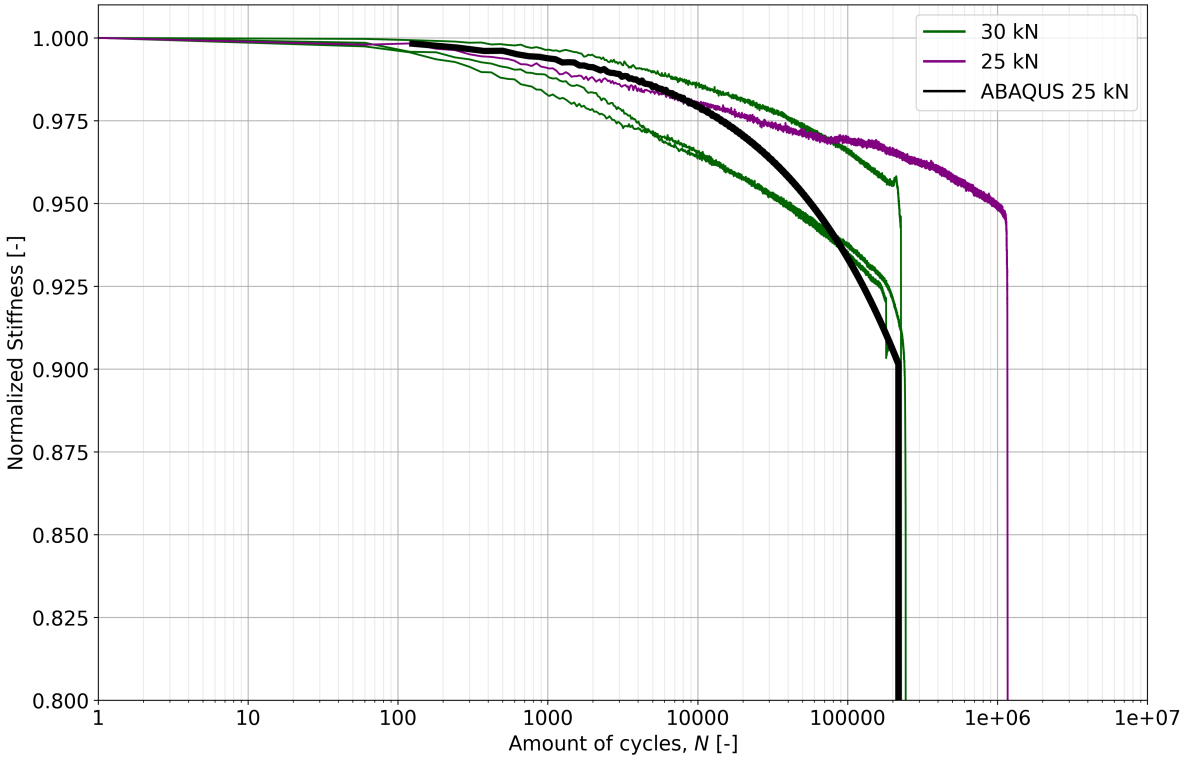

Figure 6.40: Results for load level 25 kN simulation expressed in stiffness degradation curve

It turns out that the numerical model is underestimating the amount of cycles by a large factor of five. The model runs for approximately 220,000 cycles, whereas the experiment ran for 1,150,000 cycles. This confirms what was already noticed regarding the underestimation of the amount of cycles on the lower load levels.

In addition to this, the normalized stiffness failure limit is also lower compared to the coupon test. This can be explained based on the way that the failure limit is currently defined. For all three load levels (30 kN, 50 kN, 70 kn), the stiffness at failure is considered at 90% of the normalized original stiffness. As explained in section 6.3.2, this was done for simplification reasons. This limit is expressed by the parameter $D.th$, which is set to 0.1. As previously discussed in section 5.4.1, the actual threshold at which the coupons failed for each load level is slightly deviating. The trend it follows can be defined as a slowly decreasing as the force decreases as well. A rough indication of this behavior is shown in Figure 6.41.

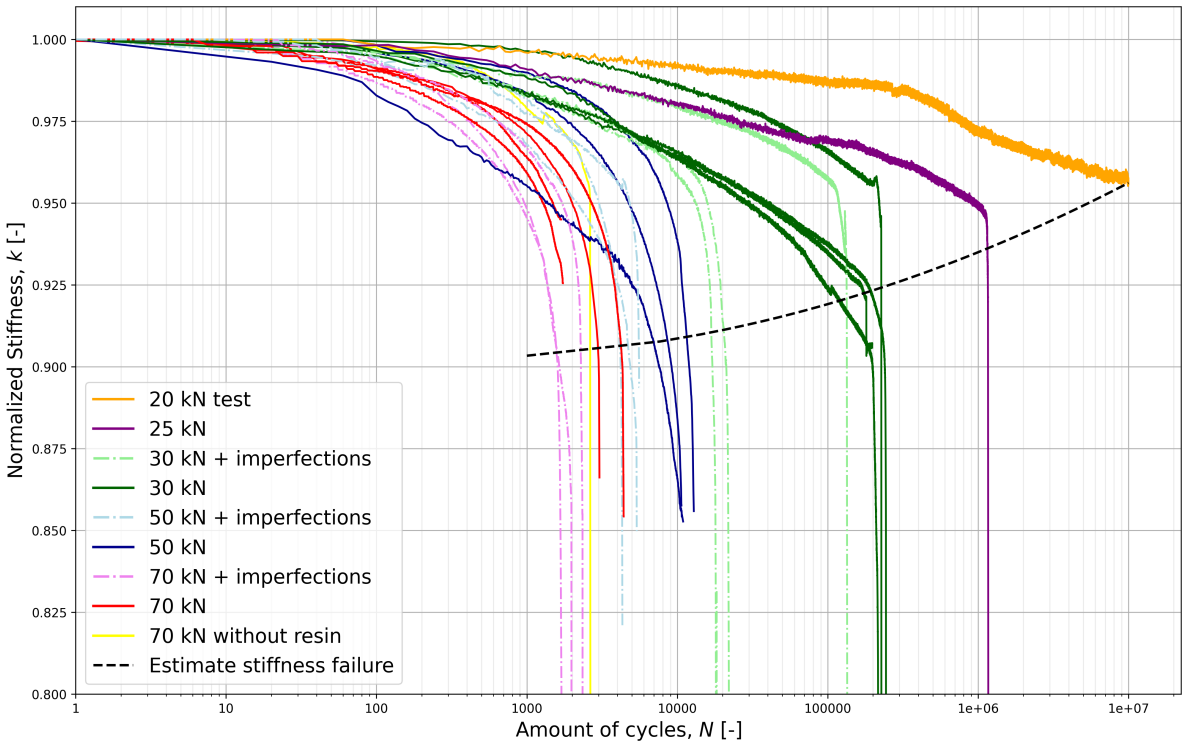

Figure 6.41: Normalized stiffness degradation curve with failure trend line

To get an even better prediction of the failure limit at other load levels, it would be advisable to perform additional tests. Currently, the high amount of cycles results (25 kN and 20 kN) is only based on one test each. However, based on the estimation of the behavior, a non-linear trend can be seen. Therefore, one could argue to define this parameter $D.th$ as a variable as well, with the help of a trend line. There are multiple possibilities for the type of trend line, such as polynomial function.

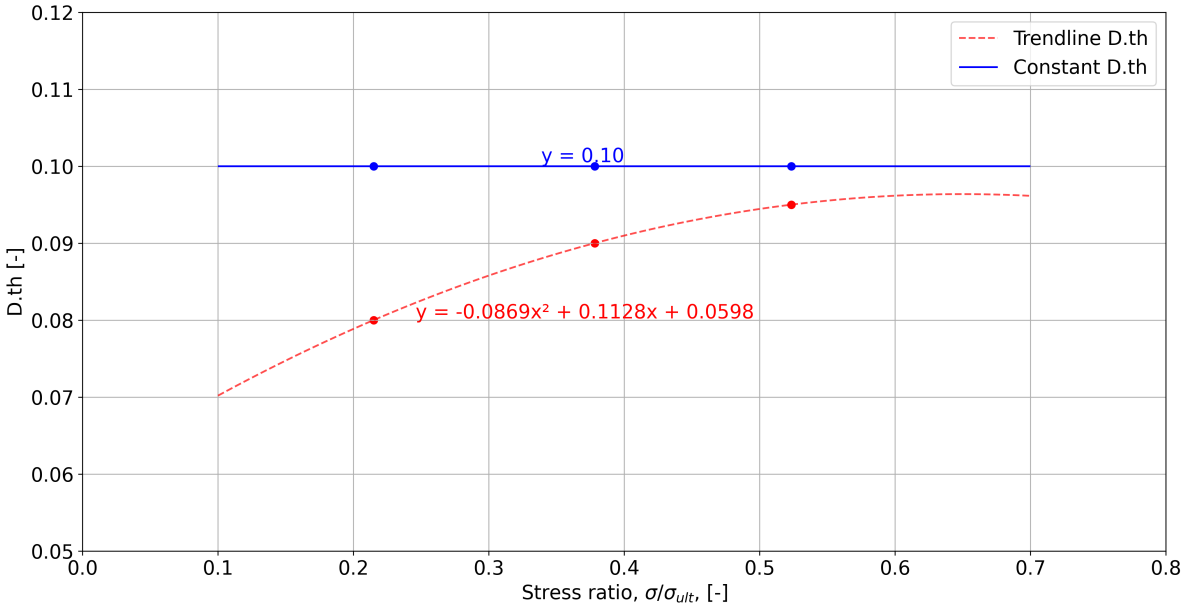

Figure 6.42: Trend line for variable D.th

Figure 6.42 shows the current implementation as a constant, and a possible second order polynomial for

a more accurate representation of the failure limit. Setting $D.th$ as a variable is not actually implemented in the code, but is a suggestion for follow-up research to add as a fifth trend line.

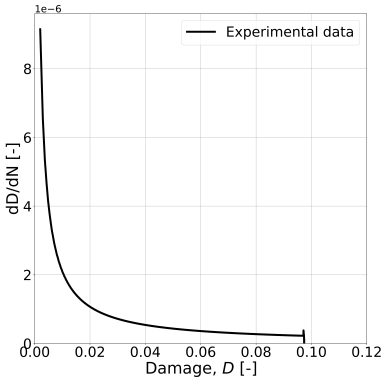

Figure 6.43: Damage per cycle vs. total damage for load level 25 kN

Looking at the damage increase that is exerted as damage progresses (Figure 6.43), the behavior looks almost identical to the fitting curve of 30 kN as shown in Figure 6.22a. This confirms that the method for suppressing the second rational function for low load levels is still effective when extrapolating load levels below 30 kN.

Stress-life curves FEM

In section 5.4.2 the S-N curves from the experimental fatigue tests were discussed. In addition to this, the results from the numerical model simulations are included in Figure 6.44. This comparison is based on the S-N curves from figure 5.12b, that considers the imperfection outlier as a coupon without imperfections.

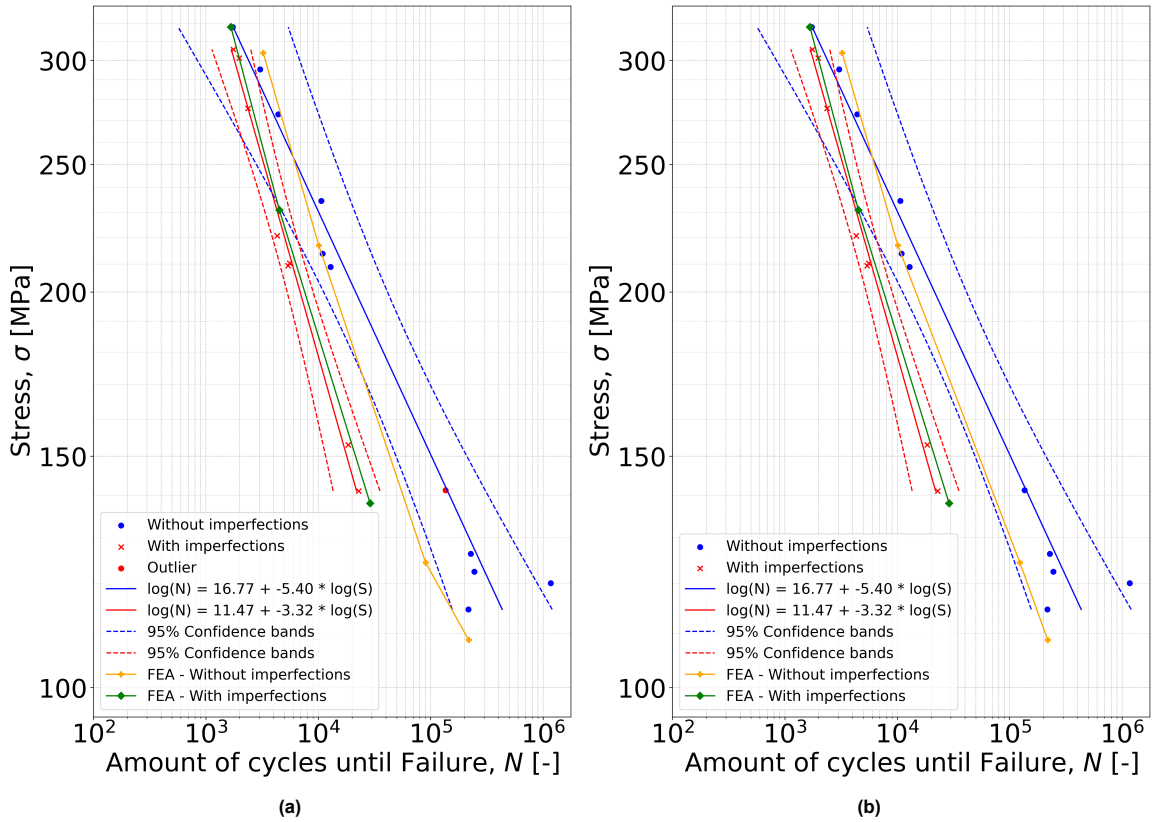

Figure 6.44: S-N curves including FEM results for mesh size (a) 3 mm and (b) 4 mm

The figure contains two sub figures with different S-N curves, Figure 6.44a is based on the Finite Element Model (FEM) results including the fatigue life of the 30 kN load found in section 6.5.7. This is the initial result that includes the instability due to the mesh size of 3 mm, as discussed in section 6.6.1. The second Figure 6.44b includes the stable results that have been found by increasing the mesh size to 4 mm.

Based on the S-N curve for the FEM without imperfections, a recurring finding is again confirmed for the FEM. For higher stresses, the results are very much in line with the scattering of results from the experiments. At lower stress ranges, the FEM result starts to deviate from the experimental results. Taking into account the initial 3 mm mesh size result, the FEM result is underestimating the fatigue life such that it is even outside the region described by the confidence bands. However, it should be noted that the performance is already improving with the S-N curve shown in Figure 6.44b, using the result from the 4 mm mesh size model. The result from this model is within the confidence bands. Comparing both S-N curves for coupons without imperfections highlights a steeper slope for the FEM. This highlights the fact that the model is less sensitive to stress changes. As a result, the FE model is accurate in the higher stress ranges while underestimating the performance in lower stress ranges.

Looking at the FEM results of coupons with geometrical imperfections, the results appear to be more consistent with the experimental results. Each of the stress levels is very representative and lies within the confidence bands region. As for the S-N curve slope, this is almost identical to the experimental S-N curve. This indicates that the model sensitivity to stress changes is in line with experimental results. There is a slight deviation in the performance. The S-N curve is shifted rightwards, indicating that the numerical model actually overestimates the fatigue performance of the material slightly. For now this level of accuracy is considered sufficient, but this can be improved in follow-up research.

Currently, the imperfections are only modeled as geometrical imperfections. What is not considered is the fact that due to the dimple, the fibre volume fraction will change locally as well. In the coupons tested, originated from the facings, the V_f is 54%. At the locations of the dimples, the same amount of fibres is present. However, the amount of resin is decreased. This results in a higher fibre volume fraction percentage. Current studies investigating the influence of the fibre volume fraction on the fatigue performance all conclude that as the V_f increases above 55-60%, the fatigue performance will decrease [23][2][10]. Since in these coupons from the facings the V_f is already near this limit, taking this increase into account will most likely result in a small decrease of fatigue life. Therefore, for an updated version of the numerical model, one could consider changing the material properties based on new fibre volume fractions present locally at the dimple.

Initial vs. final fitting curves

The initial stiffness degradation curves that eventually were used for recreating the damage behavior in the numerical models, were based on ellipse fitting curves as shown in Figure 6.5. In order to extract the final results, multiple fitting curves based on other fitting curves have been used. In this section, a comparison will be performed to see if/how the initial fitting curve differs from the final results. Both stiffness degradation curves for each load level are shown in Figure 6.45.

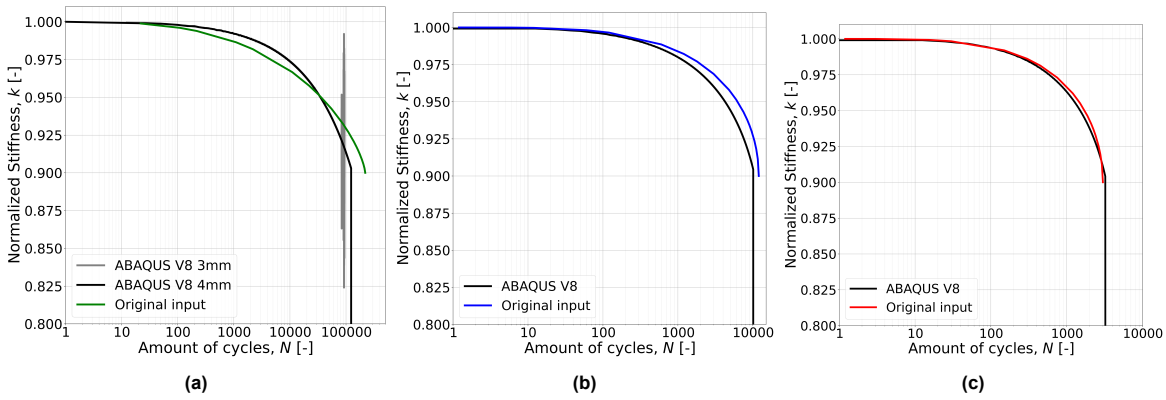

Figure 6.45: Comparison of initial vs. final fitting curves for stiffness degradation for load levels (a) 30 kN with 3 mm and 4 mm mesh size, (b) 50 kN and (c) 70 kN

The largest difference is present in the lowest load level of 30 kN (shown in Figure 6.45a). The slope of the degradation curve is slightly deviating from the initial slope, in this case it starts more gradually but ends up declining quickly. This relates to the underestimated fatigue life that the model exhibits at lower load levels. Note that the figure shows two lines, both the resulting degradation curve of the 3 and 4 mm variant. The 4 mm result is included since the 3 mm result was terminated earlier due to instability issues as mentioned in section 6.6.1. Looking at the other two load levels and their respective fitting curves, the fitting lines are almost identical. The largest difference is in the fact that the amount of cycles is not entirely correct. This can be traced back to the number of cycles that was set for the first fitting curve. In both cases, this is not set at the averaged number of cycles. The result from the numerical model are actually more in line with the averaged results from the experimental data. Therefore, there might be an improvement possible by creating new fitting curves for the experimental stiffness degradation curves, but this will likely only result in a small benefit.

7

Conclusions and recommendations

7.1. Conclusion

The main question to be answered during this Master's thesis was:

- How can fatigue in multidirectional composite laminates be modeled at the coupon level using computational methods?

By using the experimental results from Chapter 4 and Chapter 5 as input for the model, a fatigue model was developed to predict the fatigue life of multidirectional laminate. This was done by means of a FEA, performed in Abaqus. This problem was addressed by answering multiple sub-questions:

- What is the degradation behavior of multidirectional composite laminates at varying load levels?

According to the experimental study in Chapter 5, it is found that there is an effect of the load on the degradation behavior on fatigue. Three load levels, ranging from low (22% of ULS), to mid (37% of ULS), to high (50% of ULS) loads, were tested. At 22% of ULS the stiffness degradation drop until failure is found to be 8% while at 50% of ULS this has increased to 9%. Besides the increase in stiffness drop, the fatigue life was severely reduced from 230,000 cycles at low load to 3,000 cycles at high load.

- What role do geometrical imperfections play on the fatigue life of multidirectional laminate on coupon level?

Based on an experimental study, performed in Chapters 4 and Chapter 5, it was found that imperfections mainly play a role in dynamic tests. Depending on the load level, deviating influence of imperfections are found. At 22% of ULS, the fatigue life is reduced by a factor of 11.1, while at 50% of the ULS, this reduction is only a factor 1.5. As for static tests, the influence on the tensile strength was negligible.

- How can the degradation behavior of a coupon be modelled in Abaqus?

A numerical model is developed in Abaqus, which integrates a VUSDFLD user subroutine. The user subroutine implements a Continuum Damage Mechanics (CDM) model that describes the material damage accumulation over time, reducing the material stiffness properties as a function of the stress levels in each element. Based on the final results, it is concluded that the fatigue life estimation is most accurate for higher load levels. Estimations from the model are within 10% of the experimental results. Meanwhile, the lower levels are underestimated by approximately 85%.These findings are further addressed in Chapter 6

Despite this limitation for lower load levels, the model successfully predicts the impact of local imperfections on fatigue life performance. By simply modeling geometrical imperfections, causing high local stress concentrations, the model was able to predict the fatigue life, and also the overall stiffness degradation slope accurately. These findings contribute to understanding the fatigue performance of composite structures and highlight the influence that imperfections have on fatigue life, especially under lower load conditions.

7.2. Limitations

Despite the positive results, the model and method chosen still hold several limitations that should be taken into account. The biggest limitation of the model currently is the underestimation of the fatigue life for lower load levels without imperfections. The results from simulations for 30 kN and lower all result in underestimations. In the range between 30 kN and 50 kN, no simulations have been verified since no experimental results for those load levels were available.

An additional limitation of the model that should be taken into account is regarding the stiffness failure limit. During experimental testing, it was found that the stiffness failure limit is slightly deviating per load level. As the load level increases, a slight increase in the limit is noticed. For simplification reasons, however, this stiffness failure limit is currently set at a default value of 10% of stiffness degradation for all load levels.

Regarding the geometry of the coupons in the FE model, two assumptions have been made. The first assumption regarding the model without imperfections is that this coupon is considered to be perfect dimension and material property wise. In reality, the coupons tested have small geometrical deviations in thicknesses and widths, and possible internal material property irregularities. The second assumption is regarding the coupons with imperfections. The model now assumes that all dimples have a depth of 0.50 mm in combination with being located in the middle of the coupon. The depth is based on the average dimple depth, but did slightly deviate in the samples tested. In addition to this, the imperfection in the model is located in the middle of the coupon, whereas the exact location of the imperfection in the coupon was not always located in the middle. This affects the results because the damage calculation in the material is stress-dependent and the shape of the coupon is slightly tapered. The coupon has the smallest cross-sectional area in the middle of the coupon, therefore resulting in slightly higher stresses compared to other locates along the coupon.

Alongside above limitations, the used approach still requires experimental testing on coupon level on multiple stress levels to gain the stiffness degradation data before you can set up the model for a specific new material. This is needed because an appropriate fitting curve for three load levels is preferred to accurately interpolate and extrapolate other stress ranges. More stress levels are also possible, but a minimum of three is recommended. Each stress level will require multiple tests in order to ensure that the data is representative.

7.3. Recommendations

Future research can focus on several areas to further improve the accuracy of the results. The first recommendation to investigate is the method for defining more precise fitting curves. Currently, the process uses multiple fitting curves, that are based on other fitting curves. The first fitting curve used is based on an ellipse, that describes the stiffness degradation curve of the experimental results. For each fitting curve, a limited amount of points is used to determine the entire fitting curve. Currently, each load level uses 20 data points, set at a fixed interval based on the amount of cycles. One of the disadvantages of this approach is that, especially for the low load levels, a large interval is between each point. This causes a less accurate fitting curve, and especially influences the accuracy of the damage estimation at each cycle. If one increases the number of data points, the expectation will be that the damage curves as shown in Figure 6.6 will all coincide more, currently the 30 kN load level deviates due to the first 20 cycles not being considered.

Instead of using a new fitting curve with decreased intervals to estimate the damage per cycle, one could also try to use the derivative of the ellipse equation instead. This will result in the exact rate at which the material stiffness is degrading over the amount of cycles. With these new lines, a more accurate damage fitting curve can be set for each load level. It will also be interesting to see if by having many more data points towards the end of the 30 kN stiffness degradation slope, the damage per cycle curve over the total amount of damage (as shown in Figure 6.7) will showcase the same increasing behavior at the end, or if it stays flat. This would indicate that the failure mechanism type should be deviating as well.

As mentioned at the limitations of the model, the stiffness failure limit is currently assumed to be constant among all load levels. However, during experimental testing, it was found to be slightly deviating per load level. A recommendation for further improving the model is to instead implement this stiffness

failure limit as a variable as well, depending on the load level. A first suggestion to implement this new variable is briefly described in section 6.6.5.

Lastly, as this model currently focuses on crack initiation, one should pursue the capabilities of trying to predict the next stage, which is crack propagation. This can be validated by creating a CT-model. Another interesting follow-up study will be to look at the applications of this method on more geometrical complex models, or for instance larger size structures instead of the coupon designs at which it was currently applied.

In addition to above recommendations, it is recommended to research how the results from this model can be implemented in actual projects. Currently, the model produces results, but does not consider safety factors due to external influences. The focus should lie on how to get a design value from these results, that takes into account safety measures.

References

[1] Mar. 2018. URL: https://discovercomposites.com/what-are-composites/.

[2] MH Abd Allah et al. “Effect of fibre volume fraction on the fatigue behaviour of GRP pultruded rod composites”. In: *Composites Science and Technology* 56.1 (1996), pp. 23–29.

[3] M Brod, A Dean, and R Rolfes. “Numerical life prediction of unidirectional fiber composites under block loading conditions using a progressive fatigue damage model”. In: *International Journal of Fatigue* 147 (2021), p. 106159.

[4] M Brod et al. “Numerical modeling and experimental validation of fatigue damage in Cross-Ply CFRP composites under inhomogeneous stress states”. In: *Composites Part B: Engineering* 200 (2020), p. 108050.

[5] F.C. Campbell. *Structural Composite Materials*. ASM International, 2010. ISBN: 978-1-61503-037-8. URL: https://app.knovel.com/hotlink/toc/id:kpSCM00001/structural-composite/structural-composite.

[6] Pei Chi Chou and Robert Croman. “Residual strength in fatigue based on the strength-life equal rank assumption”. In: *Journal of Composite materials* 12.2 (1978), pp. 177–194.

[7] CG Dávila. “From SN to the Paris law with a new mixed-mode cohesive fatigue model for delamination in composites”. In: *Theoretical and Applied Fracture Mechanics* 106 (2020), p. 102499.

[8] Ives De Baere, Wim Van Paepegem, and Joris Degrieck. “Comparison of different setups for fatigue testing of thin composite laminates in bending”. In: *International Journal of Fatigue* 31.6 (2009), pp. 1095–1101.

[9] Degrieck, and Wim Van Paepegem. “Fatigue damage modeling of fibre-reinforced composite materials: Review”. In: *Applied Mechanics Reviews* 54.4 (July 2001), pp. 279–300. ISSN: 0003-6900. DOI: 10.1115/1.1381395. eprint: https://asmedigitalcollection.asme.org/appliedmechanicsreviews/article-pdf/54/4/279/5438146/279_1.pdf. URL: https://doi.org/10.1115/1.1381395.

[10] Dominik Flore and Konrad Wegener. “Influence of fibre volume fraction and temperature on fatigue life of glass fibre reinforced plastics”. In: *AIMS Materials Science* 3.3 (2016), pp. 770–795.

[11] B. Harris. “Fatigue and accumulation of damage in reinforced plastics”. In: *Composites* 8.4 (1977). Fatigue of frp composites, pp. 214–220. ISSN: 0010-4361. DOI: https://doi.org/10.1016/0010-4361(77)90105-7. URL: https://www.sciencedirect.com/science/article/pii/0010436177901057.

[12] MKR Hashim, MS Abdul Majid, and MJM Ridzuan. “Review of fatigue responses of fiber-reinforced polymer (FRP) composite”. In: *Structural Health Monitoring System for Synthetic, Hybrid and Natural Fiber Composites* (2021), pp. 127–141.

[13] CJ Jones et al. “The Environmental Fatigue Behaviour of Reinforced Plastics”. In: *Proceedings of the Royal Society of London. Series A, Mathematical and Physical Sciences* (1984), pp. 315–338.

[14] Mathew W Joosten, Carlos G Dávila, and Qingda Yang. “Predicting fatigue damage in composites subjected to general loading conditions”. In: *Composites Part A: Applied Science and Manufacturing* 156 (2022), p. 106862.

[15] Ascione L et al. *Prospect for new guidance in the design of FRP*. Technical Report LB-NA-27666-EN-C (print),LB-NA-27666-EN-N (online). Ispra (Italy), 2016. DOI: 10.2788/851558(print),10.2788/22306(online).

[16] Saptarshi Maiti et al. “Sustainable fiber-reinforced composites: A Review”. In: *Advanced Sustainable Systems* 6.11 (2022), p. 2200258.

[17] P. K. Mallick. *Fiber-reinforced composites: Materials, manufacturing, and Design*. Taylor & amp; Francis, 2007.

[18] *Plastics - Determination of Tensile Properties - Part 4: Test Conditions for Isotropic and Orthotropic Fibre-Reinforced Plastic Composites*. Delft, Netherlands: Nederlands Normalisatie-instituut (NEN), 2023.

[19] Poly Service. *Infoblad Poly-Pox 500 - Harder 455*. Accessed: 2024-01-30. 2023. URL: https://www.polyservice.nl/pdf/tib/Poly-Pox/Infoblad%20Poly-Pox%20500%20-%20Harder%20455.pdf.

[20] Shahram Sarkani et al. “Stochastic Fatigue Damage Accumulation of FRP Laminates and Joints”. In: *Journal of Structural Engineering* 125.12 (1999), pp. 1423–1431. DOI: 10.1061/(ASCE)0733-9445(1999)125:12(1423). eprint: https://ascelibrary.org/doi/pdf/10.1061/%28ASCE%290733-9445%281999%29125%3A12%281423%29. URL: https://ascelibrary.org/doi/abs/10.1061/%28ASCE%290733-9445%281999%29125%3A12%281423%29.

[21] Delft University of Technology. *FRPTool - Fiber Reinforced Polymer Analysis*. 2024. URL: https://delftxtools.tudelft.nl/frp/.

[22] Afrooz Kazemi Vanhari, Edward Fagan, and Jamie Goggins. “A novel estimation method for fitting fatigue data in the composite wearout model”. In: *Composite Structures* 287 (2022), p. 115384.

[23] Mahmoud Yousry Zaghloul, Moustafa Mahmoud Yousry Zaghloul, and Mai Mahmoud Yousry Zaghloul. “Influence of stress level and fibre volume fraction on fatigue performance of glass fibre-reinforced polyester composites”. In: *Polymers* 14.13 (2022), p. 2662.

A

Complete dimensions database

This Annex contains the complete database with all measurements of the coupons taken before testing.

Specimen dimensions

Tested
Being tested
Resin

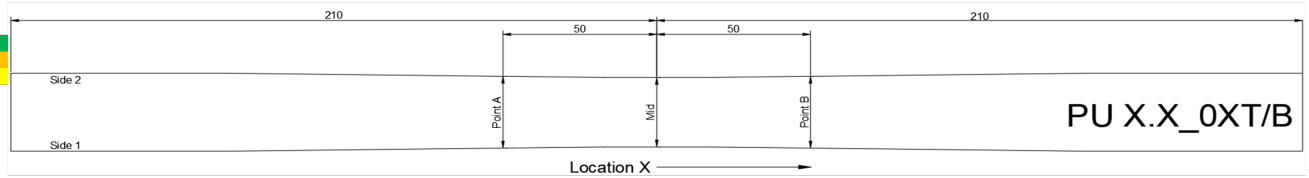

Coupon name	Type of test	Test order	Extra notes	Mid				Point A				Point B				Imperfection	Location,mm	Mid imperfection				-15 mm				+15 mm			
				Width	Thickness			Width	Thickness			Width	Thickness					Width	Thickness			Width	Thickness			Width	Thickness		
					Side 1	Side 2	Average		Side 1	Side 2	Average		Side 1	Side 2	Average				Side 1	Side 2	Average		Side 1	Side 2	Average		Side 1	Side 2	Average
PU 1.1_01B				24.32	10.23	10.38	10.305	25.36	10.76	10.64	10.700	24.87	10.89	10.79	10.840	None													
PU 1.1_02B	Fatigue 30kN 6Hz	19	Applied resin	24.27	9.31	9.01	9.160	25.00	9.66	9.03	9.345	24.98	9.83	9.07	9.450	None													
PU 1.1_03B				22.97	7.82	7.58	7.700	23.89	8.11	7.38	7.745	23.44	8.56	7.81	8.185	None													
PU 1.1_04B				24.40	10.55	10.68	10.615	25.12	10.67	10.81	10.740	25.14	10.78	10.78	10.780	None													
PU 1.1_01_top	Static	1		24.30	10.18	10.18	10.180	-	0.00	0.00	0.000	-	0.00	0.00	0.000	None													
PU 1.1_02T	Fatigue 100kN 2Hz	3	Run twice for dem	24.14	10.06	9.25	9.655	25.30	9.90	9.33	9.615	24.86	9.58	9.37	9.475	None													
PU 1.1_03T				24.44	10.42	10.70	10.560	24.90	10.43	10.70	10.565	25.35	10.29	10.52	10.405	Really small dimpel	-92.00	25.93	10.5	10.01	10.255	26.24	10.37	10.44	10.405	25.5	10.42	10.56	10.490
PU 1.1_04T				23.38	11.20	10.48	10.840	24.43	11.70	11.14	11.420	23.57	10.45	9.62	10.035	None													
PU 1.2_01B	Static	7		24.36	8.92	8.73	8.825	25.35	7.77	7.99	7.880	24.86	8.71	9.02	8.865	Dimpel	-50.00	25.35	7.77	7.99	7.880	25.8	8.41	8.71	8.560	25.23	8.9	8.93	8.915
PU 1.2_02B				24.29	10.30	10.19	10.245	25.00	10.48	10.40	10.440	25.03	10.35	10.06	10.205	Slightly bend													
PU 1.2_03B				24.28	8.85	8.57	8.710	25.12	8.92	8.66	8.790	25.05	8.88	8.77	8.825	None													
PU 1.2_04B	Fatigue 70 kN 2Hz	24	Resin w surface pr	24.36	10.33	8.70	9.515	24.74	10.28	8.92	9.600	25.31	10.29	8.44	9.365	Dimpel	45.00	25.22	10.04	8.41	9.225	24.95	10.25	9.02	9.635	25.52	10.34	9.2	9.770
PU 1.2_01T	Static	2		24.40	9.18	9.40	9.290	25.35	9.47	9.54	9.505	24.86	9.40	9.53	9.465	None													
PU 1.2_02T	Fatigue 70kN 2Hz	4		24.34	9.47	9.11	9.290	25.27	9.57	9.25	9.410	24.77	9.20	9.31	9.255	None													
PU 1.2_03T				24.32	9.77	10.50	10.135	24.73	9.87	10.44	10.155	25.29	9.73	10.38	10.055	None													
PU 1.2_04T				24.42	9.35	10.03	9.690	24.88	9.56	9.94	9.750	25.45	9.31	10.04	9.675	None													
PU 1.3_01B				24.33	10.09	9.05	9.570	25.07	10.38	9.27	9.825	25.03	10.43	9.49	9.960	None													
PU 1.3_02B				24.30	8.80	8.77	8.785	25.05	8.55	8.75	8.650	25.01	8.47	8.60	8.535	Small bump/curve	-10.00	24.32	8.56	8.66	8.610	24.52	8.69	8.75	8.720	24.32	8.59	8.75	8.670
PU 1.3_03B				24.32	9.16	10.59	9.875	24.91	8.90	10.20	9.550	25.25	9.09	10.42	9.755	None													
PU 1.3_04B	Fatigue 50kN 4Hz	15	Resin ends	24.28	8.53	8.60	8.565	24.80	9.11	8.50	8.805	25.24	8.54	8.72	8.630	None													
PU 1.3_01T	Fatigue 50kN 4Hz	31	Resin w surface pr	24.20	8.62	8.88	8.750	25.19	9.47	9.49	9.480	24.68	8.75	9.08	8.915	Small increase in thickness starting at point A													
PU 1.3_02T				24.35	10.23	9.45	9.840	24.80	10.40	9.70	10.050	25.27	10.50	9.46	9.980	None													
PU 1.3_03T	Fatigue 70kN 2Hz	23	Resin w surface pr	24.45	9.15	8.89	9.020	24.84	8.98	8.66	8.820	25.22	8.80	8.78	8.790	None													
PU 1.3_04T	Fatigue 70kN 2Hz	14	Resin ends	24.26	10.05	8.82	9.435	24.73	10.24	9.28	9.760	25.24	10.50	9.91	10.205	Small increase in thickr	40.00												
PU 1.4_01B	Static	8		24.22	8.26	8.53	8.395	25.14	8.90	8.93	8.915	24.61	8.35	8.49	8.420	Dimpl, but not loc. of f	-35.00	24.88	7.8	7.84	7.820	25.14	8.9	8.93	8.915	24.64	8.91	8.51	8.710
PU 1.4_02B	Fatigue 25kN 6Hz	29	Resin w surface pr	24.19	8.71	8.50	8.605	24.91	8.64	8.42	8.530	24.86	8.93	8.33	8.630	Small bend	-70.00												
PU 1.4_03B	Fatigue 70kN 2Hz	32	Resin w surface pr	24.35	9.84	11.45	10.645	25.00	9.24	10.41	9.825	25.10	9.98	10.45	10.215	Large variation in thickness at one side													
PU 1.4_04B	Fatigue 30kN 6Hz	20	Applied resin	24.34	9.81	8.65	9.230	24.79	9.53	8.59	9.060	25.32	10.38	8.76	9.570	Dimpel	35.00	25.08	9.01	8.18	8.595	24.73	9.72	8.6	9.160	25.32	10.38	8.76	9.570
PU 1.4_01T				24.36	9.83	10.82	10.325	25.25	9.83	10.50	10.165	24.74	9.83	10.63	10.230	None													
PU 1.4_02T	Fatigue 70kN 2Hz	10		23.64	8.85	9.33	9.090	24.72	8.93	9.33	9.130	24.20	8.87	9.46	9.165	None													
PU 1.4_03T				24.22	9.36	9.50	9.430	24.74	9.27	9.30	9.285	25.18	9.32	9.28	9.300	None													
PU 1.4_04T				24.15	9.25	9.09	9.170	24.63	9.12	9.07	9.095	25.13	9.17	8.81	8.990	None													
PU 2.1_01B	Static + dimpel	6	The filename and	24.36	9.87	10.20	10.035	25.30	10.11	10.59	10.350	24.80	9.86	10.41	10.135	Dimpel	-40.00	25.06	9.14	10	9.570	25.37	9.77	10.49	10.130	24.76	9.99	10.7	10.345
PU 2.1_02B	Fatigue 30kN 6Hz	26	Resin w surface pr	24.08	8.67	9.04	8.855	24.57	8.67	8.58	8.625	24.92	8.55	8.88	8.715	Dimpel	40.00	24.8	7.94	8.06	8.000	24.51	8.74	8.71	8.725	24.91	8.77	8.8	8.785
PU 2.1_03B	Fatigue 30kN 6Hz	25	Resin w surface pr	24.03	8.71	8.92	8.815	24.81	8.55	8.56	8.555	24.80	8.90	9.00	8.950	Small bend	-60.00												
PU 2.1_04B				24.30	10.59	9.58	10.085	25.12	10.37	9.43	9.900	25.02	10.22	9.71	9.965	None													
PU 2.1_01T				24.26	10.71	11.18	10.945	25.26	10.61	11.15	10.880	24.70	10.70	11.12	10.910	None													
PU 2.1_02T	Fatigue 70kN 2Hz	9		24.23	10.17	10.54	10.355	25.25	10.71	10.81	10.760	24.73	10.56	10.60	10.580	None													
PU 2.1_03T	Fatigue 30kN 6Hz	30	Filename = 1.3-01	24.41	9.11	9.84	9.475	25.54	8.95	9.88	9.415	24.89	8.90	9.65	9.275	None													
PU 2.1_04T	Fatigue 70kN 2Hz	33	Resin w surface pr	24.03	9.37	10.19	9.780	24.98	9.35	10.19	9.770	24.45	9.19	10.10	9.645	Small increase in thickr	85.00	25.48	9.5	10.42	9.960	25.04	9.08	10.06	9.570				
PU 2.2_01B				24.49	10.69	10.77	10.730	25.04	10.51	10.51	10.510	25.36	10.69	10.88	10.785	None													
PU 2.2_02B				24.28	9.99	10.38	10.185	25.12	10.48	10.55	10.515	25.19	10.82	10.55	10.685	Large variation in thick	90.00	25.91	11.83	10.56	11.195	25.59	11.76	10.67	11.215	26.33	10.76	10.56	10.660
PU 2.2_03B	Fatigue 70kN 2Hz	13	Applied resin + tap	24.30	10.42	8.92	9.670	25.00	10.01	8.96	9.485	25.10	10.50	9.03	9.765	None													
PU 2.2_04B	Fatigue 30kN 6Hz	17	Applied resin	24.26	10.52	8.98	9.750	25.21	10.63	8.76	9.695	24.90	10.65	8.95	9.800	None													
PU 2.2_01T				23.64	10.86	11.34	11.100	24.78	10.87	11.17	11.020	24.02	10.86	10.94	10.900	None													
PU 2.2_02T	Fatigue 30kN 6Hz	35	Resin w surface pr	24.48	10.62	10.46	10.540	25.40	10.63	10.15	10.390	24.93	10.67	10.38	10.525	None													
PU 2.2_03T				24.33	9.74	9.36	9.550	25.30	9.50	9.11	9.305	24.80	9.77	9.39	9.580	None													
PU 2.2_04T				24.31	10.72	9.96	10.340	25.26	10.80	9.70	10.250	24.70	10.49	9.50	9.995	None													
PU 2.3_01B	Fatigue 50kN 4Hz	34	Resin w surface pr	24.28	10.04	9.75	9.895	25.26	10.20	9.88	10.040	24.82	9.56	9.60	9.580	Dimpel/slight bend	50.00	24.82	9.56	9.6	9.580	24.36	10.02	9.73	9.875	25.41	10.3	9.97	10.135
PU 2.3_02B	Fatigue 50kN 4Hz	27	Resin w surface pr	24.39	8.58	10.32	9.450	25.40	8.37	10.13	9.250	24.92	8.65	10.18	9.415	Big difference in thickness in general between both sides													
PU 2.3_03B	Fatigue 30kN 6Hz & F 18+21		Applied resin	24.38	9.75	8.88	9.315	25.30	10.12	8.90	9.510	24.87	9.61	8.49	9.050	None													
PU 2.3_04B	Fatigue 50kN 4Hz	28	Resin w surface pr	24.34	9.02	9.60	9.310	25.26	8.59	9.43	9.010	24.65	8.65	9.46	9.055	Dimpel/slight bend	50.00	24.34	9.02	9.6	9.310	24.45	8.79	9.42	9.105	25.31	9.31	9.77	9.540
PU 2.3_01T	Fatigue 70kN 2Hz & 5 12 + 16		Applied resin + tap	24.32	9.33	9.73	9.530	25.35	9.47	9.76	9.615	24.99	9.57	9.73	9.650	None													
PU 2.3_02T	Failed before test		Resin w surface pr	24.37	9.38	10.42	9.900	25.32	9.49	10.54	10.015	24.81	9.42	10.19	9.805	None													
PU 2.3_03T				24.41	8.81	9.38	9.095	25.38	8.95	9.19	9.070	24.89	8.97	9.18	9.075	None													
PU 2.3_04T				23.20	9.00	9.32	9.160	24.46	8.88	9.41	9.145	23.37	8.79	9.11	8.950	None													
PU 2.4_01B				24.82	8.95	9.15	9.050	25.52	9.41	9.03	9.220	25.58	9.56	9.32	9.440	None													
PU 2.4_02B	Static	11		25.15	8.63	9.18	8.905	26.14	8.35	8.39	8.370	24.95	8.70	9.17	8.935	Dimpl, but not loc. of f	-50.00	26.14	8.35	8.39	8.370	26.47	9.08	9.32	9.200	25.92	8.91	9.14	9.025
PU 2.4_03B	Fatigue 70kN 2Hz	25	Resin w surface pr	24.54	9.03	10.09	9.560	25.58	8.89	9.28	9.085	24.88	9.03	9.89	9.460	Dimpel/slight bend	-50.00	25.58	8.89	9.28	9.085	25.7	9.41	10.21	9.810	25.26	9.97	10.24	10.105
PU 2.4_04B				24.41	10.42	10.68	10.550	25.13	10.37	10.80	10.585	25.41	10.14	10.80	10.470	None													
PU 2.4_01T	Static	5		24.34	9.70	10.13	9.915	25.26	9.66	10.23	9.945	24.77	9.55	9.83	9.690	None													
PU 2.4_02T				24.33	10.72	9.78	10.250	24.78	10.78	9.84	10.310	25.30	10.25	9.45	9.850	None													
PU 2.4_03T	Fatigue 70kN 2Hz	22	Resin w surface pr	23.85	8.83	8.96	8.895	24.97	8.64	8.92	8.780	24.26	8.65	9.01	8.830	Small dimpl located at upper clamp area, neglectable													
PU 2.4_04T				24.52	9.04	9.46	9.250	25.39	8.60	8.97	8.785	24.89	8.99	9.48	9.235	None													

Figure A.1: Full overview of the database, containing all dimensions of the coupons

B

Pictures static tested coupons

Except for coupon PU 2.4_02B, no pictures of the coupons before testing were taken. All images taken are from the coupons after the static tensile tests and showcase the damage from different views.

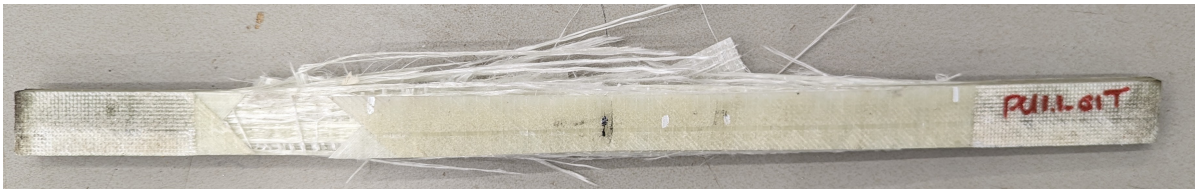

(a)

(b)

Figure B.1: Coupon PU 1.1_01T after failure

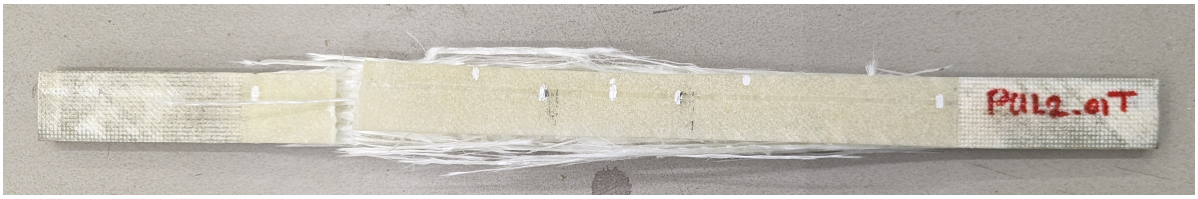

(a)

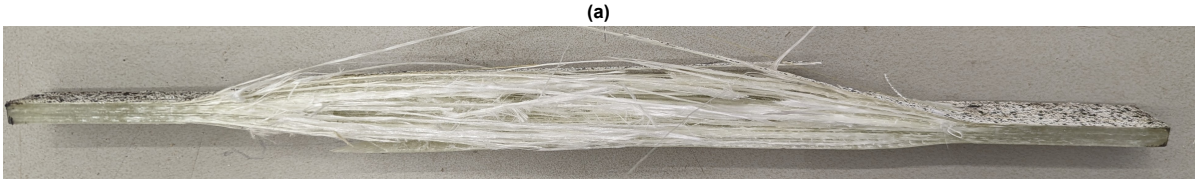

(b)

Figure B.2: Coupon PU 1.2_01T after failure

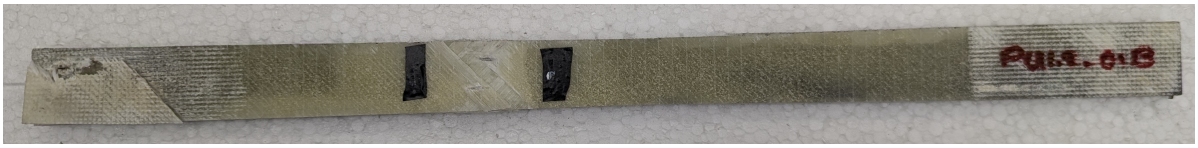

(a)

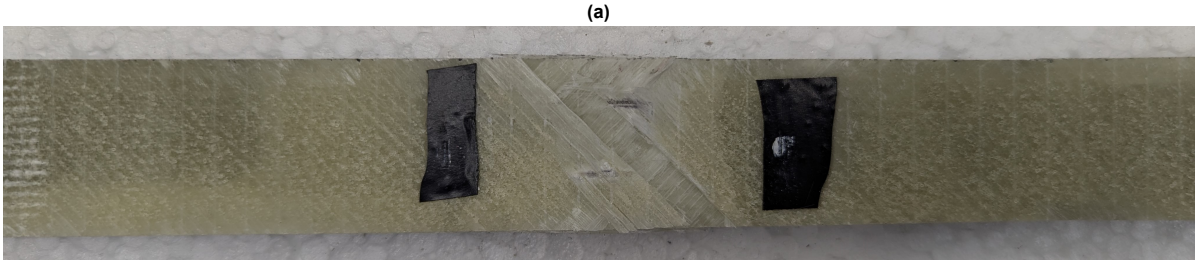

(b)

(c)

Figure B.3: Coupon PU 1.2_01B after failure

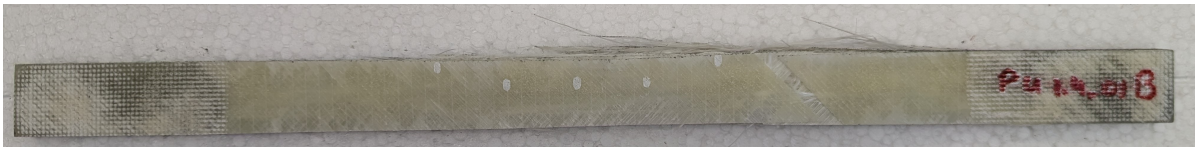

(a)

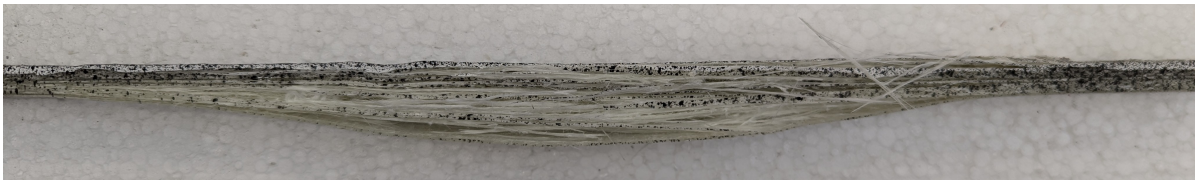

(b)

Figure B.4: Coupon PU 1.4_01B after failure

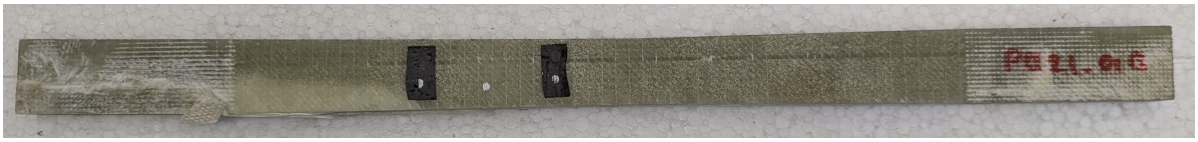

(a)

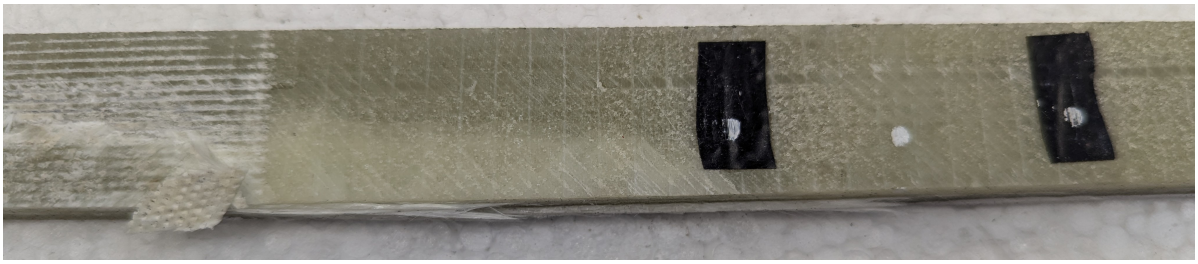

(b)

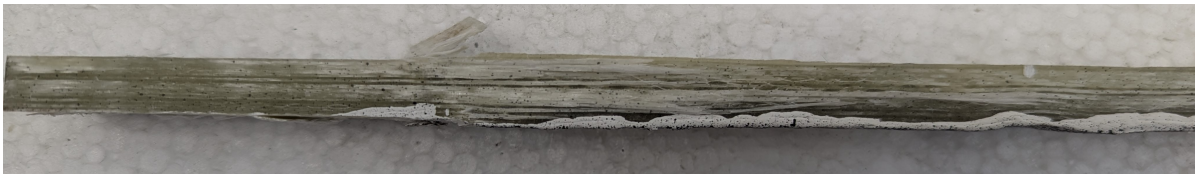

(c)

Figure B.5: Coupon PU 2.1_01B after failure

(a)

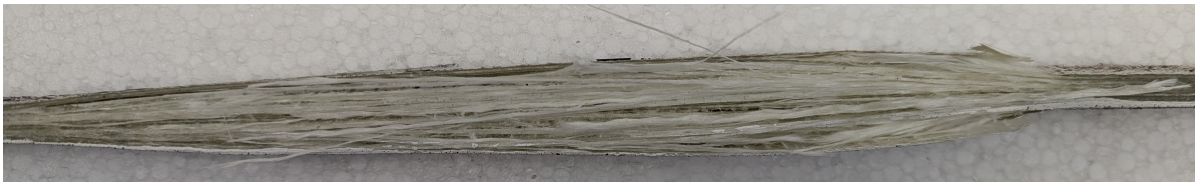

(b)

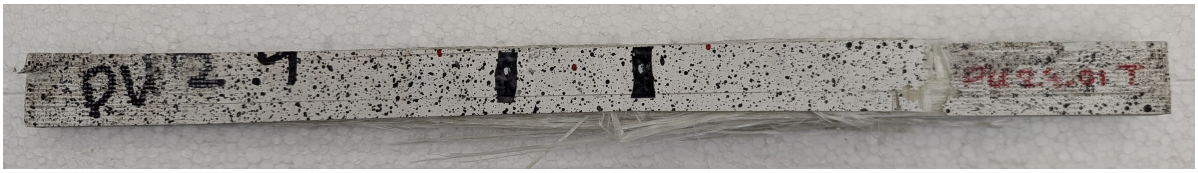

Figure B.6: Coupon PU 2.4_01T after failure

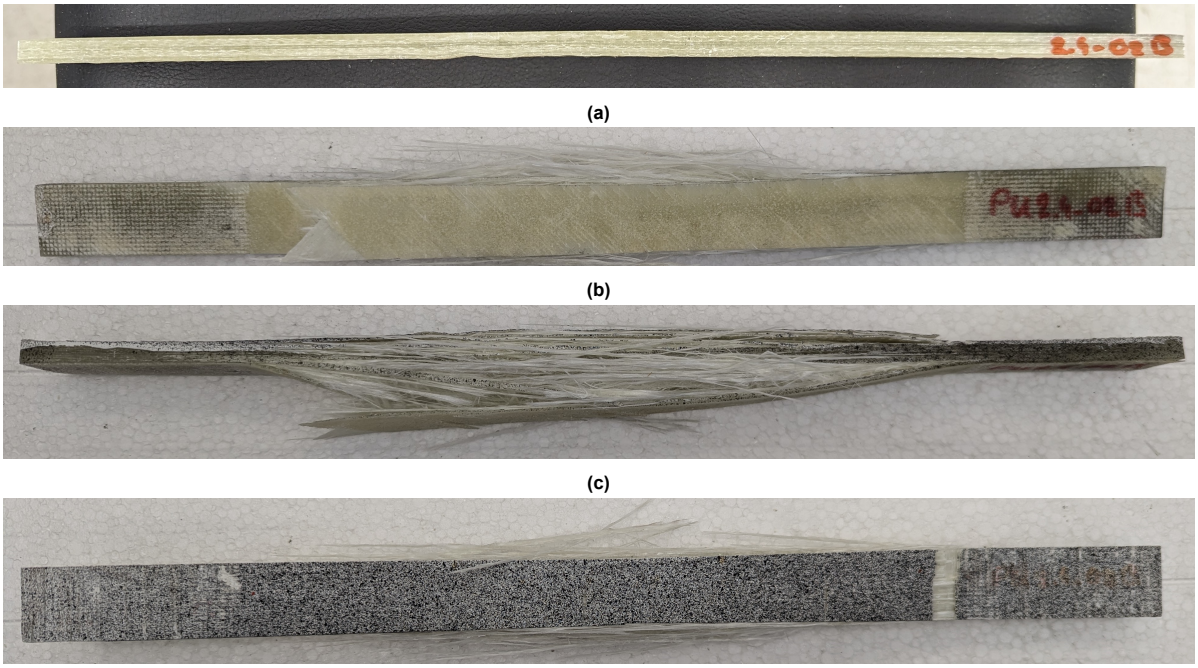

(a)

(b)

(c)

(d)

Figure B.7: Coupon PU 2.4_02B (a) before failure and (b), (c), (d) after failure

C

Pictures fatigue tested coupons

This annex contains all the pictures of the coupons that were tested on the fatigue life. The pictures are taken before and after testing. The chapter is divided per load level, showing both coupons with and without imperfections.

C.1. 30 kN coupons

This section shows all coupons tested on the 30 kN load level.

C.1.1. Without imperfections

(a)

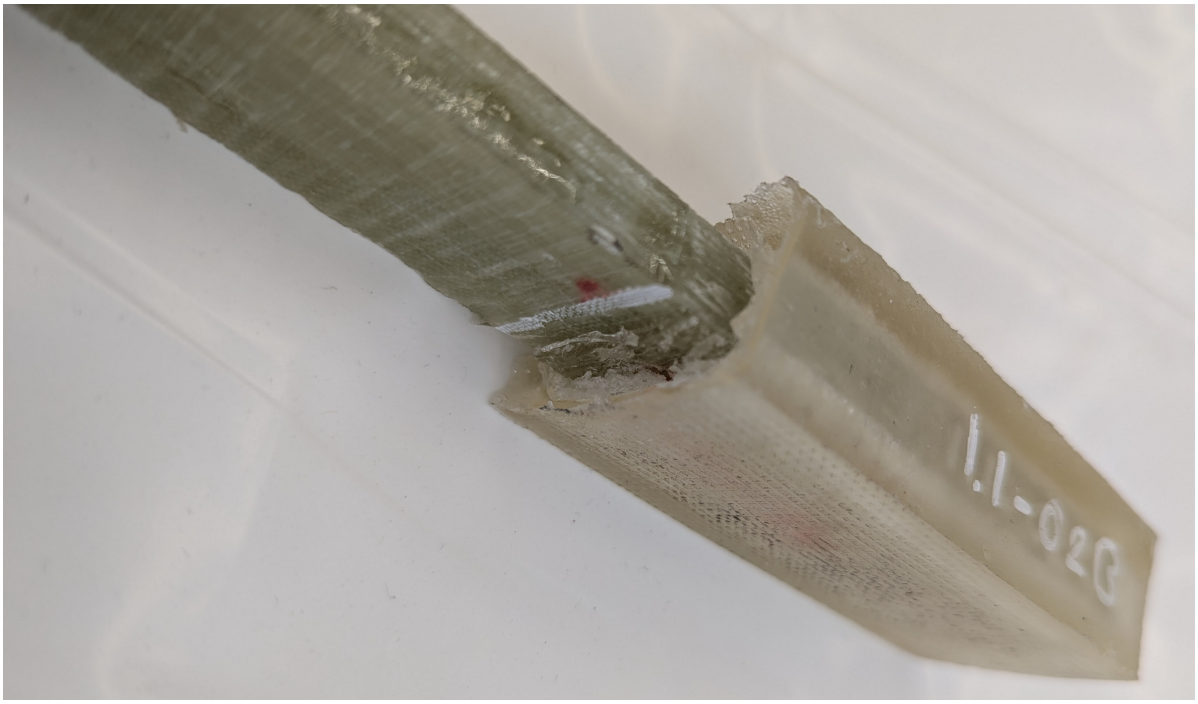

(b)

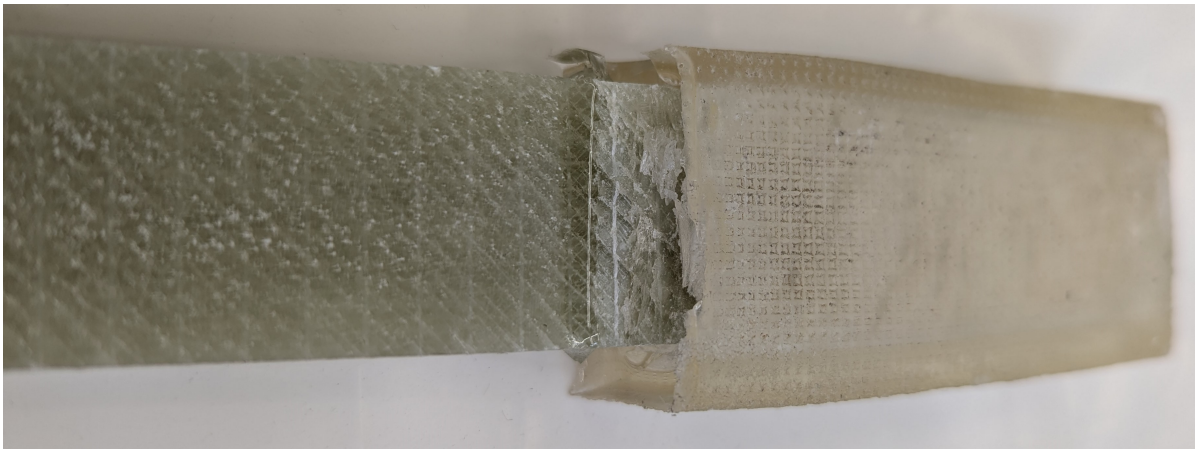

(c)

Figure C.1: [Disregarded] Coupon PU 1.1_02B (a) before testing, (b) and (c) after slipping of the resin

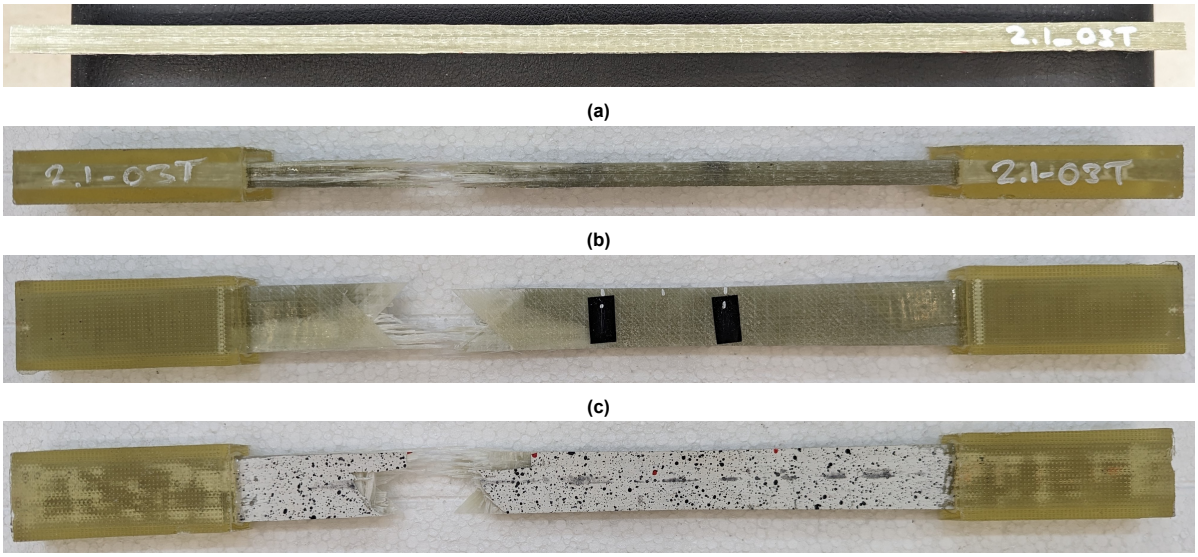

Figure C.2: Coupon PU 2.1_03T (a) before testing, (b), (c) and (d) after testing

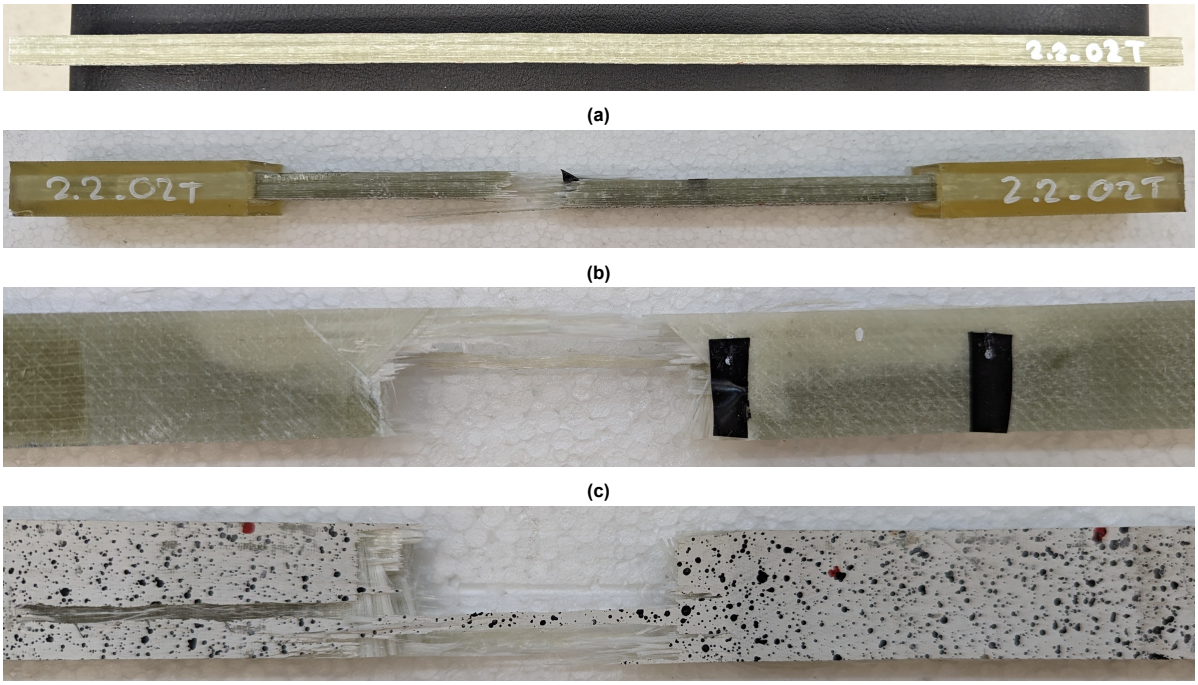

Figure C.3: Coupon PU 2.2_02T (a) before testing, (b), (c) and (d) after testing

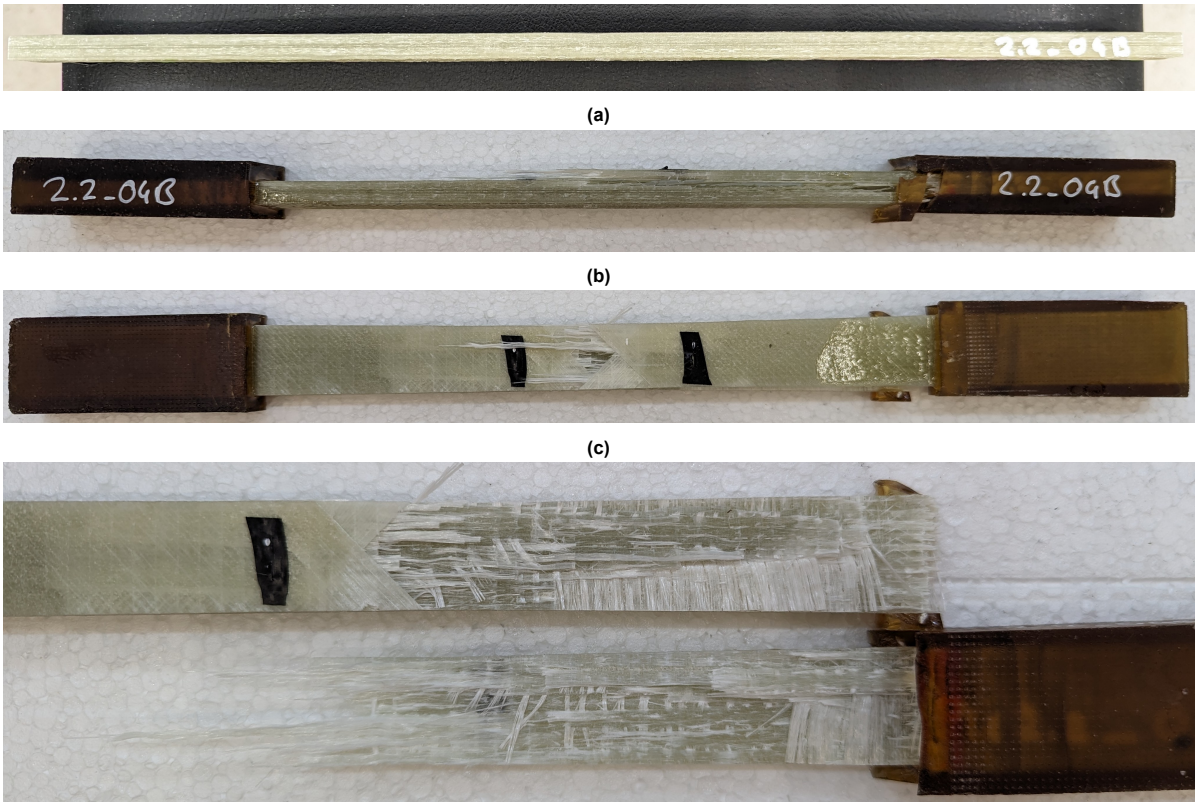

(a)

(b)

(c)

(d)

Figure C.4: Coupon PU 2.2_04B (a) before testing, (b), (c) and (d) after testing

C.1.2. With imperfections

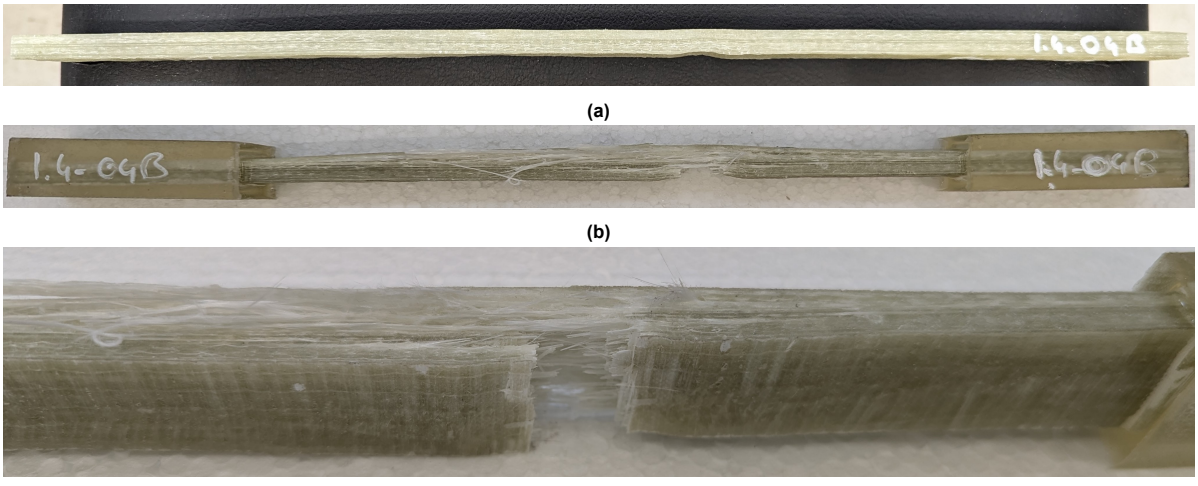

(a)

(b)

(c)

Figure C.5: Coupon PU 1.4_04B (a) before testing, (b) and (c) after failure

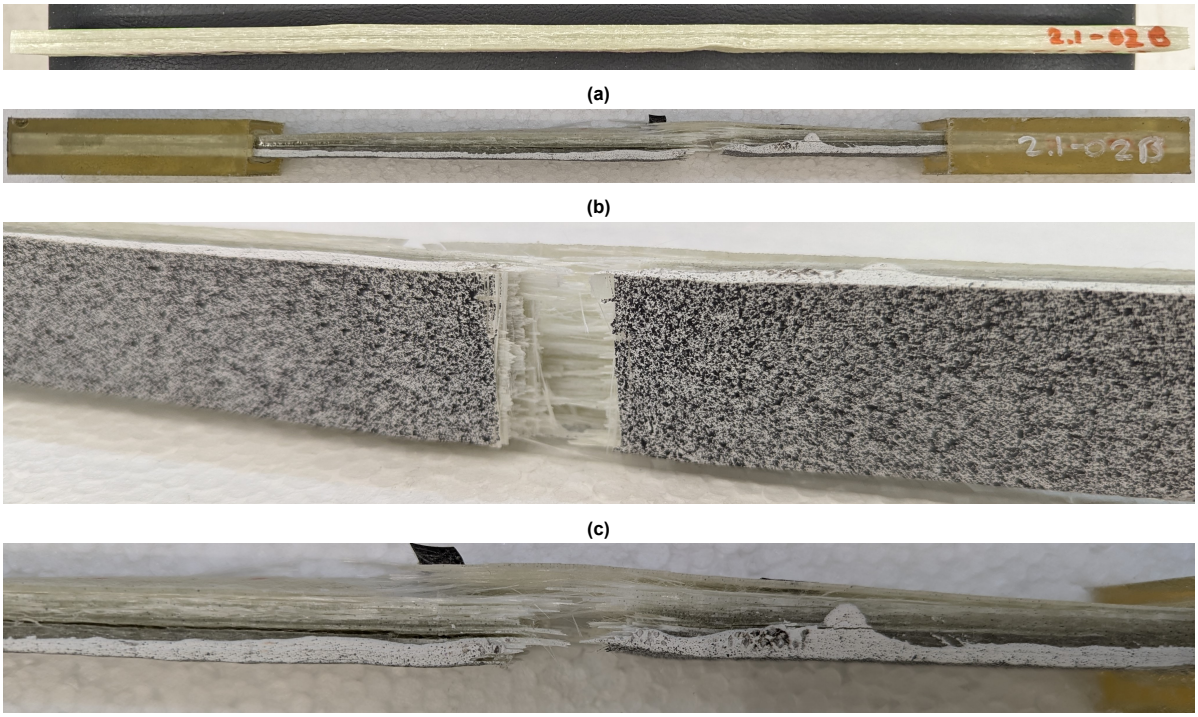

(a)

(b)

(c)

(d)

Figure C.6: Coupon PU 2.1_02B (a) before testing, (b), (c) and (d) after testing

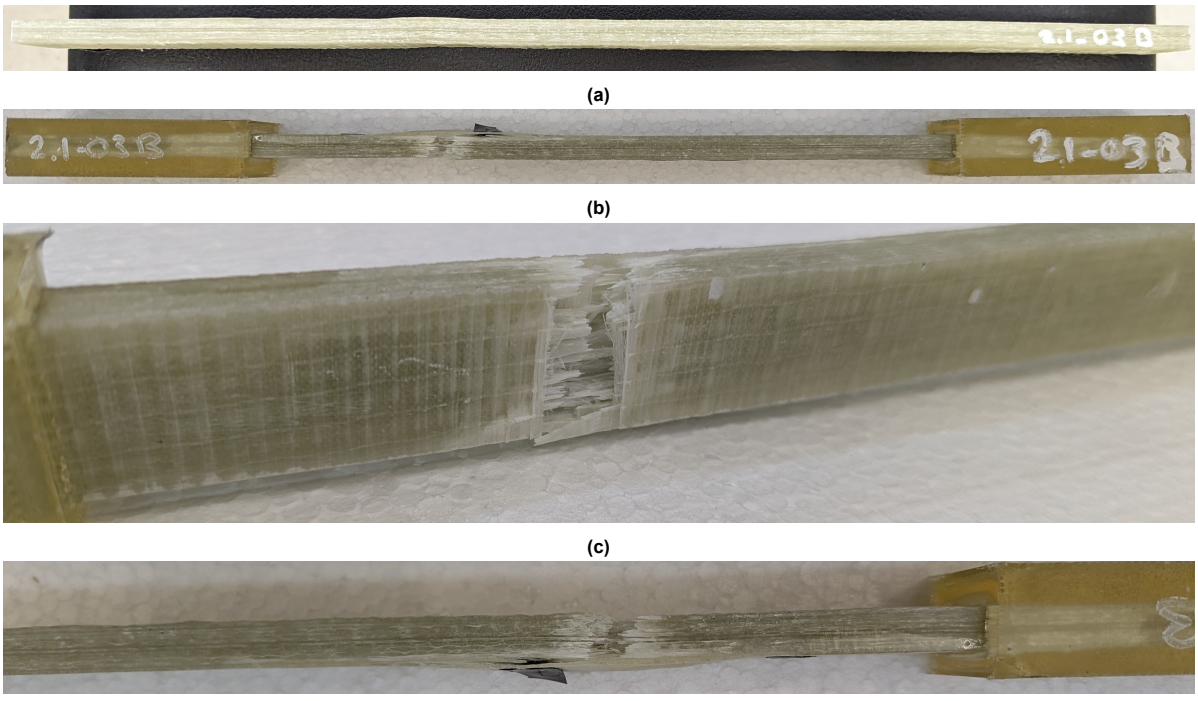

(a)

(b)

(c)

(d)

Figure C.7: Coupon PU 2.1_03B (a) before testing, (b), (c) and (d) after testing

C.2. 50 kN coupons

This section shows all coupons tested on the 50 kN load level.

C.2.1. Without imperfections

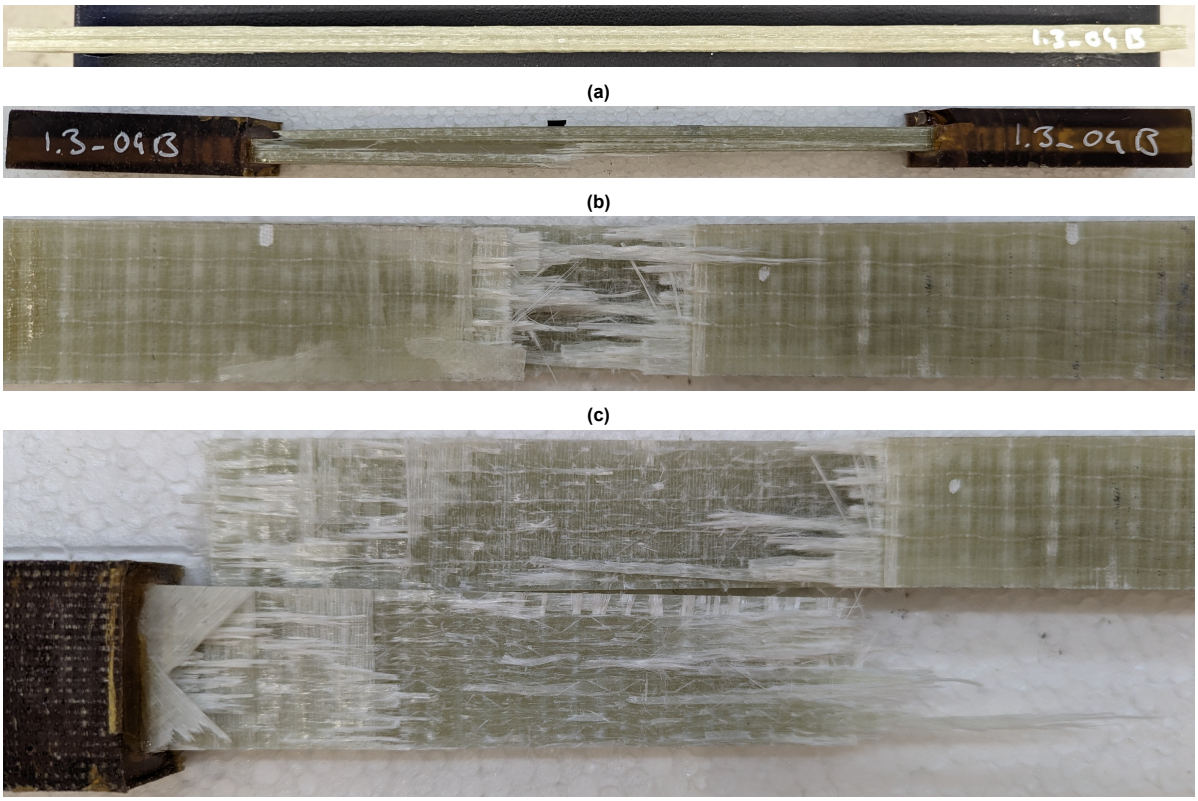

Figure C.8: Coupon PU 1.3_04B (a) before testing, (b), (c) and (d) after testing

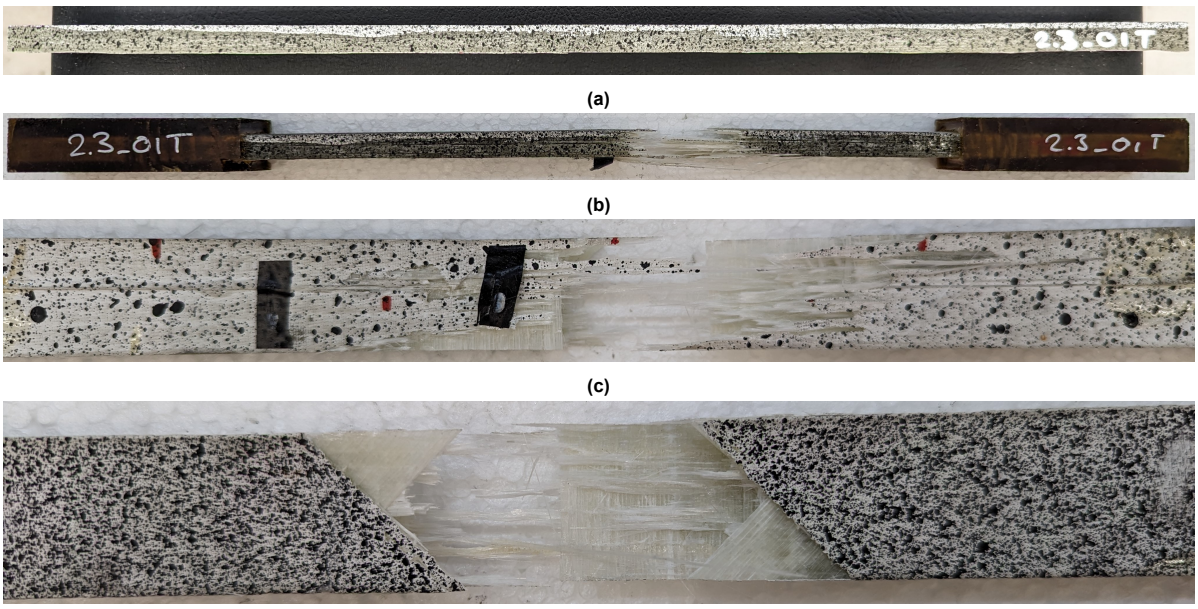

Figure C.9: Coupon PU 2.3_01T (a) before testing, (b), (c) and (d) after testing

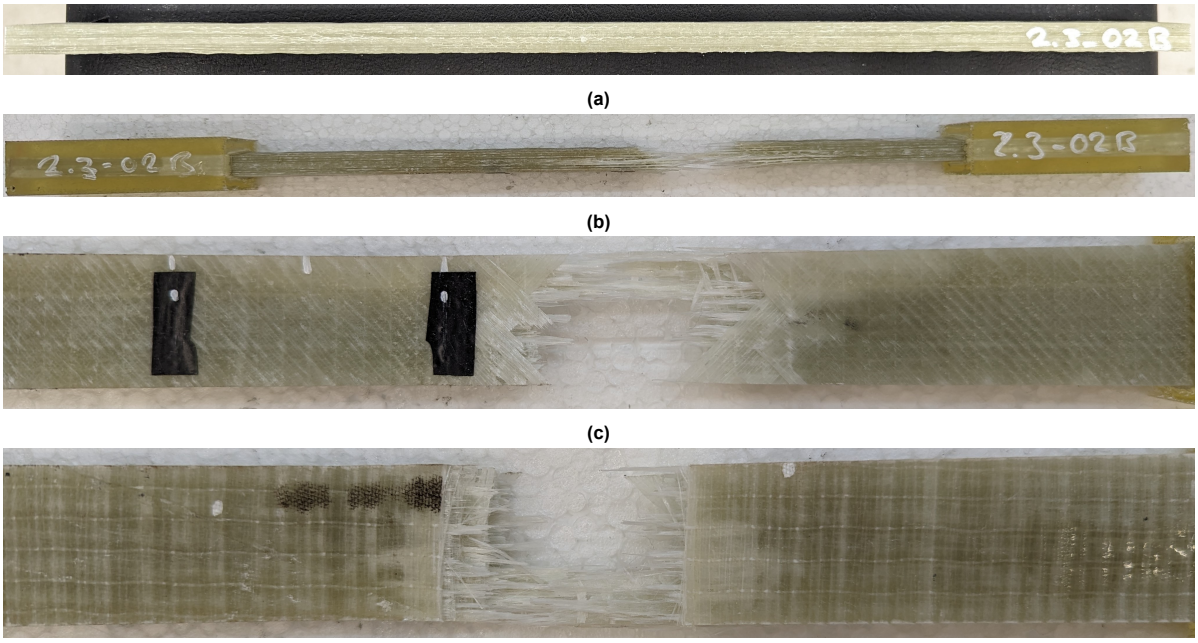

(a)

(b)

(c)

(d)

Figure C.10: Coupon PU 2.3_02B (a) before testing, (b), (c) and (d) after testing

C.2.2. With imperfections

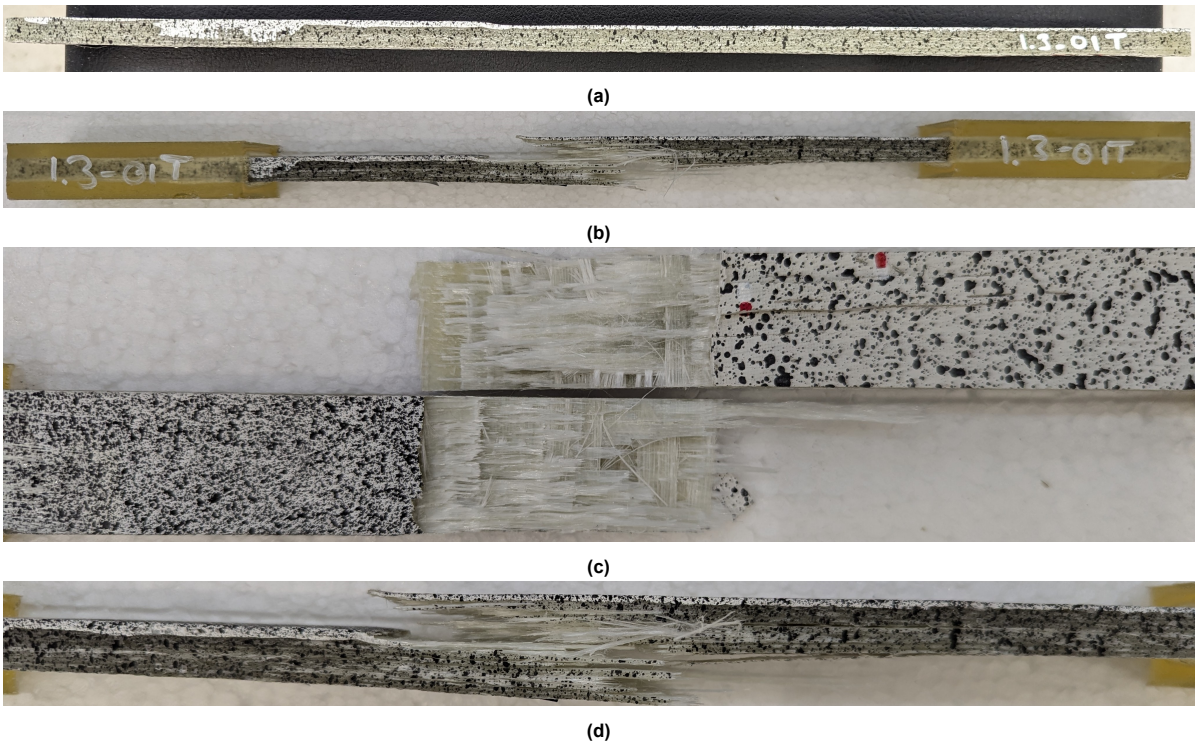

(a)

(b)

(c)

(d)

Figure C.11: Coupon PU 1.3_01T (a) before testing, (b), (c) and (d) after testing

(a)

(b)

(c)

(d)

Figure C.12: Coupon PU 2.3_01B (a) before testing, (b), (c) and (d) after testing

(a)

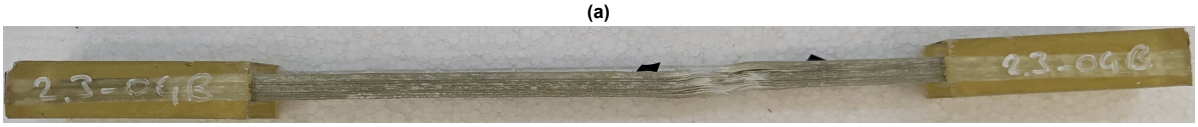

(b)

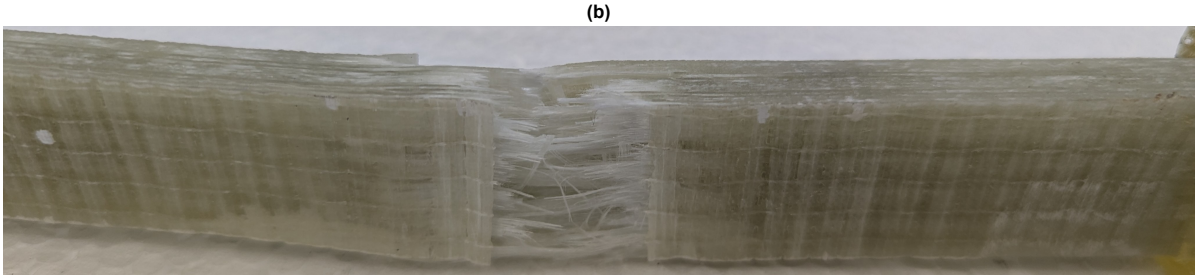

(c)

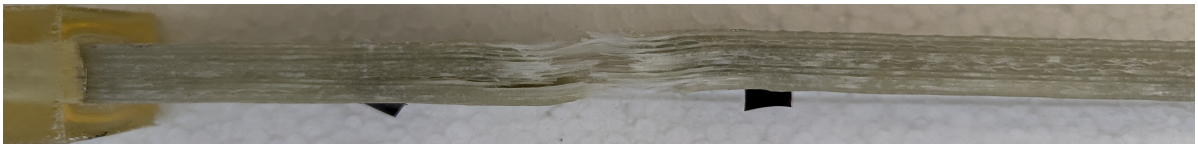

(d)

Figure C.13: Coupon PU 2.3_04B (a) before testing, (b), (c) and (d) after testing

C.3. 70 kN coupons

This section shows all coupons tested on the 70 kN load level.

C.3.1. Without imperfections

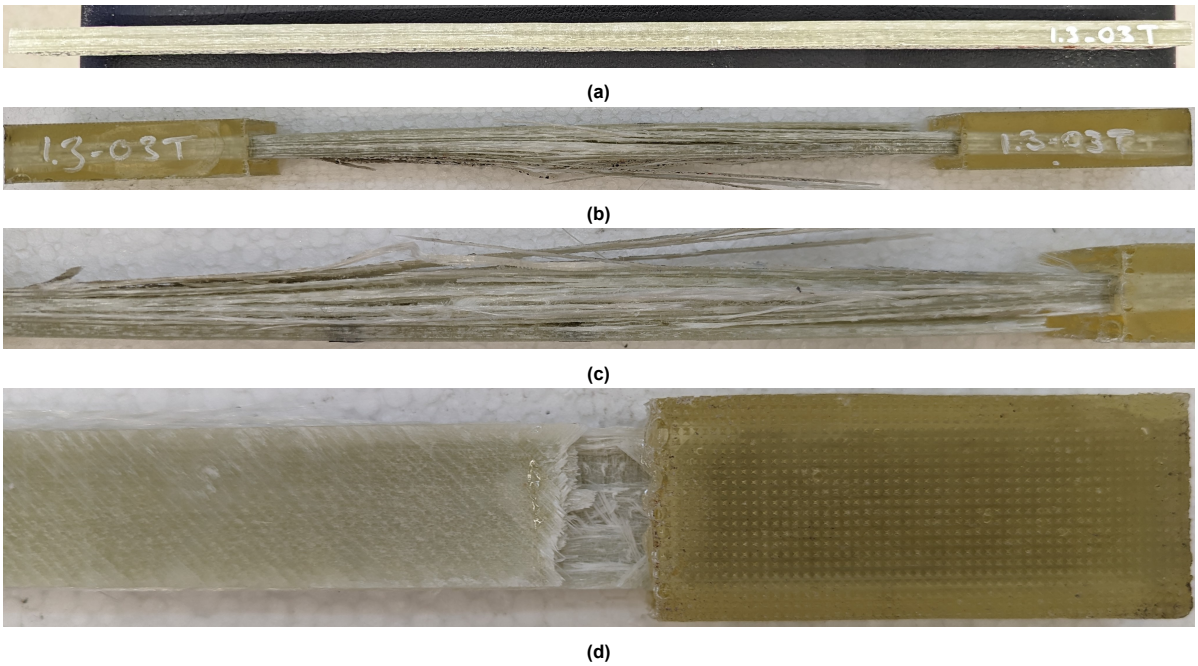

(a)

(b)

(c)

(d)

Figure C.14: Coupon PU 1.3_03T (a) before testing, (b), (c) and (d) after testing

(a)

(b)

(c)

(d)

(e)

Figure C.15: Coupon PU 1.4_03B (a) before testing, (b), (c), (d) and (e) after testing

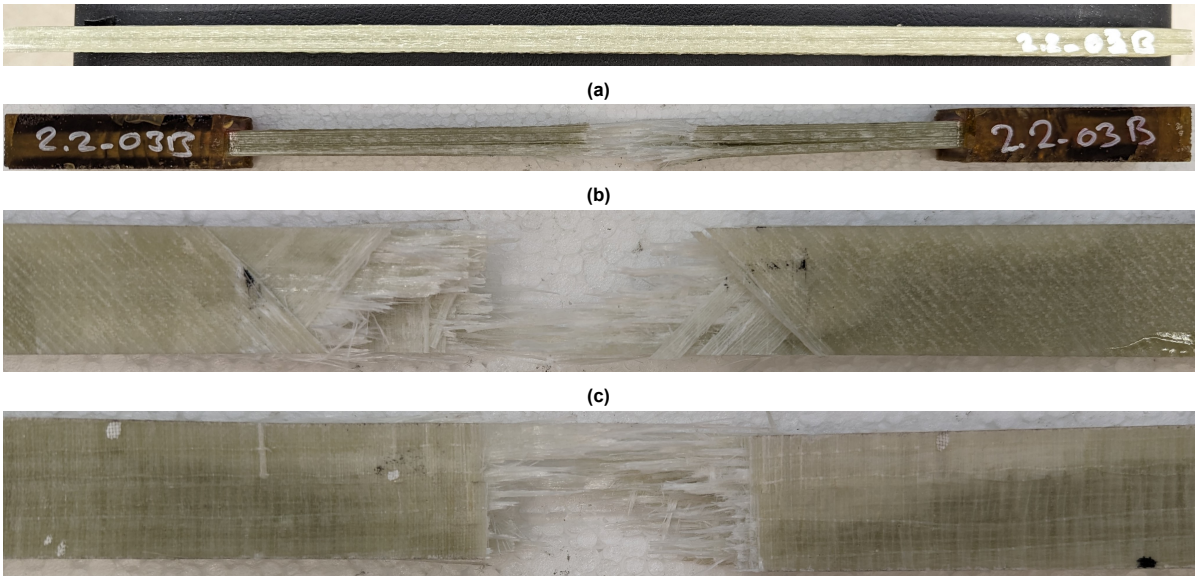

(a)

(b)

(c)

(d)

Figure C.16: Coupon PU 2.2_03B (a) before testing, (b), (c) and (d) after testing

(a)

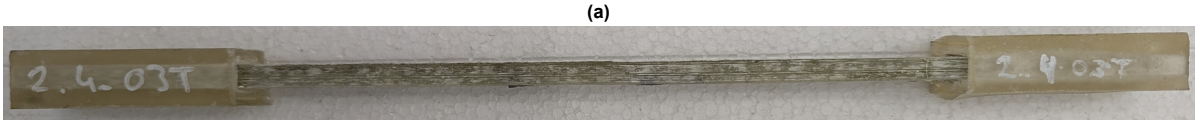

(b)

(c)

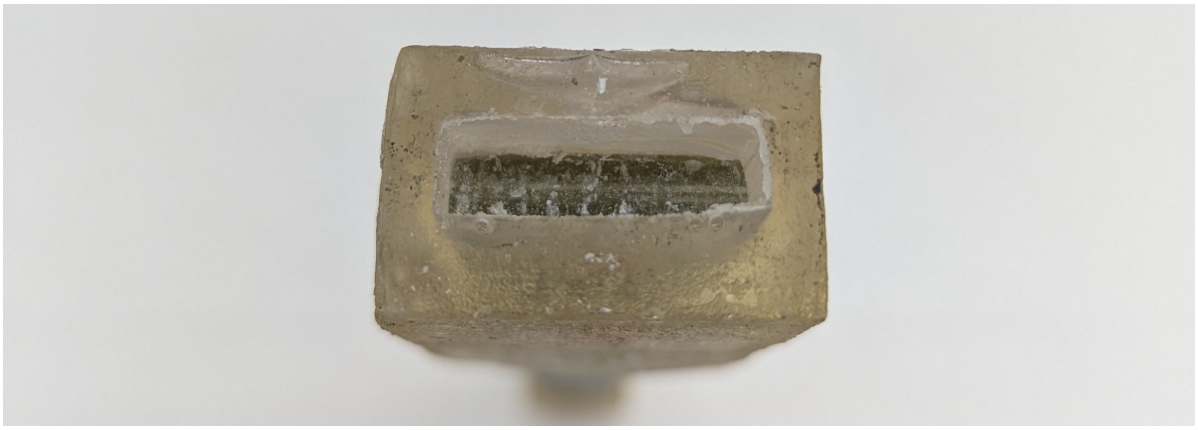

(d)

Figure C.17: Coupon PU 2.4_03T (a) before testing, (b), (c) and (d) after slipping of the resin

C.3.2. With imperfections

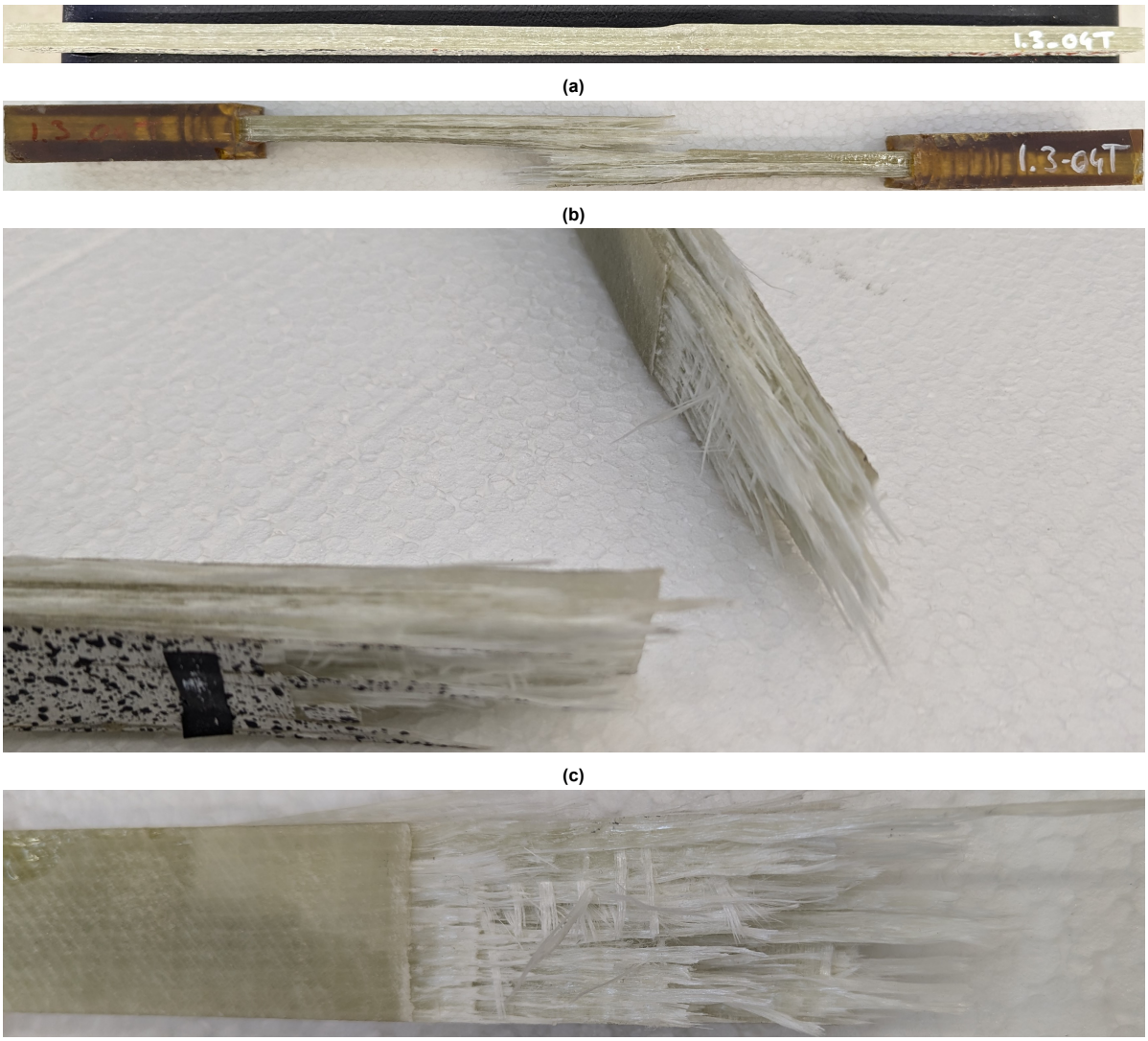

Figure C.18: Coupon PU 1.3_04T (a) before testing, (b), (c) and (d) after testing

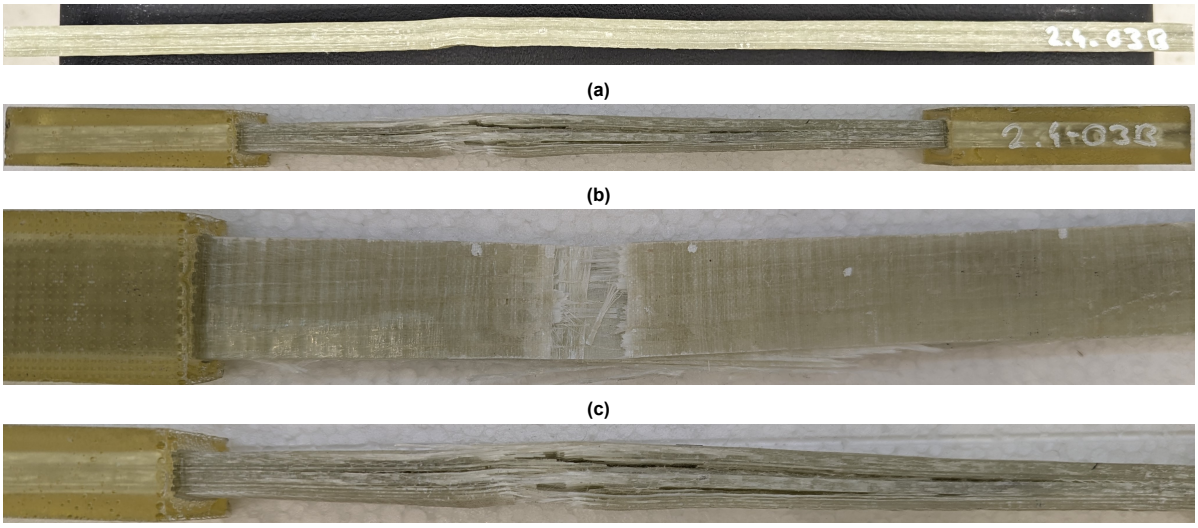

Figure C.19: Coupon PU 2.4_03B (a) before testing, (b), (c) and (d) after testing

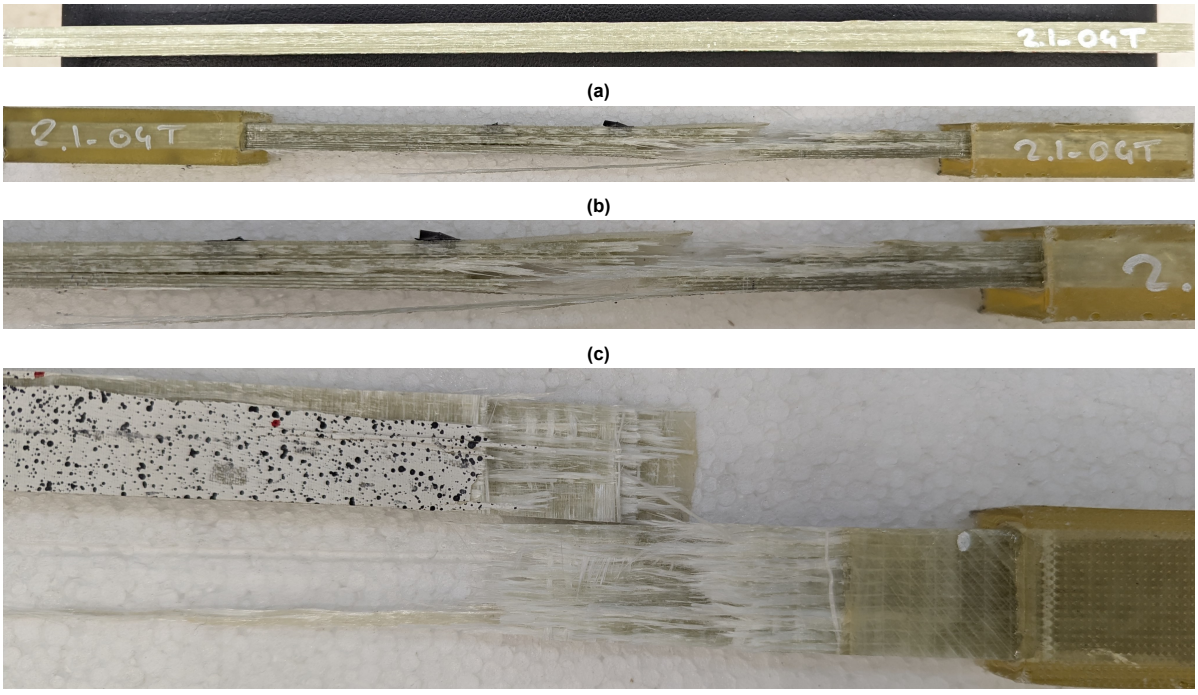

Figure C.20: Coupon PU 2.1_04T (a) before testing, (b), (c) and (d) after testing

C.4. Other coupons

The 25 kN coupon without imperfections.

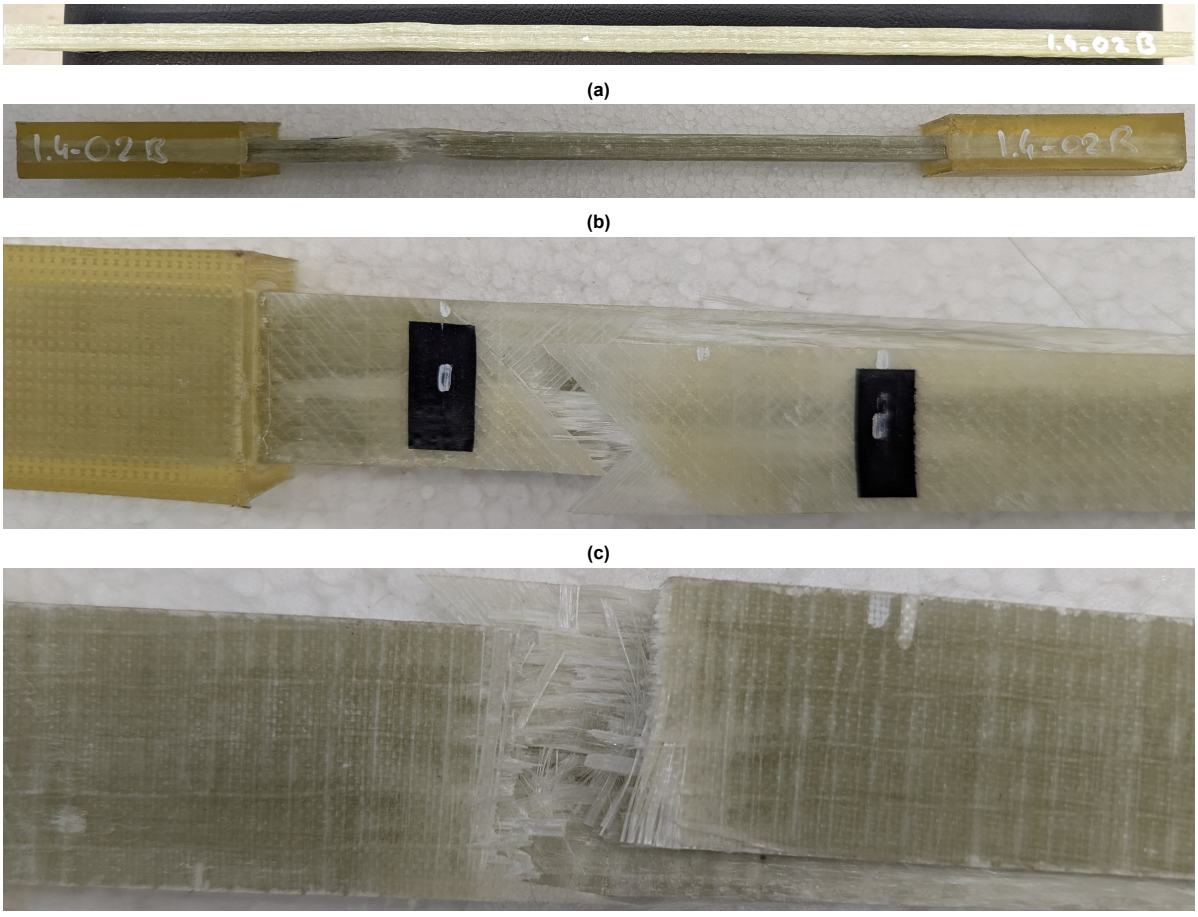

Figure C.21: Coupon PU 1.4_02B (a) before testing, (b), (c) and (d) after testing

The 20 kN coupon without imperfections. This coupon never reached full failure in the clamps due to an error in the machine resulting in compression in the coupon (Figure C.23).

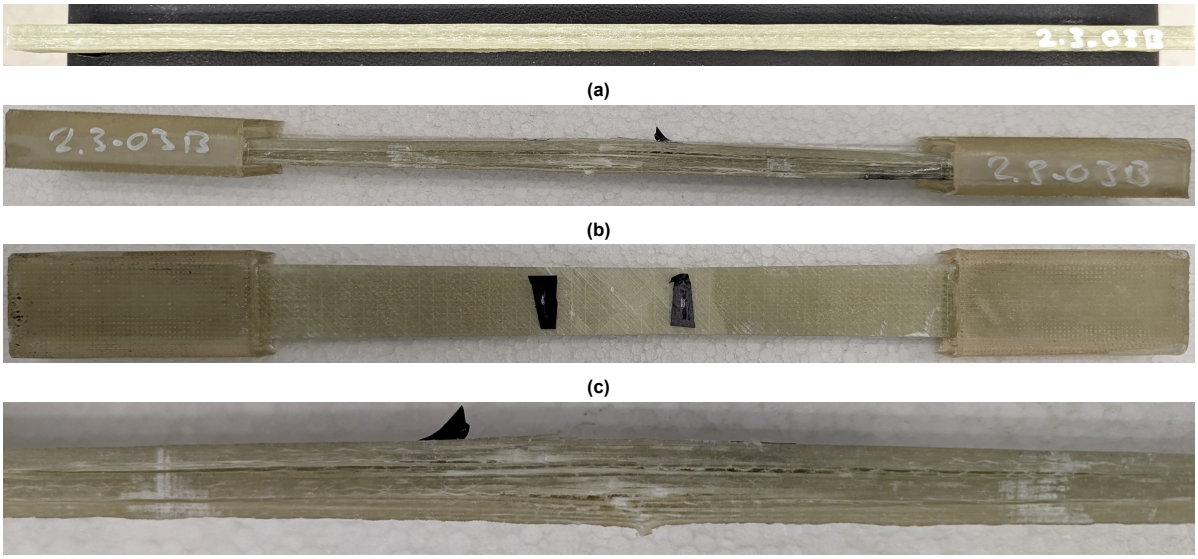

Figure C.22: Coupon PU 2.3_03B (a) before testing, (b), (c) and (d) after testing

Figure C.23: Compression failure in the machine of coupon PU 2.3_03B